Touch inhibits feeding through a neural bottleneck in *C. elegans*

A window into a biological information compression system

Doctoral thesis
to obtain a doctorate (PhD)
from the Faculty of Medicine
of the University of Bonn

Elsa Bonnard
from Dole, France
2026

Written with authorization of

the Faculty of Medicine of the University of Bonn

First reviewer: Dr. Monika Scholz

Second reviewer: Prof. Dr. Tobias Rose

Day of oral examination: 12/17/2025

From the Max Planck Institute for Neurobiology of Behavior - caesar

Table of Contents

List of Abbreviations

5-HT serotonin.

Ca^{2+} calcium.

FPS frames per second.

GECI genetically encoded calcium indicator.

GEVI genetically encoded voltage indicator.

GFP green fluorescent protein.

I1 interneurons 1.

ICE human caspase interleukin-1β-converting enzyme.

K$^+$ potassium.

LED light-emitting diode.

NA numerical aperture.

Na$^+$ sodium.

nAChR nicotinic acetylcholine receptor.

NGM nematode growth medium.

NIR near-infra red.

PLM posterior lateral microtubule.

RIP ring/pharynx interneurons.

ROI region Of interest.

SEM standard error of the mean.

STD standard deviation.

TRNs touch receptor neurons.

YA young adult.

YFP yellow fluorescent protein.

1. Introduction

1.1 Neural bottlenecks: a biological information compression system

Neural bottlenecks are a ubiquitous network motif where a large number of neurons project onto a smaller population. This convergence creates a narrow channel of limited capacity for information transfer, posing a fundamental challenge for neural coding: how to retain essential information when communicating through a restricted pathway.

The bottleneck motif is widespread across species and brain regions. Classic examples are found in sensory systems, like the convergence of 1000 olfactory receptor neurons onto a single mitral cell in the mammalian olfactory bulb (Lledo et al., 2005). Other examples include tactile afferents converging in primate cuneate nucleus (E. G. Jones, 2000) and cat auditory nerve fibers converging in the brainstem (Spirou et al., 2005). Bottlenecks are also critical in motor pathways, such as the descending neurons that form a constraint layer between the brain and body in insects (Bueschges & Ache, 2025), and in integrative hubs like the pontine nuclei, which relay cortical signals to the cerebellum (Brodal & Bjaalie, 1992).

The prevalence of this motif raises a central question: what is the computational purpose of such bottleneck? The efficient coding theory suggests neural systems evolve to maximize information transmission with limited resources (Barlow, 1961). A neural bottleneck could achieve this efficiency through lossless compression, removing redundancies to create an compact representation. Alternatively, it could perform lossy compression, selectively filtering the input to preserve only the information that is behaviorally relevant.

The canonical example for a bottleneck motif displaying efficient coding is the optic nerve (Zhaoping, 2006): while input from photoreceptors has been estimated to encode visual information at a rate of 10^9 bits per second, the output rate is only 10^7 bits per second, a reduction of two orders of magnitude. Author synthesized multiple lines of experimental and theoretical evidence for neural strategies that reduce input redundancy (lossless compression). In the blowfly, for example, large monopolar cells employ mechanisms such as lateral inhibition and temporal filtering to preprocess visual signals, thereby enhancing contrast and eliminating correlated noise.

The drawback of reduced information capacity is mitigated by the advantage posed by convergence motifs. Convergence of multiple inputs improves signal quality and robustness. In the olfactory system, the convergence of many sensory neurons onto a single output cell averages out noise, increasing the signal-to-noise ratio (Lledo et al., 2005). In the fruit fly *D. melanogaster*, neurons receiving convergent input fire more reliably and precisely than their presynaptic partners (Bhandawat et al., 2007). Further evidence from both experimental and computational studies argues that bottleneck motifs might act as coincidence detectors, where convergence makes spike timing more precise and reduces errors (Diesmann et al., 1999; Jeanne & Wilson, 2015; Levi et al., 2022; Mobille et al., 2025).

Beyond sensory systems, convergence is also relevant for sensory-motor transformations. Further computational works explored the functional advantages of compressed sensory representations for downstream motor circuits. Autoencoder models inspired by the converging fly descending neurons to the ventral cord showed that bottlenecks minimize how many neurons are required for optimal performance in selecting the right motor command for a given task, and that modularity increases information transfer, though at the cost of increasing state dependency (Nande et al., 2022). A computational model of the bottleneck from striatum to basal ganglia with a high convergence ratio (1:154) was used to show that even simplified transfer functions to the thalamus which in turn project to cortex are sufficient to reconfigure cortical activity through non-uniform inhibitory basis functions (Humphries, 2025). Finally, pontine nuclei —receiving convergent cortical input— filter out high-dimensional, task-irrelevant activity before relaying cortical signals to the cerebellum (Muscinelli et al., 2023). These findings from modeling studies underscore the critical need to quantify not just how much information is encoded in bottleneck neurons or how the incoming signal is transformed, but specifically how much information is relevant for driving behavior and how the sensory-motor transformation aligns with task performance. This quantification, however, faces the challenge of accessing the activity of all the neurons involved in the bottleneck while monitoring the animal's behavior.

1.2 RIP-I1 neurons in *C. elegans* as a tractable bottleneck

In this thesis, we use the nematode *Caenorhabditis elegans*, a tractable model system where such comprehensive measurement is possible. The worm's compact nervous system of 302 neurons, fully mapped connectome, and genetic accessibility make it ideal for this purpose (Girard et al., 2007). Furthermore, its transparency enables non-invasive imaging of neural activity in behaving animals using genetically encoded calcium indicators. These tools can be combined with cell-specific manipulations to dissect neural circuits, while its rich behavioral repertoire provides robust assays for quantifying bottleneck function.

From connectome data (White et al., 1976; White et al., 1986) reanalyzed by Cook et al. (2019, 2020), we identified a compact neural bottleneck formed by two bilateral pairs of neurons: ring/pharynx interneurons (RIP) and interneurons 1 (I1). RIP receive massively convergent sensory inputs (**Fig.** 1.1). They provide the only direct synaptic connection to the pharyngeal network, an anatomical isolated network controlling the worm pharynx, via gap-junctions to the pharyngeal interneurons I1 (**Fig.**1.1). RIP are located in a large somatic network which among many other functions controls locomotion. This sets up a compact bottleneck motif with sensory inputs in the somatic network, and behavioral output controlled by the pharyngeal network, enabling detailed investigation of the information flow during behavior.

1.3 Touch-feeding paradigm to study RIP-I1 bottleneck function

To understand how the RIP-I1 bottleneck processes sensory information, we aimed to design a behavioral paradigm where we can deliver controlled sensory input to the somatic network and measure the bottleneck output. we used behavior as final read-out, as it reflects the entire process from sensation to action (Krakauer et al., 2017).

A suitable behavioral paradigm must fulfill three criteria: 1. Input specificity: The sensory stimulus must be reliably detected by neurons upstream of the bottleneck. 2. Bottleneck transmission: The signal must pass (solely) through the RIP-I1 pathway. 3. Output control: The behavioral response must be driven by a network downstream of the bottleneck. Furthermore the behavioral paradigm must allow for the manipulation and measurement of neuronal activity. Meeting these conditions enables to determine how the bottleneck transforms sensory inputs into behavioral outputs, drawing a direct link between the bottleneck's structure and its function.

1.3.1 Feeding as behavioral read-out

From the read-out side, the output circuit of the bottleneck is the pharyngeal network comprising 20 neurons which control the pharyngeal muscle and ultimately feeding. While feeding has been studied in *C. elegans*, investigating information transfer requires time-

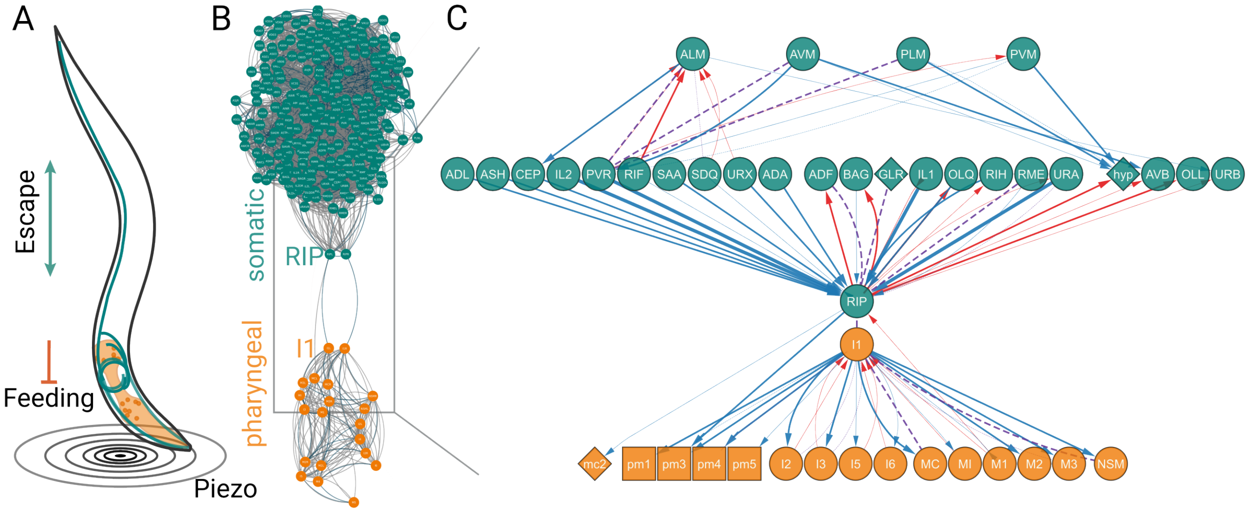

Figure 1.1: Touch-feeding system to study RIP-I1 bottleneck function in *C. elegans*. (A) Schematic of a worm showing its nervous system: pharyngeal neurons controlling the pharynx for feeding (orange) and somatic neurons including sensory neurons and escape circuit (green, organized in the ventral and dorsal nerve cords and head nerve ring). Substrate vibrations (touch stimuli) are delivered by a piezo buzzer. Escape and feeding are the behavioral readouts. (B) Connectome diagram highlighting the RIP-I1 bottleneck as a gateway between the pharyngeal network and the rest of the nervous system. (C) A hierarchical layout of the bottleneck circuit in four layers: 1. the input or sensory layer (touch receptor neurons, TRNs), 2. the interneuron layer (cells presynaptic to RIP), 3. the bottleneck layer (RIP and I1), and 4. the output layer (cells postsynaptic to I1). Circles represent neurons, rectangles represent muscles, and diamonds represent non-neuronal cells (e.g., hypodermis, glia, marginal cells). Directed chemical synapses are solid lines with arrows; gap junctions are dashed lines. Line thickness corresponds to synaptic weight ranges: 1-3 (thin), 4-50 (medium), > 50 (thick). For reference, RIP-I1 connection has a weight of 4. Putative information flow is color-coded: blue (feedforward, sensory to pharynx), red (feedback), and purple (bidirectional). Bilateral neuron pairs are merged for simplicity. The connections within a same layer are not shown. Connectome data are from Cook et al. (2020) where synaptic weights were calculated by summing presynaptic specializations across serial sections. Network analysis and visualization made in Cytoscape (Shannon et al., 2003)

resolved, single-worm data with sufficient throughput to allow for large sample sizes which was not feasible with existing methodologies.

C. elegans feeds on bacteria and other small micro-organisms by drawing in a suspension of food particles from the environment (**Fig.** 1.2). The bacteria are ingested and separated from the liquid by the pumping action of its pharyngeal muscles (Avery & Shtonda, 2003; Fang-Yen et al., 2009; Seymour et al., 1983). Transport of the bacteria proceeds with occasional peristaltic contractions that move food further toward the terminal bulb where a hard cuticular structure, the grinder, crushes the bacteria before they are pushed into the intestine (Albertson & Thomson, 1976).

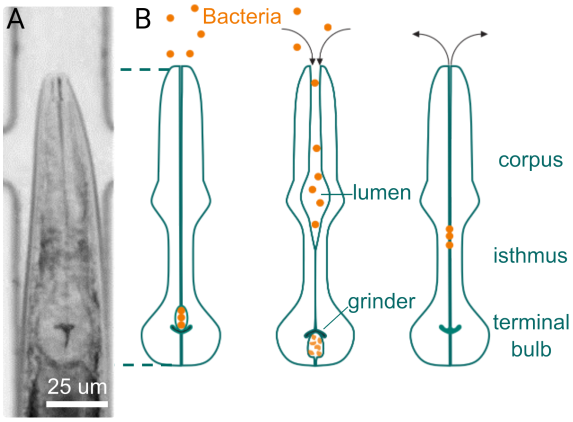

Figure 1.2: *C. elegans* pharyngeal pumping. (A) Bright-field image of *C. elegans* head restrained in a micro-fluidic chamber from Lee et al. (2017). Scale bar 25 µm. (B) Pharyngeal pumping is a contraction–relaxation cycle involving the corpus, anterior half of the isthmus and terminal bulb muscles. Pharynx in its resting state. The cycle starts by near-simultaneous contraction of those muscles resulting in lumen opening which pumps in liquid with bacteria in suspension and grinder rotation which crushes a previous bacteria bowl then passes them to the intestine. Then a Near-simultaneous relaxation brings the grinder to its resting position and close the lumen, expelling the liquid and trapping bacteria. A second motion of the pharyngeal muscles, posterior isthmus peristalsis moves bacteria to the terminal bulb (not shown). Schematic adapted from Avery and Shtonda (2003)

Pharyngeal pumping is inherently a stochastic process (Lee et al., 2017; Scholz et al., 2016, 2017). It has been suggested that stochastic pumping results from a decision making process that serves to regulate pumping based on food availability (Scholz et al., 2017). Even in the absence of food, pumping has been observed and interpreted as a mechanism for food sampling (Lee et al., 2017; Scholz et al., 2017; Trojanowski et al., 2016). When food is abundant, pumping occurs on average up to 300 times per minute (5 Hz) (Lee et al., 2017; Scholz et al., 2016; Song & Avery, 2012). Pumping rates are altered in response to the type, concentration, size, and familiarity of the surrounding bacteria

(Avery & Shtonda, 2003; Lee et al., 2017; Scholz et al., 2016; Song et al., 2013). The behavioral and metabolic context, such as hunger, satiety, and mating drive also influence the rate of food intake (Avery & Horvitz, 1990; Gruninger et al., 2006; You et al., 2006, 2008). Furthermore, various sensory stimuli modulate the pumping rate such as odor (Li et al., 2012; Zou et al., 2018), light (Bhatla & Horvitz, 2015; Bhatla et al., 2015) and touch (Keane & Avery, 2003; McClanahan et al., 2020). Feeding behavior is thus regulated at different time scales ranging from immediate neuro-muscular activity (McKay et al., 2004; Raizen & Avery, 1994; Raizen et al., 1995; Trojanowski et al., 2016) to the intermediate scales of food choice and foraging (Katzen et al., 2023; Li et al., 2012; Scholz et al., 2017), to longer-term life history traits and behavioral state changes of the animal (Avery & Horvitz, 1990; Cermak et al., 2020).

1.3.2 Challenges in measuring feeding

Existing techniques to measure feeding fall broadly into two categories. The first focuses on indirect measures of population food intake, and the second detects each pumping contraction (**Tab.** 1.1). Indirect food intake measures rely either on labeling the food intake of the worm, for example using bio-luminescent bacteria (Ding et al., 2020)), fluorescent bacteria (Andersen et al., 2014; You et al., 2008), or fluorescent beads (Fang-Yen et al., 2009; Kiyama et al., 2012), or by measuring the remaining food concentration over time in large liquid cultures of worms (Gomez-Amaro et al., 2015). However, liquid culture does not allow direct measurement of pumping activity or feeding-related behaviors, such as locomotion toward food. Resolving single pump information can be achieved by combining bright-field microscopy with live worm tracking to remove center of mass motion and enable imaging of the grinder (Cermak et al., 2020; Li et al., 2012; Zou et al., 2018), or alternatively by constraining animals in microfluidics. In tracking and constrained configurations, one can read out pumps by directly following the grinder motion in the pharynx (Lee et al., 2017; Scholz et al., 2016). A complementary technique relies on recording electro-pharyngeograms that detect the signature of muscular contractions in a small population of constrained animals without requiring a tracking microscope (Lockery et al., 2012). Despite these numerous approaches, what is lacking is a method that allows time-resolved pumping detection in populations of unrestrained crawling animals. In this thesis we therefore set out to develop such a method to support the quantification of the bottleneck function.

Table 1.1: Comparison of methods for measuring pharyngeal pumping.

Technique	Single pump	Single worm	Animals	Method	Label	Constrained	Source
Bioluminescent bacteria	No	No	100-1000	Microscopy	No	No	(Ding et al., 2020)
Luciferase expressing worms	No	Yes	100	Microscopy	Yes	No	(Rodríguez-Palero et al., 2018)
Optical density	No	No	100-1000	Absorption	No	No	(Gomez-Amaro et al., 2015)
Tracking microscope	Yes	Yes	1	Microscopy	No	No	(Li et al., 2012); (Cermak et al., 2020); (Zou et al., 2018)
pWarp	Yes	Yes	4	Microscopy	No	Microfluidic	(Scholz et al., 2016)
NemaChip	Yes	Yes	8	Electrophysiology / EPG	No	Microfluidic	(Lockery et al., 2012)
Manual counting	Yes	Yes	1	Microscopy	No	No	(Song & Avery, 2012); (Dallière et al., 2016); (Bhatla & Horvitz, 2015) and many others
PharaGlow	Yes	Yes	1-50	Microscopy	Yes	No	(Bonnard et al., 2022)

1.3.3 Substrate vibrations as a controllable touch stimulus

Among the different sensory stimuli able to modulate feeding, we selected mechanical or touch stimuli. Touch as a sensory modality offers strong practical advantages: it is easy to deliver and control precisely, and mechanosensation in *C. elegans* has been well characterized (Goodman & Sengupta, 2019). Many key genes, proteins, and neurons involved are known, and a variety of transgenic lines are available. Specifically, harsh touch to the tail and substrate vibrations both inhibit pumping (Keane & Avery, 2003; McClanahan et al., 2020). However, a detailed characterization of the stimulus-response curve, i.e., psychometric curve, is missing.

Gentle touch stimuli are detected by extra-pharyngeal neurons: substrate vibrations are detected by the six touch receptor neurons (TRNs) (Wicks & Rankin, 1995; Wicks et al., 1996). These mechanoreceptors thus form the input layer upstream of the RIP-I1 bottleneck, positioning the bottleneck layer strategically to modulate touch signal before they reach the pharynx. However, there is no direct synaptic connections between those mechanoreceptor neurons to the RIP neurons (**Fig.** 1.1). It remains an open question whether touch signal is transmitted through the RIP-I1 bottleneck or use extrasynaptic signals like neuromodulators (Pocock & Hobert, 2010; Sawin et al., 2000), and to what extent they modulate pharyngeal pumping.

Furthermore, the well-defined escape response to touch, consisting of an increase of speed and reorientation, provides an additional and robust behavioral read-out that is processed outside of the pharynx (Goodman, 2006; Pirri & Alkema, 2012). This offers a valuable comparative measure of the touch signal processing that does not go through the bottleneck but also yields a measurable behavioral output in locomotion. In addition, the two behaviors, locomotion and feeding, are coordinated during effective foraging (Iwanir et al., 2016). We hypothesize that based on the anatomy, the RIP-I1 bottleneck is in a key position to coordinate those distinct behavioral outputs. This provides a further ethological utility of understanding information flow in this system.

1.3.4 Calcium indicators to measure neuronal activity

To measure activity of the neurons in the input and bottleneck layers, we take advantage of *C. elegans* optical transparency and amenability to genetic manipulation by using genetically encoded calcium indicator (GECI).

Fluorescent measurement of intracellular calcium (Ca^{2+}) using GECI is a standard method for monitoring neuronal activity (Inoue, 2021). GECIs enable specific, long-term imaging of calcium dynamics *in vitro* and *in vivo* with cell-type and subcellular resolution. This approach reports Ca^{2+} influx into the cell, for example through voltage-gated Ca^{2+} channels, which is triggered by both action potentials and graded membrane depolarization. It also captures local Ca^{2+} signals in dendritic spines that are driven by synaptic plasticity. Furthermore, Ca^{2+} signals can be amplified through subsequent Ca^{2+} release from internal stores e.g. Ca^{2+} release from the endoplasmic reticulum. As Ca^{2+} is needed for synaptic vesicle release, this is ultimately a read-out of signal transmission in neurons, however compartmentalization and measurement in the vicinity of the soma may impact how signals should be interpreted.

This method is particularly powerful for studying non-spiking neurons, such as those prevalent in *C. elegans*. These neurons lack voltage-gated sodium (Na^{+}) channels (Yu et al., 2005) and therefore do not generate conventional action potentials. *In vivo* electrophysiological measurements confirmed that *C. elegans* neurons do not generate Na^+-dependent action potentials but rather potassium (K^+)/Ca^{2+} voltage-dependent graded non-linear responses to current injection or show bistable potentials (Goodman et al., 1998; Mellem et al., 2008). A few neurons have been recently reported to generate Ca^{2+}-dependent action potentials (Jiang et al., 2022; Q. Liu et al., 2018). These complex electrophysiological responses have been successfully reproduced using models composed solely of Ca^{2+} and K^+ conductance, highlighting the central role of these ions in*C. elegans* neurons (Naudin et al., 2022). Furthermore, their relatively slow dynamics —compared to millisecond-scale action potentials— make them particularly suitable for tracking with calcium indicators, with hundreds of milliseconds to seconds time resolution.

GECI like the GCaMP series have been iteratively engineered over multiple generations to enhance their brightness, photostability, sensitivity, and binding kinetics with minimal disruption to normal animal physiology (Dana et al., 2019; Zhang et al., 2023). In *C. elegans*, GCaMP usage has been widespread and enabled discoveries about stimulus encoding of sensory neurons using single-cell imaging (Clark et al., 2006; Itskovits et al., 2018; Kato et al., 2015; Katta et al., 2019; Larsch et al., 2015) and multineuron imaging in chemosensory cells (Itskovits et al., 2018; Pritz et al., 2023). In addition, GCaMP was essential for detecting the compartment-specific activity in interneurons (Hendricks et al., 2012) and global effects of single neurons on activity and sleep (Turek et al., 2013). Going beyond single or few neurons, whole-brain labeling even enabled the discovery of brain-wide coding of behavior in restrained and moving animals (Atanas et al., 2023; Hallinen et al., 2021; Kato et al., 2015; Nguyen et al., 2016; Venkatachalam et al., 2016).

More specifically, GCaMP indicators have reported a rise in intracellular Ca^{2+} in TRNs triggered by mechanical stimuli (Cho et al., 2017; Nekimken et al., 2017; Shaw et al., 2016; Suzuki et al., 2003). Whole-brain calcium imaging in freely moving animal suggest that activity in RIP and I1 are coupled with slow—tens of seconds to minutes—pharyngeal pumping variations (Atanas et al., 2023), however, in these datasets RIP neurons could only be measured once and the conclusions are therefore preliminary. Inward currents upon mechanical stimulation have been recorded in the TRNs, where Na^+ is the main ion carrier (Eastwood et al., 2015; Katta et al., 2019; O'Hagan et al., 2005). To date, no electrophysiological data are available for either the RIP or I1 neurons. neurons. Based on the observations reported above, it is likely that sensory information will be encoding by graded potentials in the bottleneck neurons and that it can be measured using GCaMP indicators. To establish the response of the neurons involved in the bottleneck to sensory stimuli requires measuring the neuronal stimulus response curve, i.e., the neurometric curve.

1.4 Question and aims of this thesis

This thesis aims to investigate how biological neuronal networks compress information, using behavior as a final read-out. We address this fundamental question by studying the function of the RIP-I1 neural bottleneck in *C. elegans* using a touch-feeding paradigm as a model system. To achieve this goal, we used a three-step approach:

- Aim 1: Measure feeding in freely moving animals.
- Aim 2: Establish the touch-feeding paradigm and quantify the psychometric curves (i.e., the relationship between stimulus intensity and behavioral response).
- Aim 3: Measure information flow through the bottleneck by comparing neurometric curves (i.e., the stimulus-neuronal response relationship) from the input and bottleneck layers to the psychometric curve.

The method developed to address the first aim is presented in Sections 2.1 (Methods) and 3.1 (Results) and has been published in a peer-reviewed journal: (Bonnard et al., 2022).

The second aim is addressed in Sections 2.1 (Method—shared with aim 1), 3.2 and 3.3 (Results). These sections describe how we applied this new method to estimate, for the first time, the input-output transformation of the RIP-I1 bottleneck, using touch as stimulus and feeding as read-out and demonstrate its requirement by genetically ablating its key neuronal layers. This part of the work is included in a manuscript in preparation (Bonnard et al., in prep.)

Finally, the third aim is addressed in Sections 2.2 and 2.3 (Methods) and in Sections 3.4 and 3.5 (Results). These sections describe our approach for measuring how the touch signal intensity is encoded in the input versus bottleneck layers using single neuron calcium imaging. First, we focus on how we adapted a new calcium indicator for use in *C. elegans* to achieve sensitive measurements of calcium dynamics across the entire behaviorally relevant range of stimulus intensities in the TRNs in immobilized animals. These results have been published in a peer-reviewed journal: (J. Liu et al., 2024). Second, we describe how we extended this approach to behaving animals. This allowed us to obtain the first insights into how touch signal is transformed within the RIP bottleneck neurons and to directly correlate these neural dynamics with the resulting feeding behavior. The results are included in the manuscript in preparation cited above. (Bonnard et al., in prep.)

2. Materials and methods

2.1 Measuring feeding and locomotion in freely moving animals

2.1.1 *C. elegans* maintenance and handling

C. elegans were grown on nematode growth medium (NGM) plates at 20°C and fed by the bacterial *Escherichia coli* strain OP50. Animals were synchronized by letting adult gravid animals lay eggs for 2–3 hr, then removing the adults. The average time from egg to young adult stage for the reference strain GRU101 expressing yellow fluorescent protein (YFP) in its pharyngeal muscles (in List of Transgenic Lines) is about 63 hr. This time varied between transgenic lines and was measured to ensure age matched populations.

For the touch assays, synchronized adults were transferred by picking onto the imaging plates. In case of transgenic lines with extra-chromosomal arrays, animals in the larva stage L4 were selected under an epifluorescence microscope (Axio Zoom V16; Zeiss®) and picked to an intermediate new seeded NGM plate the day before for both control and mutant lines. They were then transferred by picking onto the imaging plates prior the recording.

For the other assays, synchronized adults were washed off the culture plates with 1 ml of M9 buffer and collected in an Eppendorf tube. Animals were allowed to settle for 1 min, the supernatant was removed and the tube was refilled with M9. Washing was repeated two more times. The washing was sufficient in that we did not observe animals remaining in the spots containing the remainder of M9 on the assay plates, suggesting that the bacterial amount was too diluted to induce dwelling behavior. The remaining worms suspension was pipette onto the imaging plates.

2.1.2 Confocal microscopy

To assess the effect of human caspase interleukin-1β-converting enzyme (ICE), we generated young adults using the cGAL4/UAS system to drive expression in specific neurons: UAS effectors green fluorescent protein (GFP) with (test) or without (control) ICE were expressed under the control of the GAL4 driver *nlp-51-GAL4* for targeting the RIP neurons (strains INF530, INF529 in List of Transgenic Lines) or the *lgc-8* for targeting I1 neurons (Strains INF127, INF411 in List of Transgenic Lines). Animals were immobilized in 50 mM Na^+ azide and mounted on a 2 % agarose pad on a microscope slide under a coverslip and imaged using a Leica Stellaris confocal microscope (Leica Microsystems®) equipped with a 25×/0.95 numerical aperture (NA) Nikon water immersion objective lens. Fluorophores were excited using a 488 nm laser for GFP and hybrid detectors were used for signal detection. Image acquisition was conducted using LAS X software (Leica Microsystems®) and processing using Fiji (Schindelin et al., 2012).

2.1.3 Epifluorescence microscopy

2.1.3.1 Imaging plate preparation

For touch assays, customized imaging arena were prepared. Imaging arena for the touch assays were prepared by filling a copper ring window (5 × 7 x 1 mm) with 2 % agarose diluted in M9 buffer placed on top of an NGM block taken out from a 6 cm diameter Petri dish. The copper ring was added for keeping the animals in the field of view. For ensuring the cohesion of the copper ring arena with the NGM block during the transfer to the stimulation apparatus, an extra 2 ml 2 % agarose on the copper ring edge was added. The arena was seeded with 4 µl of 10-fold concentrated overnight OP50 culture and let dry at room temperature for 1 hr. For some of the behavioral assays, standard 6 cm NGM plates were used as indicated. The presence or absence of bacterial food or the addition of a copper ring are mentioned in the description of each assay below.

2.1.3.2 Population imaging

Imaging of multiple animals simultaneously was performed using a commercial upright epifluorescence microscope (Axio Zoom V16; Zeiss®) equipped with a 1x objective (PlanNeoFluor Z 1.0x/0.25 NA). For imaging of YFP fluorescence, light from an light-emitting diode (LED) lamp (X-Cite XYLIS) was reflected towards the sample using a dichroic mirror (FT 515; Zeiss®) and filtered (BP500/25; Zeiss®). Emitted light was filtered using a band-pass filter (BP 535/30; Zeiss®) and focused onto the camera sensor (acA3088-57um; Basler®) using a camera adapter with an additional 0.5x magnification (60 N-C 2/3" 0.5x; Zeiss®). The power density of fluorescence excitation at the focal plane (0.24 mW/mm2 at 500 nm) was measured using a powermeter sensor (PS19Q; Coherent®) with the corresponding controller (PowerMax; Coherent®). Animals were imaged at 30 frames per second (FPS) for 5 min unless otherwise indicated. For imaging of mCherry, the filter cube was replaced with a commercial filter set (64HE; Zeiss®). The resulting power density using this cube was 0.76 mW/mm2 at the focal plane.

2.1.3.3 Single animal imaging

For acquiring behavioral data in mutants for touch assays, single animals were imaged using an upright microscope (BX51WI; Olympus®) and a 4x objective (Plan N, 4x/ 0.10NA; Olympus®), yielding a full field of view of 2048 x 2048 µm at a resolution of 4 µm/px. To optimize data acquisition and storage, a region of interest region Of interest (ROI) of 800 x 800 µm was recorded. Transgenic lines with either mCherry (red) of YFP-labeled pharynx were imaged. Excitation light was delivered from an LED lamp (Spectra X light engine; Lumencor®) using a 3 ms-stroboscopic illumination. YFP was excited by the LED lamp cyan line (470/24 nm). Transmitted and emitted light were filtered with a 475/42 nm pass-band excitation filter, a 495 nm long-pass dichroic, and a 510 nm long-pass emission filter (ET510LP; Chroma®). mCherry was excited by the green line (550/15 nm). Transmitted and emitted light were filtered with a 545/30 nm pass-band excitation filter, a 560 nm long-pass dichroic, and a 575-625 nm pass-band emission filter. Images were detected using a sCMOS camera (Zyla iXon Ultra; Andor®) at 30 Hz acquisition rate, 3 ms exposure time and a 16 bit read-out depth using a customized interface (LabVIEW; National Instruments®). Animals were tracked in real-time using a customized intensity based segmentation tracking algorithm with a 13 Hz refreshment rate. Animal center of mass coordinates were send to an 3-axis motorized stage (X-LSM150A; Zaber®) to keep the animal center in the field of view.

2.1.3.4 Dual bright-field and fluorescence imaging

For acquiring data for the manual and automated pumping detection comparison, dual imaging was performed using an upright microscope (BX51WI; Olympus®) and a 10 x objective (UplanSApo, 0.4 NA; Olympus®). For bright-field imaging, light emanating from a near-infrared (780 nm) LED (M780LP1 and driver LEDD1B; Thorlabs®®) was filtered using a (785/62 BrightLine HC; Semrock®) and projected onto the sample via the bright-field illumination condenser. To excite fluorescence, the Teal line from an LED lamp (Spectra X light engine; Lumencor®) was filtered (513/17 nm BrightLine HC; Semrock®) and projected onto the sample using a 520 nm long-pass dichroic (FF520-Di02; Semrock®). Transmitted and emitted light were filtered using a 532 nm long-pass filter (BLP01-532R; Semrock®). To simultaneously record images in bright-field and fluorescence, a dual-camera device was used (DC2; Photometrics®). Light was split into two channels using a 695 nm long-pass dichroic mirror (695DCXRUV; Photometrics®) and images were projected into two cameras (acA3088-57um; Basler®). Fluorescent light was band-pass filtered (550/49 Brightline HC; Semrock®) before reaching the camera sensor. The exposure time (6 ms) of one camera served to synchronize the acquisition of the second camera and the Lumencor® light engine. Individual worms were manually tracked using a 3-axis motorized stage (X-LSM150A; Zaber®).

2.1.4 Behavioral assays

2.1.4.1 Development experiments

Animals were pre-synchronized by hypochlorite bleaching, allowed to hatch overnight in M9 and then cultured on NGM plates with OP50 at 20 °C. On day 3 after pre-synchronization, worms were synchronized again by letting 20 gravid animals lay eggs for 2 hr per assay plate, then removing the adults and letting embryos grow for specific durations to reach the appropriate larval or adult stage (19 hr for mid-L1, 31 hr for mid-L2, 39 hr for mid-L3, 50 hr for mid-L4, 65 hr for young adults). For the assay plates, 40 µl of *E. coli* OP50 culture was spotted onto an empty 6 cm NGM plate a few hours before the synchronization and left to dry. Synchronized animals were imaged directly on their assay plates. The magnification for each stage was chosen to achieve an approximate pharynx length of 60 pixels (2 x (1.18 µm/px) for L1, 1.5 x (1.57 µm/px) for L2, 1.4 x (1.69 µm/px) for L3, 1.3 x (1.81 µm/px) for L4 and the standard 1 x (2.36 µm/px) for young adults). Three assay plates were imaged once per stage, and three additional plates were imaged at each stage to test for photo-sensitivity.

2.1.4.2 Starvation experiments

Washed animals were transferred to the center of an empty 6 cm NGM plate at room temperature and left to recover for 15 min before imaging. The same plate was imaged at defined time points for progressively more starved animals (at 30 min, 90 min, 150 min and 210 min after being taken off food). The field of view was chosen randomly on the plate but was required to contain at minimum 3 animals at the beginning of the recording. For control, washed animals were transferred close to a 40 µl of*E. coli* OP50 lawn, which was spotted onto an empty 6 nm cm NGM plate a few hours before the recordings and allowed to dry. Acclimation time and recording are similar for starved animals.

2.1.4.3 Male and hermaphrodite interaction experiment

For long-term imaging of the male and hermaphrodite interaction, stroboscopic illumination (5 ms light pulses) were used to reduce bleaching. Excitation light was synchronized with the camera exposure using the GPIO camera line and the TTL input of the

LED lamp. Frames were collected using a custom software (LabVIEW; National Instruments®). To reduce the amount of stored data and allow continuous recording using a standard computer (Celsius W520; Fujitsu), images were segmented automatically and only areas containing animals, and their coordinates within the image, were stored. This procedure allowed a data reduction by approximately 1000 fold. For imaging, a copper frame (5.3 x 3.75 x 1 mm) was filled with 2 % low melting point agarose (Sigma Aldrich®) in M9 and 2–5 µl of a 10-fold concentrated overnight OP50 culture was seeded on top. The frame was deposited into a 10 cm NGM plate, and animals were transferred to the agarose arena. To preserve the moisture of the preparation and prevent shrinking of the gel, about $\frac{1}{3}$ of the agar at the outer rim of the plate was removed using a scalpel and the space was filled with 6 ml of M9. Animals were recorded for at least 3 hr and all animals that were continuously tracked for at least 2 hr were included in the analyses in **Fig.**3.6.

2.1.4.4 Touch experiments

Animals were transferred onto the imaging arena and acclimated for 30 min in the recording room. The arena was then transferred to the stimulus apparatus, where animals acclimated for an additional 5 min under imaging conditions. For the psychometric measurement, ten to fifteen synchronized GRU101 adult animals were transferred onto the imaging arena for population imaging. For the mutants experiments, a single animal was transferred in the imaging arena for single animal tracking imaging.

Substrate vibrations were delivered by gluing a 48 mm diameter piezo buzzer (APS4812B-LW100-R, PUI Audio Inc.®) on a 60 mm diameter Petri dish painted matte black to minimize light reflection. The buzzer-equipped dish was hold in a customized 3D-printed holder. For each recording, the NGM block containing the imaging arena was positioned anew within the stimulus apparatus.

The piezo element was driven by a 630 Hz sinusoidal voltage for 1 s . For measuring the psychometric curves, animals were exposed to multiple buzzes at various amplitudes (0 to 30 volt peak to peak (V), 5 V step) presented in a random order with 3 min inter-buzz intervals. For the mutants experiment, single animal was exposed to a single 15 V buzz repeated 5 times. A trial lasts 2 min with the buzz onset at 60 s and inter-time trials was about 3 min.

Stimulus delivery was synchronized with camera acquisition using a data acquisition card (BNC-2110, National Instruments®) driven by a customized Matlab program based on the data acquisition toolbox (Matlab, R2020a, MathWorks®).

2.1.5 Analysis

2.1.5.1 Pharyngeal pumping and animal tracking—fluorescence data from population imaging

For population imaging, animals were tracked using our custom python analysis package PharaGlow which is freely available under a permissive GPL 3.0 license. In brief, PharaGlow runs a three-step analysis:1. center of mass tracking and collision detection, 2. linking detected objects to trajectories and 3. extracting centerline, contour, width, and other parameters of the shape to allow extracting pharyngeal pumping events. Tracking uses the soft matter package (Allan et al., 2021). The code is fully modular and any existing tracking code could in principle be used for the first two steps provided the input data is formatted to PharaGlow standards. We provide example data and example Jupyter notebooks to help users make use of our package both in personal computer and high-performance cluster settings. The resulting files contain the position, and the straightened images which are further processed to extract the behavioral measures as described in **Fig.** 3.1.

To obtain pumping traces from straightened animals, the inverted maximum of the dorso-ventral standard deviation of brightness is calculated for each straightened frame per animal (**Fig.** 3.1). This metric is sensitive to the opening of the pharyngeal lumen and terminal bulb contractions. Peaks in the resulting trace correspond to pumping events. Due to the animal motion, uneven illumination or defocusing can modify the baseline of the pumping metric. We correct for baseline fluctuations and spurious fluorescence changes by subtracting the background fluctuations using a rolling mean filter of 1 s (except for eat-18 mutants, where we use 3 s otherwise the slow contractions were removed too). To the remaining signal we apply a smoothing filter of width = 66 ms (2 frames). We detect peaks using AMPD, an algorithm for peak detection in quasi-periodic signals (Scholkmann et al., 2012). We also require the peak distances to obey physiologically reasonable rates, i.e., the peaks can not be closer than dmiN = 132 ms (4 frames). To automatically establish the noise level of the trace, we compare the incidence of intervals between detected peaks that violate the assumption dmin > 132 ms and select the minimal prominence required, such that the fraction of violating intervals is lower than a sensitivity parameter. For all dataset with 5-min recordings, we set s = 0.999. To obtain pumping traces from straightened animals, the inverted maximum of the dorso-ventral standard deviation of brightness is calculated for each straightened frame per animal (**Fig.** 3.1).

In the male-hermaphrodite long-term recordings, we use a Hampel filter with a width of 300 frames to remove spurious outliers in the signal which affect peak detection and set s = 0.9999. Depending on the purpose, pumping rates have been calculated as follows: To determine the average pumping rate per track, we calculate the number of pumping events / total track duration. To obtain pumping rate distributions, we calculate the number of pumps in a sliding window of 10 s and combine data from all tracks. The ‘instantaneous pumping rate’ is defined as 1/Δt between pumps. We use the instantaneous rate when a higher temporal resolution is desired. Which rate metric is used is indicated in the caption.

2.1.5.2 Pharyngeal pumping and animal tracking—fluorescence data from single animal imaging

Image processing from single animal assays was performed using a compact version of the custom analysis pipeline detailed in **Section** 2.1.5.1. The pipeline executed three primary functions: (1) stage-camera calibration, (2) animal tracking, and (3) extraction of pumping events. Following each recording session, a spatial calibration was performed to convert pixel coordinates into physical units (µm). Calibration images were acquired by displacing the microscope stage a fixed known distance along the x and y axes using a calibration slide. A transformation matrix was calculated from these images, which was subsequently used to convert the real-time tracking coordinates of the pharyngeal center of mass from the camera reference frame into the laboratory reference frame. To ensure continuous and accurate tracking at the full camera acquisition rate of 30 FPS, the pharynx was further tracked offline using the Soft Matter Particle Tracker package (Allan et al., 2021). This offline tracking provided higher fidelity than the real-time system, which operated at a refresh rate of 13 Hz. A ROI of 60 x 60 px was defined around the tracked pharyngeal position in each frame. Pumping events were quantified by analyzing the dynamics of fluorescent intensity within the ROI. For each frame, the skewness of the fluorescent intensity distribution inside the ROI was calculated. Pumping events were identified as distinct peaks in the resulting skewness-versus-time signal.

2.1.5.3 Assigning high and low pumping rate states

Pumping rates (Hz) were calculated from the total number of pumping events detected within a 30 s window. Further smoothing for visualization purpose is indicated in captions. For the touch experiments, pumping rate was smoothed using a 1 s rolling mean (30 frames). The basal pumping rate was defined as the mean rate during the 10 s period preceding stimulus onset. A Gaussian mixture model (with 2 or 3 components) fit to the basal rate distribution for each transgenic line was used to determine a threshold for classifying pumping states. For all other experiments, a fixed threshold of 2.5 Hz was applied to the pumping rate to distinguish between fast and slow pumping states.

2.1.5.4 Animal selection

Animals that were continuously tracked either for at least 60 s (**Fig.** 3.1, **Fig.** 3.2 and **Fig.** 3.4) or for the duration specified by the touch assays quantification were including (**Fig.** 3.15 and **Fig.** 3.19). In the starvation experiments, animals that were successfully tracked for at least 20 s were included due to the larger velocity in this condition (**Fig.** 3.4). Due to age synchronization, all animals in the field of view were of similar size in the wild-type experiments. For *eat-18* mutants, the size and developmental stage of the animals were more dispersed and only animals that had the appropriate size for their stage were included (**Fig.** 3.8). No other filtering or outlier removal was performed.

2.1.5.5 Autocorrelation of pumping rates

The autocorrelation of the pumping rates for the 2 hr recordings was calculated from the 10 s average pumping rates. The decay time of the autocorrelation was determined using a one-sided t-test for each time-point and calculating if the sample mean of the autocorrelation for each animal differed from 0. To determine the uncertainty of the decay time, we ran leave-one-out bootstrapping and report the mean and standard deviation (STD) of the leave-one-out testing.

2.1.5.6 Velocity and reversal measurement

Velocity was calculated from the tracked center of mass of the labeled pharynx. Reversals were calculated based on the angle between the pharynx and the animal's nose tip direction. To avoid spurious reversals, the nose tip trajectories are coarse-grained to 6 Hz, and the angle between the nose tip and pharynx is smoothed with a window of width = 1 s (30 frames). Time-points with angles exceeding 120° were annotated as reversals. Reversals shorter than 0.5 s are removed. The estimation of the pharyngeal area is based on an automated threshold of the pharynx.

2.1.5.7 Quantification of feeding and escape responses to touch

Escape responses were calculated as the percent change in velocity after (S_{post}) stimulus onset compared to before (S_{pre}) as follow:

$$\frac{\Delta S}{S_0} = \frac{S_{\text{post}} - S_{\text{pre}}}{S_{\text{pre}}} \times 100\%$$

Where S_{pre} and S_{post} are the average velocity measured in a 10 s time window immediately before and after stimulus onset. Animals were classified as escape responders if S_{post}

was greater than one STD above or below S_{pre}. A positive percentage change indicates a speed-up (escape response), a negative value indicates a slow-down, and a value of zero indicates no change.

Similarly, feeding responses were calculated as the percent change in pumping rate after (P_{post}) stimulus onset compared to before (P_{pre}) as follow:

$$\frac{\Delta P}{P_0} = \frac{P_{\text{post}} - P_{\text{pre}}}{P_{\text{pre}}} \times 100\%$$

Where P_{pre} and P_{post} are the average pumping rate measured in a 10 s time window immediately before and after stimulus onset. The pumping rate for each window was calculated as the total number of pumping events divided by the window duration. Animals were classified as pumping responders if P_{post} was lower or higher than one STD P_{pre}. A negative value indicates a pumping inhibition, a positive percentage change indicates an increase in pumping, and a value of zero indicates no change.

To quantify the psychometric relationship, we fitted the behavioral response data against stimulus intensity with either a linear or a logistic function. The regression was performed using a weighted least-squares algorithm, where the weights were defined as the inverse of the standard deviation (STD) for responses at each stimulus intensity. This weighting scheme accounts for the inhomogeneity of the variance (or standard deviation) of the response data across stimulus intensities.

2.1.5.8 Manual annotation of pumping behavior

Movies for individual animals were created from a large field of view and expert annotators counted pumps by displaying the movie using the cell counter tool in Fiji (Schindelin et al., 2012). The annotators were blinded to the movie conditions and to the other experts' results.

2.2 Measuring calcium signal in response to touch in single neurons in immobilized animals

2.2.1 Plasmids and transgenic lines

We created new transgenic lines co-expressing the calcium indicator GCaMP7f or GCaMP8f and the red fluorescent marker mKate2 under the promoters *myo-2p* for pharyngeal muscles (strains INF491 and INF418) and *mec-17p* for TRNs (strains INF498 and INF447), as follow:

The plasmid *pLJ50* was made by replacing the *unc-31p* from *pRL231* (gift of Manuel Zimmer) with *myo-2p* to target pharyngeal muscles. *pLJ52* was adapted from the sequence described in Zhang et al. (2023) by codon optimizing the GCaMP8f and adding three synthetic introns as described in Redemann et al. (2011). The sequence was created using the Codon Optimization Tool at https://worm.mpi-cbg.de/codons/cgi-bin/optimize.py. Then, GCaMP8f was subcloned into *pLJ50* to replace GCaMP7f to make *pLJ53*. *SL2*::*mKate2*::*let-858 3'UTR*—coding for the red indicator mKate2—was used to replace the *unc-54 3'UTR* in *pLJ53* to make *pLJ54*. Then, *myo-2p* was further replaced by *mec-17p*—to target TRNs—to make *pLJ57*. GCaMP8f from *pLJ57* was replaced by GCaMP7f to make *pLJ80*.

For I1, we injected the plasmid *pLJ55* into N2 animals. The resulting strain was further crossed to the light-insensitive double mutants *lite-1(ce314) gur-3(ok2245)* (MT21793 strain from Bhatla and Horvitz (2015)) to create INF205 strain. We created similarly INF204 for TRNs. For RIP, we injected *pLJ56* into MT21793. We isolated further a worm with particularly strong RIP expression and maintain it to create INF559 strain.

Plasmids sequence are available in **Tab.** 2.1 and transgenic lines description in List of Transgenic Lines.

Table 2.1: Plasmid Constructs for generating the GCaMP lines

`Name`	**Sequence**	**Description**
`pRL231`	*unc-31p*::GCaMP7f::*unc-54 3'utr*	GCaMP7f
`pLJ50`	*myo-2p*::GCaMP7f::*unc-54 3'utr*	GCaMP7f in pharyngeal muscles
`pLJ53`	*myo-2p*::GCaMP8f::*unc-54 3'utr*	GCaMP8f in pharyngeal muscles
`pLJ54`	*myo-2p*::GCaMP8f::*sl2*::*mKate2*::*let-858 3'utr*	GCaMP8f and mKate2 in pharyngeal muscles
`pLJ56`	*nlp-51p*::GCaMP8f::*sl2*::*mKate2*::*let-858 3'utr*	GCaMP8f and mKate2 in RIP neurons
`pLJ57`	*mec-17p*::GCaMP8f::*sl2*::*mKate2*::*let-858 3'utr*	GCaMP8f and mKate2 in TRNs
`pLJ80`	*mec-17p*::GCaMP7f::*sl2*::*mKate2*::*let-858 3'utr*	GCaMP7f and mKate2 in TRNs
`pLJ120`	*lgc-8p*::GCaMP8f::*sl2*::*mKate2*::*let-858 3'utr*	GCaMP8f and mKate2 in I1 neurons

2.2.2 Imaging plates preparation

For imaging GCaMP signal in pharyngeal muscle, imaging plates were prepared similarly that for NGM plates, but without cholesterol and with agarose instead of agar to reduce auto-fluorescence.

For imaging GCaMP signal in single neuron, an imaging chamber was prepared by filling a 5 × 7 mm copper ring window by 2 % agarose placed on an NGM plate. The copper ring was used to keep the experimental parameters as similar as possible as for the touch behavioral assay (See 2.1.3.1). For ensuring the cohesion with the NGM block during the transfer to the stimulation apparatus, an extra 2 % agarose on the copper ring edge was added.

2.2.3 Pharyngeal muscle activity imaging

2.2.3.1 Low resolution imaging

Thirty adult animals were picked onto an imaging plate seeded with 150 µl of *E. coli* OP50 from an overnight culture. Animals were imaged on a commercial upright epifluorescence microscope (Axio Zoom V16; Zeiss®) equipped with a 1× objective (PlanNeoFluar Z 1.0×/0.25 NA) with a camera sensor (acA3088-57 µm; Basler®) using a camera adapter with an additional 0.5× magnification (60 N-C $\frac{2}{3}$” 0.5x; Zeiss®) at 16× nominal (0.5× on camera) magnification resulting in a field of view of 1.5 cm × 1.0 cm. Images of the lawn were recorded for 10 min at 30 FPS. GCaMP7f images were recorded with a camera gain of 25 dB, and GCaMP8f had to be reduced to a gain of 19 dB to avoid overexposure.

2.2.3.2 High resolution imaging

Adult animals were loaded into microfluidic chips designed for measuring pharyngeal pumping (Lee et al., 2017; Scholz et al., 2016). The microfluidic chamber was perfused with 10 mM serotonin (5-HT) prepared with RediPrep serotonin powder (InVivo Biosystems, USA). After 10 min, most animals showed regular pharyngeal pumping. Animals remained immersed in 5-HT during the recordings. The preparation was imaged on a commercial upright epifluorescence microscope (Axio Zoom V16; Zeiss®) equipped with a 1× objective (PlanNeoFluar Z 1.0×/ 0.25 NA.) with a camera sensor (acA3088-57 µm; Basler®) using a camera adapter with an additional 0.5× magnification (60 N-C$\frac{2}{3}$” 0.5x; Zeiss®) at 180× nominal (5.626× on camera) magnification. The frame rate was 30 FPS with 30 ms exposure time. The resulting images were cropped to a region containing the entire pharynx of the worm using Python and rotated for display. The relative fluorescence

$\Delta F/F0$ was calculated from the mean intensity across the entire image relative to the baseline (5th percentile of the data). Peaks were detected using Python script and aligned to their respective maximum. The height of the peak and the half-decay time were extracted for each peak. Samples were selected for similar mean pumping rates and lower mean rates to allow for stable baselines to develop between peaks.

2.2.3.3 Bright-field imaging

Animals were imaged on a dissection microscope (Axio Zoom V16; Zeiss®) at 125× nominal, 0.614 µm/px resolution, with a white LED light source. Images were recorded for 30 s at 30 FPS. Animals were manually kept centered in the field of view.

2.2.3.4 Pharyngeal pumping rates calculation

Fluorescent images were analyzed using PharaGlow (section 2.1; (Bonnard et al., 2022)). The peaks of the resulting intensity traces were found using the built-in peak detection, and an average pumping rate per tracklet was calculated as N_{pumps}/duration.

For bright-field images, 300 frames of data (corresponding to 10 s) that had a clearly visible grinder were counted manually by visualizing the data in Fiji (Schindelin et al., 2012). Pumping rates were calculated as pumping events/10 s.

2.2.4 Neuron activity imaging

2.2.4.1 Confocal microscopy

Young adults expressing GCaMP7f or GCaMP8f and mKate2 were immobilized in 50 mM sodium azide and mounted on a 2 % agarose pad on a microscope slide under a cover slip. They were imaged using a Leica Stellaris confocal microscope (Leica Microsystems®) equipped with a 25×/0.95 NA water immersion objective lens. Fluorophores were excited using laser lines at 479 nm for GCaMP7f/8f and 589 nm for mKate2, and hybrid detectors were used for signal detection. Image acquisition was conducted using LAS X software (Leica Microsystems®) and processing using Fiji (Schindelin et al., 2012).

2.2.4.2 Single neuron calcium imaging

Three to six adult animals were picked onto the imaging chamber and immobilized in 10 mM levamisole (Sigma-Aldrich). The animals were imaged using an in-house built epi-fluorescence microscope for ratiometric calcium imaging equipped with a 20 × objective (S Plan Fluor LWD, 0.70 NA, Nikon). The resulting field of view was 250 × 500 µm with a pixel size of 0.24 µm per pixel. To excite GCaMP7f/8f and mKate2 fluorophores, the cyan (470/ 24 nm, Chroma®) and green (575/15 nm, Semrock®) lines from an LED lamp (Spectra X light engine, Lumencor®) were projected onto the sample. Transmitted and emitted light were filtered using a triple-edge dichroic beamsplitter (409/493/596 nm, Semrock®). To simultaneously image GCaMP and mKate2, a dual view with a 585 nm beamsplitter (DV2, Photometrics®) was used. Each channel was projected onto a half of an sCMOS camera (Zyla, Andor®) at 30 Hz acquisition rate with an exposure time of 33 ms and a 16 bit read-out depth.

2.2.4.3 Touch stimuli delivery

Substrate vibrations were delivered using a piezo buzzer as described in section 2.1.4.4. We added a magnetic mount to our 3D-printed holder to minimize motion artifacts during the stimulation without damping vibrations transmission (Fig. 3.26.B). The piezo element was driven by a 1 s 630 Hz sinusoidal voltage at various amplitudes (0, 2.5, 5, 10, 15, and 20 volts peak to peak (V)).

The fluorescence images acquisition, the stimulus delivery and the synchronization with the camera acquisition were controlled by a data acquisition card (BNC-2090A, National Instruments®) driven by a customized program (LabVIEW; National Instruments®).

For imaging TRNs, animals were acclimated to blue light under the microscope for 20 s before being exposed to stimuli with an increasing intensity. Each recording consisted of a single stimulus exposure, including a 20 s pre-stimulus period and a 60 s post-stimulus period. For imaging the RIP and I1 neurons, a shorter ramp protocol with 10 s blue light acclimation and 10 s inter-buzz interval.

2.2.4.4 Ratiometric analysis

The resulting images were automatically split into individual channel images and registered for an optimal overlay using a customized Matlab script. Using the mKate2 channel images, manually defined regions around posterior lateral microtubule (PLM) neurons pair including background were cropped in Fiji (Schindelin et al., 2012). Within each region, the neurons were tracked using the Fiji plugin TrackMate (Tinevez et al., 2017) defining a circular ROI around the neuron. Fluorescent signals were calculated as the 95 percentile of the intensity in the circular ROI using Python. Similarly, the local background was calculated as the 5th percentile and subtracted from the signal, and the resulting curves were bleaching-corrected by dividing by the overall signal decay as described by a fit with a single exponential. Then, the green to red ratio was calculated as followed:

$$R = F_{\text{green}}/F_{\text{red}}$$

Then the ratio was normalized to the baseline ratio (R_0):

$$normR = R/R_0$$

The percentage of the ratio change compared to baseline was calculated as follows:

$$\Delta R/R_0 = (normR - normR_0)/normR_0 \times 100$$

where R_0 and $normR_0$ are the time-averaged ratios 5 s before the stimulus onset.

The normalized ratio between the GCaMP and red fluorophore in the RIP neurons is shown in 3.25.

2.3 Simultaneously measuring feeding and neuronal calcium signal in response to touch in behaving animal

2.3.1 Preparation of micro-chambers for imaging

A 3 x 3 array of micro-chambers was cast in 10 % agarose using a customized 3D-printed mold (**Fig.** 3.26.A). The array was designed to fit within the 5 × 7 mm copper ring window used in the previous behavioral and calcium imaging assays (see Sections 2.1.3.1 and 2.2.2) and to be sealed with a 4 mm diameter cover glass (#1, Multichannel Systems). Each chamber (250 × 500 × 30 µm) was sized to accommodate a single adult worm, providing sufficient space for movement while restricting motion in the z-dimension. The agarose arrays were prepared up to one week prior to recording and stored at 4℃ in M9 buffer.

On the day of recording, the micro-chamber array was seeded with 5 µl of 10x concentrated *E. coli* OP50 and allowed to dry for one hour. Animals were transferred to a drop of M9 buffer on an unseeded NGM plate for 10 min to clear them of residual bacteria. Subsequently, 2-5 animals were transferred into the micro-chamber array, which was then sealed with the cover glass. Animals were acclimated for at least 30 min in the imaging room before recording began.

2.3.2 Dual near-infrared and epifluorescence imaging

Ratiometric imaging in single neuron was performed as previously described for the immobilized animals using our in-house built epifluorescence microscope. The acquisition rate was reduced to 20 Hz (from 30 Hz) due to computer memory limitations (see **Section** 2.2.4.2).

Pharyngeal pumping was simultaneously imaged using a dedicated near-infra red (NIR) channel. A customized ring holder fitted with 860 nm LEDs (OSRAM SFH 4053; 860 nm, 60 mW) was 3D-printed and mounted onto the stimulus device (**Fig.** 3.26.B). This NIR-LED ring was designed to provide back-scattered illumination for resolving the pharynx's anatomical structures, particularly the grinder. The NIR light was collected using the same objective as for the fluorescent signal (S Plan Fluor LWD, 20 ×/0.70 NA., Nikon). Fluorescent and NIR light were split using a 785 nm beamsplitter (FF776-Di01, Semrock®). NIR-light was further pass-band filtered (819/44 nm, Brightline, Semrock®) and projected into the camera sensor (acA3088-57um; Basler®) through an additional objective (MVL50TM23, 50 mm EFL, f/2.8, 2/3", Thorlabs®) that allows to adjust the focus to the grinder while focusing neurons at different focal plan. The NIR light was collected using the same objective as the fluorescence signal (Nikon S Plan Fluor LWD, 20×/0.70 NA). The fluorescent and NIR light were separated using a 785 nm longpass beamsplitter (FF776-Di01, Semrock®). The NIR light was then pass-band filtered (819/44 nm, Brightline, Semrock®) and projected onto the camera sensor (acA3088-57um, Basler®) via an additional objective (MVL50TM23, 50 mm EFL, f/2.8, 2/3", Thorlabs®). This secondary lens allowed for a finer adjustment of focus on the pharynx independently from the focal plane of the neurons. Images were acquired at 30 Hz with an exposure time of 33 ms and a 8 bit read-out using the camera manufacturer's software (Pylon viewer, R7.2.0.25592, Basler®).

2.3.3 Touch stimulus delivery

Substrate vibrations were delivered using a piezo buzzer as described in section 2.2.4.3. The piezo element was driven by a 1 s 630 Hz sinusoidal voltage at 5 or 20 volts peak to peak (V). After transfer to the microscope, animals were allowed to recover for 5 min, followed by a 20-s blue light acclimation period prior to three paired trials. Animals were expose to a single buzz per trial, for a total of 6 trials—3 pairs of randomly assigned 5 V and 20 V trials. Each trial consisted in 20 s pre-stimulus and 60 s post-stimulus.

2.3.4 Analysis

2.3.4.1 Spatial correction of fluorescent signals

Spatial illumination inhomogeneity, inherent to both the optical system and the imaging substrate, was corrected on a per-channel basis. For each fluorescent light channel, a reference image of an empty chamber was acquired at the end of the imaging session using the identical excitation intensity as during recordings.

To match the dynamic range of the experimental data, each background image was intensity-scaled. The scaling coefficient was calculated as the ratio of the maximum pixel intensity within a representative, empty ROI in a raw image to the maximum intensity in the corresponding background image ROI. Raw images were then corrected by subtracting the scaled background image (coefficient × background). Measurement and correction were done in Fiji (Schindelin et al., 2012).

2.3.4.2 Neuron tracking and ratiometric measurement

Background subtracted green and red channel images were merged in FiJi without further registration. Neurons were tracked using the LoG detector and LAP tracker in TrackMate (Tinevez et al., 2017). Each track was visually inspected and tracking error manually corrected. The average intensity values were calculated for both green and red channels from a ROI with a 21 px radius around the soma.

For correcting motion and focusing artifacts, ratiometric measure was calculated by scaling both channels using the 5^{th} and 95^{th} percentiles of the intensity in each channel. The ratio, R, was calculated from the normalized red and green intensity and normalized to the pre-stimulus mean $R0$ as follow:

$$R = \frac{F_{\text{green}}}{F_{\text{red}} + 1} \cdot \frac{1}{R0} \tag{2.1}$$

A remaining spatial correlation of the signal due to imperfect sample flatness and focus was corrected by linear regression of the x and y position against the ratiometric calcium activity R. The resulting signal was then normalized to obtain a pe-stimulus mean of 1.

Data was linearly upsampled to obtain a resulting frame rate of 30 FPS, matching the behavioral NIR data.

2.3.4.3 Manual annotation of pharyngeal pumping

Manual counts of pharyngeal pumping events were performed by visual inspection of the simultaneously acquired NIR images, using the napari image analysis platform (napari contributors, 2019). A pumping event was counting when the grinder moves to its most posterior position within the terminal bulb or at full opening of the pharynx's anterior lumen when grinder was not visible. This opening results from muscles contractions. All other images were annotated as 0 events. Images when the grinder or anterior tube was not visible were reported as unknown and excluded from the analysis.

Pumping events were binned into 1 s bins, and the pumping response was calculated as percentage change of the time-average 10 s after relative to 10 s before stimulus onset.

3. Results

3.1 A non-invasive method to automatically measure feeding in freely moving *C. elegans*

3.1.1 Pharyngeal pumping can be been monitored automatically in crawling animals

To enable automated, high-throughput detection of pumping in animals crawling on culture plates, we combined epifluorescence microscopy with a large area scan camera (**Fig. 3.1.A**). Typically, pumping is detected by manual or automated counting using high magnification to resolve the motion of the grinder in the terminal bulb (Bhatla et al., 2015; Dallière et al., 2016). Using animals expressing a fluorescent protein in the pharyngeal muscle allowed us to image at a lower magnification compared to the resolution required for bright-field imaging of the grinder. Specifically, we imaged animals expressing YFP under the pharyngeal promoter *myo-2* (strain GRU101, in List of Transgenic Lines), which is present in all pharyngeal muscles except pm1 and pm2 (Okkema et al., 1993; Okkema & Fire, 1994).

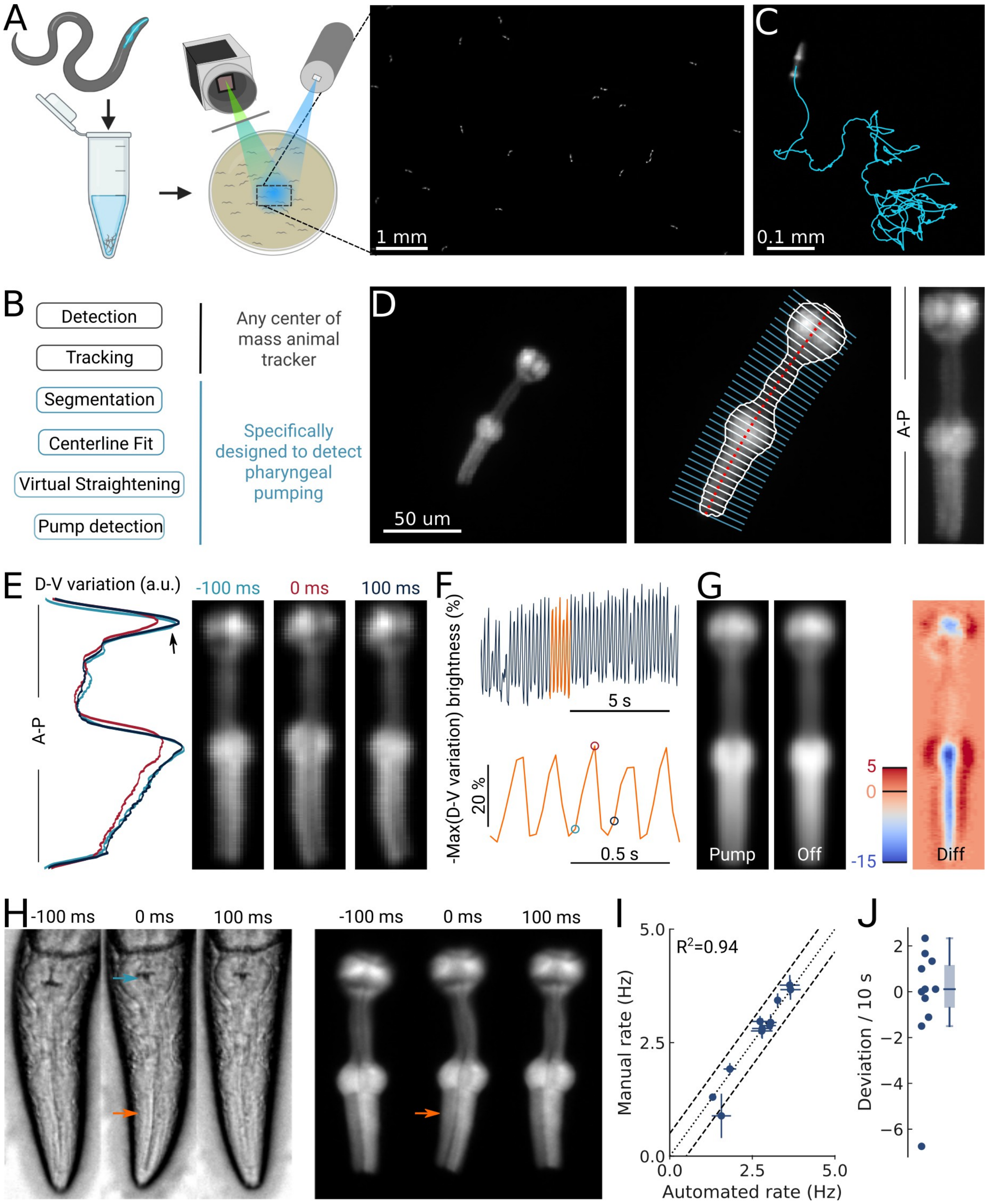

Figure 3.1: High-throughput optical detection of pharyngeal pumping in moving *C. elegans*. (Caption continued on the next page)

Figure 3.1 (continued). High-throughput optical detection of pharyngeal pumping in moving *C. elegans*. (A) Hundreds of animals expressing *myo-2p*::YFP are washed in M9 and pipetted onto the assay plate before imaging with an epifluorescence microscope at 1x magnification resulting in a full field of view of 7 by 5 mm. (B) Workflow of using the PharaGlow image analysis pipeline. Animal center of mass tracking can be substituted with any available tracker, but subsequent steps are specific to tracking pumping. (C) Representative trajectory of an animal after tracking. (D) Processing steps followed for detection of pharyngeal pumping. Example of a fluorescent image (left; 2x magnification). Segmentation of pharyngeal contour, centerline, and widths (middle) calculated for virtual straightening along the anterior-posterior axis (A–P) and the resulting straightened animal (right). (E) Three straightened frames of an animal before, during, and after a pump and their dorso-ventral variation in brightness along the A-P axis. (F) The metric that is used to detect pumping events. Bottom, a portion of the top trace (orange). Highlighted time points correspond to the images in (E). (G) Average of all images during a detected pump (‘Pump’) and for all remaining time-points (‘Off’). The difference image (‘Diff’) shows that pumps are characterized by the opening of the lumen and terminal bulb contraction. Colorbar indicates brightness difference (a.u.). (H) Example image sequence of a pharynx recorded at 10x using bright-field (left) and in epifluorescence (right) microscopy before, during, and after a pump. Arrows denote changes in the terminal bulb (cyan) and corpus (orange). (I) Correlation between the average pumping rates for the expert annotator and PharaGlow (N = 11 animals). (J) Deviation of the number of events between the expert and PharaGlow reported as the number of events in 10 s, a typical time period used in manually counted experiments.

By using a low magnification of 1x, we could image a field of view of 7 by 5 mm, corresponding to multiple body lengths of the worms (**Fig.** 3.1.A). We simultaneously imaged tens of animals (typically 30–50) as they crawled and analyzed their behavior off-line using our custom analysis software (**Fig.** 3.1.B). The analysis pipeline combines a particle-tracking workflow with custom shape segmentation of the fluorescent pharynx (**Fig.** 3.1.C). After detecting and tracking the pharynges in the field of view, the contour and centerlines are fitted. The centerline and width are used to virtually straighten the animal (**Fig.** 3.1.D). We then extract a pump metric from the straightened images based on the standard deviation of the fluorescence along the dorso-ventral axis (DV-axis) of the animal, which reflects pumping events (**Fig.** 3.1.E and F). By averaging images during these putative detected pumping events, we determined that this metric is sensitive to the opening of the pharyngeal lumen and contraction of the terminal bulb and thus indeed corresponds to pumping events (**Fig.** 3.1.G).

Although the low magnification (1x) we use to image the animals allows us to increase the number of observed animals, this could compromise pumping detection. To determine how accurate our software detects pumping in these imaging conditions, we compared the results of our automated method and a manual annotator. Since manual annotation of pumping rates is still widely used, but practiced at higher magnifications, we simultaneously imaged animals at a magnification of 10x (pixel size 240 nm/px) in bright field and fluorescence (**Fig.** 3.1.H). A human expert counted pumps in the images acquired using the bright-field channel. We then ran our automated analysis on the images acquired on the fluorescence channel, but downscaled to 1x (pixel size 2.4 µm/px). We found that PharaGlow was able to accurately detect pumping in these images, and the resulting rate and counts were in agreement with the human expert. Both methods result in a comparable mean pumping rate for the animals counted (**Fig.** 3.1.I), with a deviation between the human and automated results of less than 2 pumps per 10 s (**Fig.** 3.1.J). To score a typical experiment of 30 animals over 5 min of recording time, the human experimenter would need, at best, to count for at least 150 min of data (real time). This time is regularly longer, as accurate counting often requires scrutinizing the recordings in slow motion or visualizing the same part of the recording several times. PharaGlow is therefore able to automatically and reliably detect pumping in low-resolution, large field of view images, enhancing the number of animals which can be scored simultaneously.

3.1.2 Pumping rate increases over the development

Having developed this new high-throughput method which enables accurate measurements of many animals simultaneously, we wondered how pumping changes over the course of development, where the animal changes its size and its energy needs. During development, the pharynx grows with the body (Knight et al., 2002), but the ratio between pharynx and body length decreases from the first Larva stage, L1, to adulthood (Avery & Shtonda, 2003). To investigate how pumping rates change during development, we imaged cohorts of synchronized animals consecutively over three days in the middle of each of the four larval stages and as young adult (YA). Animals were imaged directly on their culturing plates while moving freely in the field of view (**Fig.** 3.2.A). We accounted for the growing pharynx by adapting the magnification of our imaging system to achieve approximately the same spatial sampling of the pharynx at each stage (**Fig.** 3.2.B). Under these conditions, we were able to sample at least 150 trajectories per developmental stage. Altogether, more than 1000 animal tracks remained after filtering animals that spend less than one minute in the field of view. Filtering leads to over-proportionally reducing young adult trajectories since these animals traverse the field of view quickly despite the spatially proportional scaling. Nevertheless, we obtain large samples of animals due to new animals continually entering, with a total measured time of four animal-hours for the adult stage, and more than 10 animal-hours for the L1 stage. The average track duration is well over one minute with 1.9 ± 0.9 min (mean ± STD) for L1 and 1.6 ± 0.6 min for adults.

These data represent up to two orders of magnitude more single worm pumping data than is obtainable with conventional methods (see **Tab.** 1.1).

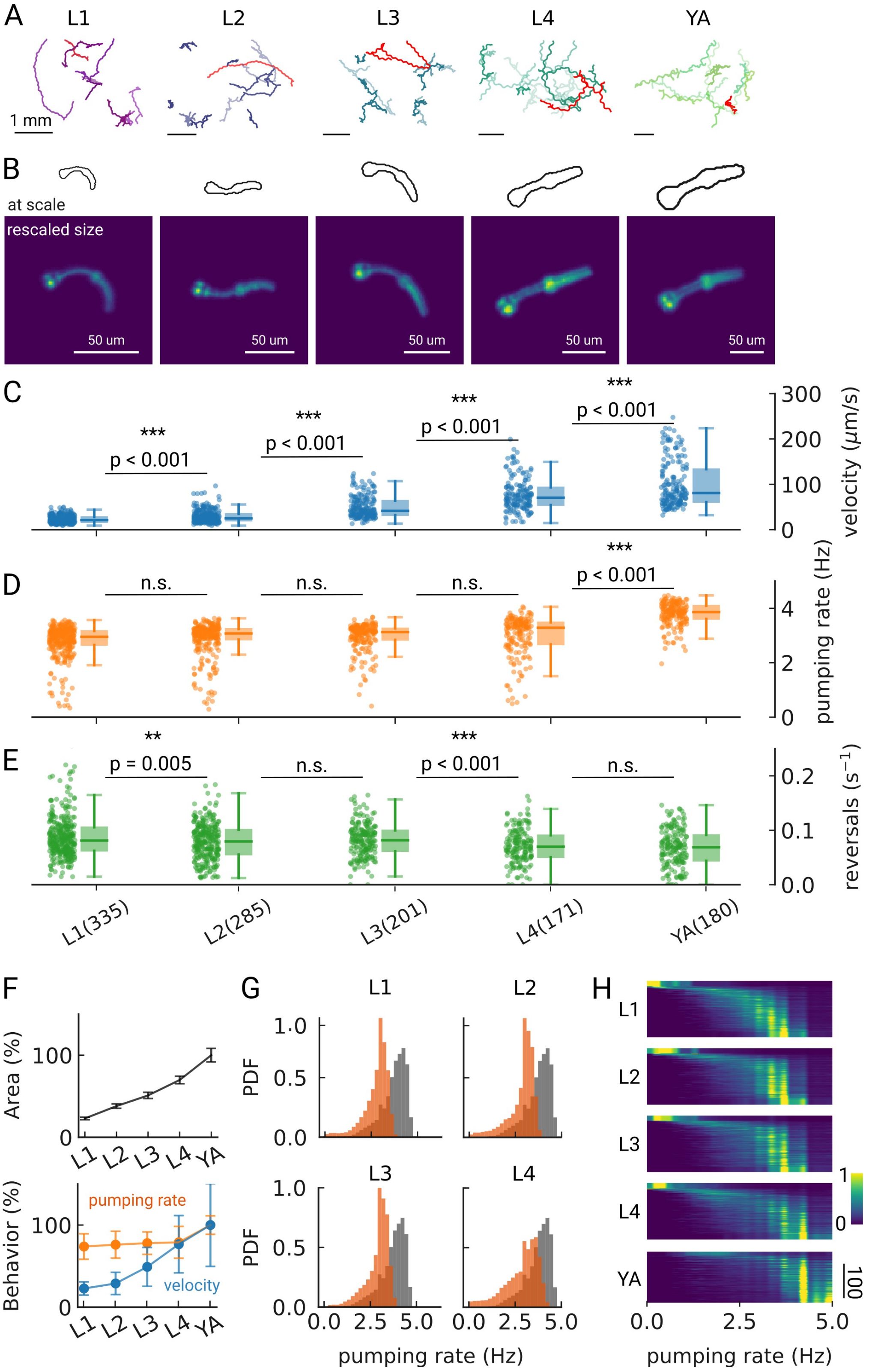

Figure 3.2: Pumping rate and speed increase during development. (Caption continued on the next page)

Figure 3.2 (continued). Pumping rate and speed increase during development.(A) Trajectories of 10 randomly selected animals at different larval stages (L1–L4) and young adults (YA). All scale bars correspond to 1 mm (top). (B) Size of the larvae and YA at the same scale (outlines, top) compared to the equal sizing achieved by adjusting the magnification (bottom). The image corresponds to the red track from (A). (C–E) Time-averaged mean velocity (C), (D) mean pumping rate, and reversals (E) for all animals. The box-plots follow Tukey's rule where the middle line indicates the median, the box denotes the first and third quartiles, and the whiskers show the 1.5 inter-quartile range above and below the box. The number of tracklets per developmental stage are shown in (E), with N = 6 independent replicates per condition. (F) Relative change in the animal's area compared to the mean area of the YA stage (top) and relative change in velocity (blue) and pumping rate (orange) across development compared to the mean of the YA stage (bottom). Error bars denote STD (G) Pumping rate distribution for all larval stages as calculated by counting pumping events in a sliding window of width = 10 s and combining data from all animals of the same stage. The YA pumping rate distribution is underlaid in gray. (H) Pumping frequency distribution of individual animals for different developmental stages and YA.

We find that on-food pumping rates increase slightly over the course of the larval stages, but much less dramatically than the velocity increases over development, despite the substantial growth of both the body and the pharyngeal muscles (**Fig.** 3.2.C–F). Owing to time resolution and the large number of individual animals that can be analyzed using PharaGlow, it is possible to generate smooth probability density functions of pumping across the different larval stages (**Fig.** 3.2.G). A small fraction of animals did not show pumping during our recording (**Fig.** 3.2.H, 5 animal tracks in L1 with < 0.5 Hz, < 1 % for all other conditions). We wondered if we had captured animals during lethargus, the period of sleep preceding each molt despite choosing the imaging time points in the middle of each larval stage and working with an age synchronized population. However, lethargus is incompatible with the observed velocities of these animals. Alternatively, it is possible that these animals transiently show satiety quiescence, which might be absent under these conditions in the larger YA population (Davis et al., 2018; Gallagher et al., 2013; You et al., 2008).

As we image unrestrained animals, we can simultaneously assess pumping and locomotor behaviors. Animals move forward on agar by generating waves of muscular contraction through their body. When the animals reverse the direction of these waves, they move backwards. Such spontaneous reversals are rare events, but can be triggered by diverse stimuli, such as nose touch (Chalfie et al., 1985) or heat (Zhao et al., 2003). The reversal rate depends also on the food condition and the developmental stage of the animal. In the absence of food, the reversal rate is higher in young adults than in larvae (about 45 events vs 30 events in 10 min), but constant throughout larval development (Chiba

& Rankin, 1990). In our on-food measurements, we find some significant differences in reversal rates, however, the effect size is small (e.g. corresponding to a rate of 47 vs 49 pumps/10 min between L2 and L3 animals). The only strong difference appears between the earlier larvae L1-L3 and the later L4/young adult stages with a difference of approximately 10 reversals /10 min (**Fig.** 3.3).

Overall, we find that our imaging approach can be adapted to larvae by increasing the magnification, and our analysis pipeline is capable of handling data from hundreds of animals. While there are small deviations between the automated detection and human counted data (See 3.3), we accurately detect both mean and individual rates for all stages, with a median of error between experts and our method of less than 10 %. Over the course of three days and five imaging sessions, more than 1000 animals were tracked, significantly more than can be achieved with comparable methods (see **Tab.** 1.1).

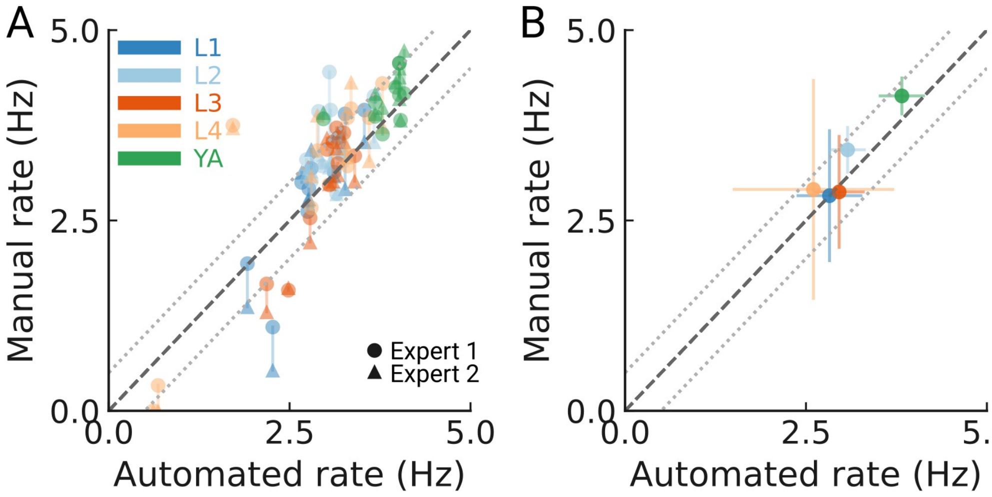

Figure 3.3: Consistent detection accuracy over all developmental stages. (A) Manually counted pumping events for 10 animals per stage (color coded) from two independent experts compared to the automated tracking. Counts of each expert are shown as a circle or triangle. The dashed line indicates unity; the dotted lines denote a 0.5 Hz difference in the resulting pumping rate. (B) The mean pumping rates per developmental stage from the experts and automated method (N = 10 animal tracks per stage). The error bars are STD between animal tracks. The two expert counts were averaged to obtain one mean count per animal. The dashed line indicates unity; the dotted lines denote a 0.5 Hz rate difference.

3.1.3 Food intake is modulated by starvation

Next, we wanted to determine if our method was robust to changes in locomotion and plate context, allowing a wider range of applications such as investigating starvation or different pharmacological treatments without the presence of a bacterial food source. Off-food locomotion is faster (Dillon et al., 2016; Gray et al., 2005), and pumping irregular (Lee et al., 2017; Scholz et al., 2016), which could potentially be more challenging for detecting pumping. Prior work showed that pumping rates off food are lower, but increase over the course of starvation and that this increase is mediated by a cholinergic pathway (You et al., 2006). We track animals either on-, or off food over an increasing amount of starvation time and extract behavioral dynamics (**Fig.** 3.4.A–D). We confirm that pumping is dependent on the starvation duration, with a reduction in pumping rate over the course of three hours (**Fig.** 3.4.B, D). Beyond the first time point, our data are consistent with prior data (You et al., 2006), showing a sustained rate of around 2–2.5 Hz (**Fig.** 3.4E). Previously, rates measured immediately after transferring animals off food (<30 min of starvation) were very low, possibly due to a lasting pumping suppression after harsh touch (Keane & Avery, 2003), which we avoid by washing animals off plates instead of picking (see Methods).

As we are able to measure pumping and locomotion behaviors simultaneously, we wanted to see if we could observe co-regulation of locomotion and feeding off-food. When taken off of food, *C. elegans* displays a restricted area search (local area search) which is characterized by frequent turns and reversals and an elevated speed (Calhoun et al., 2014; Gray et al., 2005; Hills et al., 2004; Sawin et al., 2000). This behavior lasts between 30 and 60 min, after which animals switch to longer runs that cover more area, which is a strategy for dispersal (Hills et al., 2004; Wakabayashi et al., 2004). Interestingly, for starved animals at 30 and 90 min, the joint distribution of pumping rates and velocities show distinct sub-populations (**Fig.** 3.4.F). For longer starvation durations, the population becomes homogeneous with a well-defined mean pumping rate and speed. For the shortest starvation time point we sampled, we see a mixed population with distinct speeds and pumping rates, possibly reflecting some animals that are still performing a local search and others that are not. This is consistent with the fact that these distinct populations are not apparent in worm populations that stay on food (**Fig.** 3.5).

To further investigate the origin of the two sub-populations observed at short starvation time, we analyzed the pumping rate distributions of individual animals (**Fig.** 3.4.G). Taken together, the data suggests that at 30 min starvation, a fraction of the animals show low speeds and pumping rates, and the remainder are in a high-speed, high pumping state (**Fig.** 3.4.F, G). This suggests two possible interpretations. First, it is possible that, with increasing starvation time, a subset of animals transitions to lower pumping rates until all animals show a similar pumping rate distribution with an average of 2 Hz. Alternatively, the two sub-populations could result from transient behavioral changes among animals to high pumping rates. These transitions would occur less frequently with increasing starvation time. To discern among these two possibilities would require measuring single animals over longer periods of time. Further studies are required to reveal these population dynamics upon starvation.

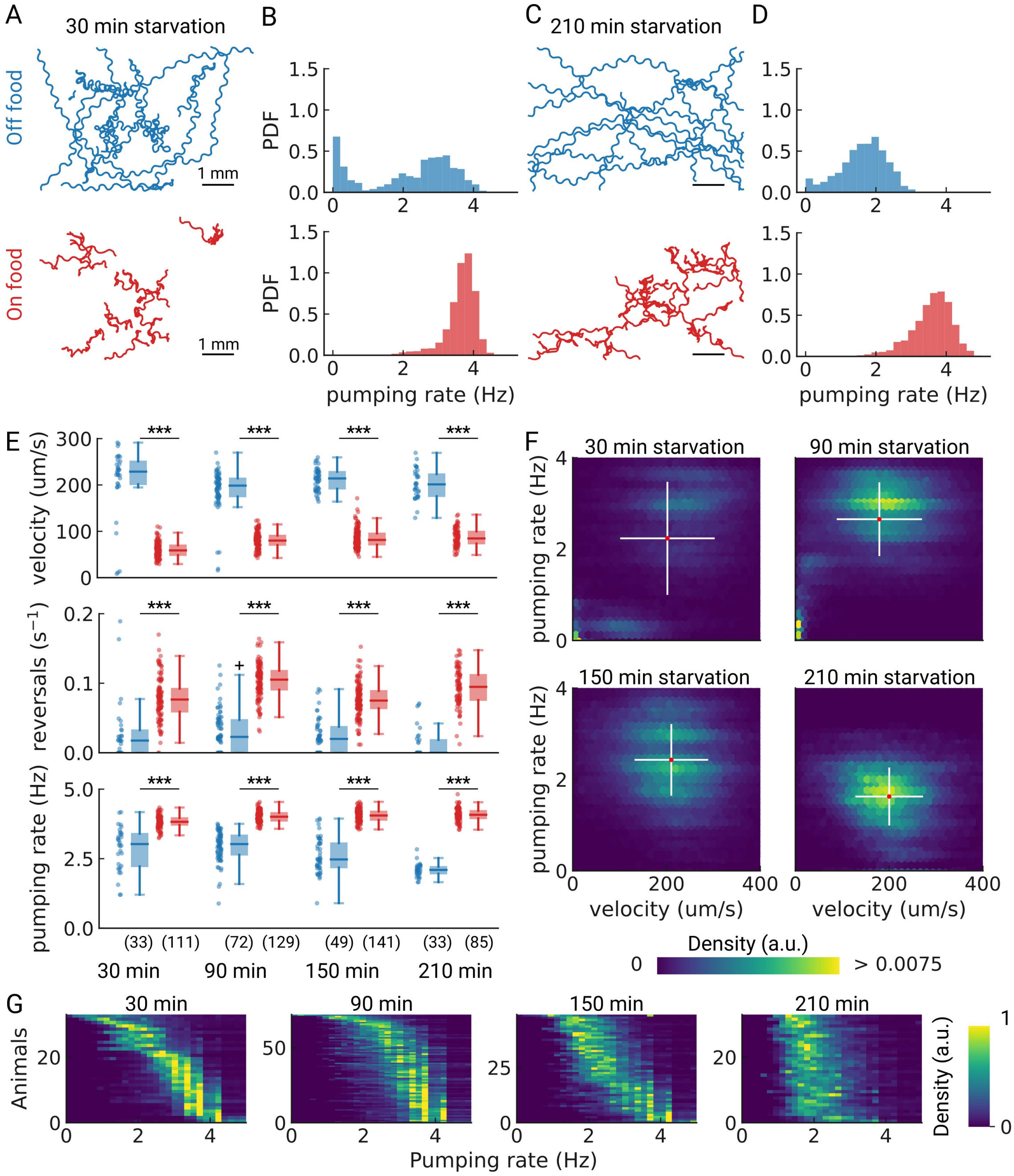

Figure 3.4: Pumping is modulated by starvation.(Caption continued on the next page)

Figure 3.4 (continued). Pumping is modulated by starvation. (A) Example trajectories of worms after 30 min starvation (blue) or 30 min continuously on food (red), N = 10. (B) The pumping rate distributions for the conditions in (A) for all animals ($N_{starved} = 33$, $N_{onFood} = 111$). (C) Same as (A) but for animals starved, or kept on food for 210 min. (D) The pumping rate distributions corresponding to (C; $N_{starved} = 33$, $N_{onFood} = 85$). (E) velocity, reversal rate, and pumping rate for animals starved and on-food controls. The sample size is given in the bottom panel. *** indicates $p < 0.001$ (Welch's unequal variance two-tailed t-test). The sample size is given in parentheses in the bottom panel. (F) Joint distribution of velocity and pumping rate for increasing starvation times. The cross indicates the mean (red) and standard deviation (white). The density is normalized by sample number. (G) Distribution of instantaneous pumping rates for each animal (tracklet). Rows are sorted by the mean pumping rate to aid visualization.

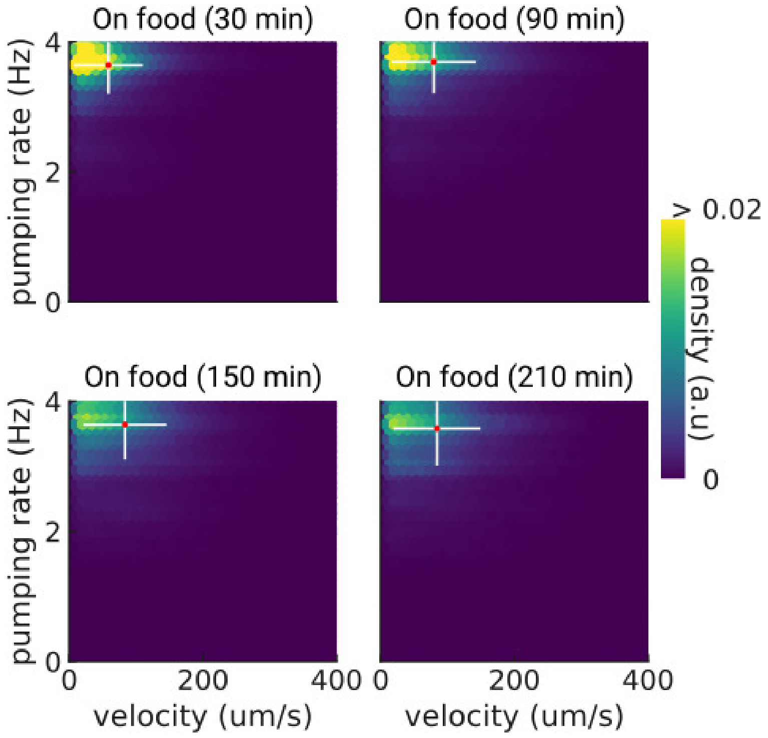

Figure 3.5: Correlation between velocity and pumping rate for increasing times on food. The cross indicates the mean (red) and standard deviation (white). The density is normalized by sample number

3.1.4 Pumping rate is modulated at multiple timescales during mating

Having established that PharaGlow can robustly detect locomotion and pumping behaviors across a range of conditions, we wanted to test if it is a suitable tool for long-term recordings. As a proof of principle, we imaged the interactions of a male and a hermaphrodite over the course of 74 min at 30 FPS (**Fig.** 3.6.A and B).

As the resulting data volume would have been prohibitive, we implemented a live segmentation method that allowed us to only store the animals coordinates and the region of interest around each animal. We then calculated the distance between the animals, allowing us to identify mating events (**Fig.** 3.6.C and D). We find that the animals frequently interact over the course of 1 h with multiple close encounters (**Fig.** 3.6.D). The male also showed a long period of quiescence in both locomotion and pumping rate. Overall, the animals are closer at the beginning of the recording, but later spend time at larger distances (**Fig.** 3.6.E, left and right panels). Despite the long imaging duration, we still observe pumping at the end of the recording, indicating that we have sufficient signal remaining to detect pumping events. We confirm this observation by calculating photo-bleaching curves. We find that the decay time of the signal is 410±47 min (**Fig.** 3.7), which indicates that it is possible to do continuous imaging over multiple hours. In this case, the recording was limited by the male escaping the enclosure, rather than loss of signal.

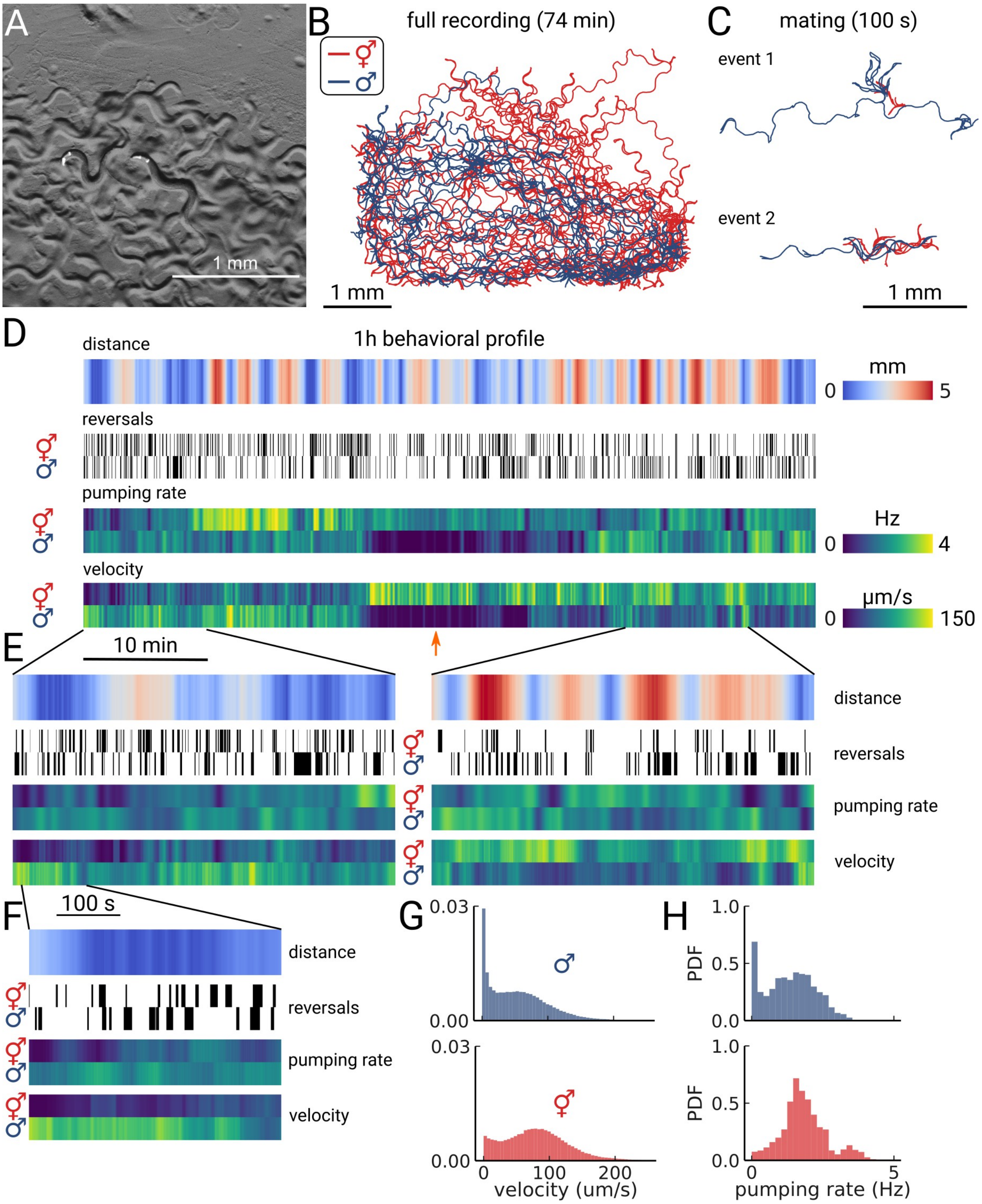

Figure 3.6: Pumping rate is modulated at multiple timescales during mating. (Caption continued on the next page)

Figure 3.6 (continued). Pumping rate is modulated at multiple timescales during mating (A) Composite image of the two animals in the arena while exposed to bright-field illumination and exciting fluorescence of YFP using green light. On the right, the hermaphrodite, on the left the male identifiable by its smaller size and its tail with sensory rays and fan. (B) Trajectories obtained from the full recording of the male (blue) and hermaphrodite (red). (C) Example mating events. (D) Behavioral measures for 1 hr of data. The distance between the animals, the reversal events, pumping rate, and velocity are shown for the hermaphrodite and the male. The male shows an extended period of quiescence (orange arrow). (E) Behavioral measures for 10 min of data and (F) 100 s of data corresponding to the mating event 1 in panel (C). (G) velocity distribution and (H) pumping rate distribution for the male and hermaphrodite.

Having this multi-scale data allows observing both large-scale structure and smaller events in the data. We further examined the mating event displayed in **Fig.** 3.6.C. During the encounter, the male shows a larger velocity and performs many long reversals when the animals are close, as is typical for a mating attempt. It is also interesting to note that pumping does not completely cease during the attempt (**Fig.** 3.6.F). Despite being in the same arena, and covering most of the enclosure during the recording (**Fig.** 3.6.B), the velocity and pumping distributions differ strongly between the two animals (**Fig.** 3.6.G and H). While the distributions of the male are dominated by the long quiescence period, the hermaphrodite overall shows a bi-modal rate distribution with some infrequent pumping at 4 Hz. PharaGlow is therefore able to track behavior over more than an hour, and keep the identity of animals given that these are constrained to the field of view.

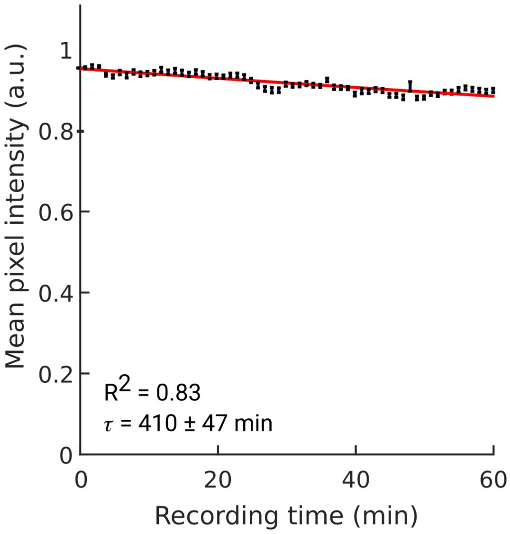

Figure 3.7: Negligeable YFP photobleaching in long-term recording during continuous acquisition at 30 FPS (×1 magnification). Stroboscopic illumination was used (5 ms light pulses; see Methods). Average of N = 11 animals. Individual animal bleaching curves were normalized to unity at t = 0. The fit to an exponential decay function yields a decay rate of 410±47 min (95 % confidence bounds). Error bars indicate standard error of the mean (SEM) across animals.

3.1.5 Pumping and locomotion patterns determine feeding mutants

A desired capability for a high-throughput feeding tool is the ability to faithfully detect pumping rates in mutant animals which might have different pharyngeal contraction patterns and body motion, potentially increasing the difficulty of detecting pumping events. To determine if PharaGlow could faithfully detect pumping and locomotion in mutant animals, we wanted to assay a range of feeding and locomotion phenotypes. We therefore selected mutants with reported constitutively high (*unc-31*, strains INF5 and INF17 in List of Transgenic Lines) or reduced (*eat-18*, strain INF44 in List of Transgenic Lines) pumping rates and different locomotion patterns (Avery, 1993; McKay et al., 2004; Raizen et al., 1995). UNC-31 is involved in dense-core vesicle release, and *unc-31* mutant animals display reduced, uncoordinated locomotion on food (**Fig.** 3.8.A). We confirm that *unc-31(e928)* and *unc-31(n1304)* animals pump at rates comparable to wild-type. However, we see a bimodal distribution of rates with a fraction of animals showing markedly lower rates (**Fig.** 3.8.B). By looking at the individual animals' pumping rates, we find that *unc-31* animals show long pauses in pumping, unlike wild-type animals (**Fig.** 3.8.F).

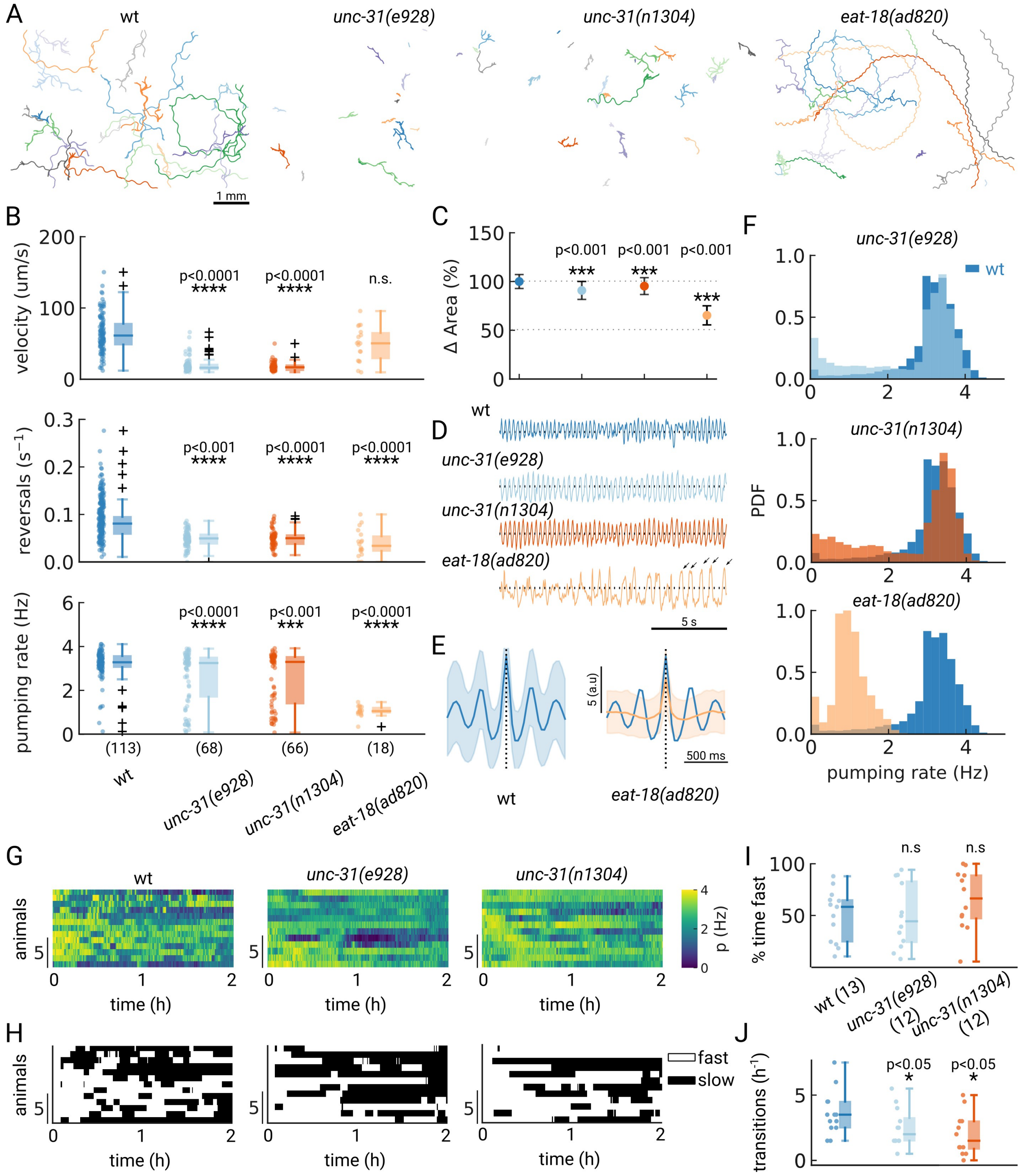

Figure 3.8: Pumping and locomotion patterns determine feeding mutants. (Caption continued on the next page)

Figure 3.8 (continued). Pumping and locomotion patterns determine feeding mutants. (A) Example trajectories of tracked animals (N = 20, except N = 18 for *eat-18(ad820)*). (B) velocity, reversal rate and pumping rate for all genotypes. The sample size is given in parentheses in the bottom panel. (C) Mean and standard deviation of the pharyngeal areas relative to wild-type. (D) Pumping metric for a representative sample animal per genotype. Arrows in the *eat-18(ad820)* trace denote slow contractions. (E) Average peak shape of the pumping signal for wild-type (wild-type, blue) and *eat-18(ad820)* (orange). The shaded area denotes STD (F) Pumping rate distributions. The wild-type pumping rate distribution is underlaid in dark blue. (G) Heatmap of the pumping rates for animals recorded over 2 h. (H) Heatmap thresholded to determine 'fast pumping' (defined as pumping rate > 2.5 Hz) and 'slow pumping' states. (I) Fraction of time spent in fast pumping of each animal and (J) the number of state transitions (slow to fast and fast to slow) for each animal in (H). Significant differences between a mutant and wild-type are indicated as * ($p < 0.05$), *** ($p < 0.001$) and **** ($p < 0.0001$). Welch's unequal variance two-tailed t-test was for the large sample size measurements (B, C). For (I–J) significance differences were assessed with the Mann-Whitney-U test.

In contrast to *unc-31*, *eat-18* mutant animals have no previously reported locomotor defects, but pump slower than wild-type (McKay et al., 2004). EAT-18 is expressed in the pharyngeal muscle and interacts with a nicotinic acetylcholine receptor (nAChR) subunit EAT-2 to form a functional acetylcholine receptor (Choudhary et al., 2020; Raizen et al., 1995). Feeding impaired mutants were previously reported to have reduced body lengths and widths (Mörck & Pilon, 2006). As expected, we found that *eat-18* animals were smaller (**Fig.** 3.8.C) and developed more slowly (approximately 91 hr from egg to adulthood compared to 63 hr for wild-type). While we detected pumping events at an average rate of 1 Hz, the animals showed a different contraction pattern and timing than either *unc-31* or wild-type animals (**Fig.** 3.8.D and E). We confirmed that *eat-18(ad820)* animals lack the ability to perform fast pumping bursts (**Fig.** 3.8.B and F) and the duration of a pharyngeal contraction is approximately doubled compared to wild-type (**Fig.** 3.8.E;**Fig.** 3.9). We do observe a higher pumping rate than previously reported for *eat-18*, where animals were reported to rarely pump during experiments (<0.5 Hz, (McKay et al., 2004; Raizen et al., 1995)). To verify that the detected motion is pumping and not peristaltic movements or other non-pharyngeal muscular motion, we verified the rate by inspecting individual recordings. When verifying these sample animals, we did observe slow pumping bursts at the 1–2 Hz rates indicated by PharaGlow, suggesting that these animals are able to pump at this frequency (**Fig.** 3.1.E). We also found that *eat-18* animals showed significantly fewer reversals than wild-type, indicating a role for nAChR in modulating reversals. This is likely mediated by extrapharyngeally located neurons, since *eat-18* is reported to show expression not only in the pharyngeal muscle, but also in some unidentified somatic neurons (McKay et al., 2004).

Considering the split distribution of mean pumping rates we observed for *unc-31* in our short term (5 min) recordings (**Fig.** 3.8.B), we wondered if these distributions reflect a persistent difference between animals or if instead the animals perform infrequent switches between high and low pumping rate states. We therefore tracked animals for at least three hours on food, restrained to our field of view using a copper enclosure. By confining only a few animals (<5 in the field of view), we were able to maintain animal identity over the course of the experiment and quantify their pumping rate over at least 2 hr (**Fig.** 3.8.G). To further investigate the different persistence of pumping across the different animals, we quantified the transitions between states of pumping and no or low pumping rates. We define a 'fast' state as a period at which the animals pump at > 2.5 Hz and 'off' states as the converse (see also a similar analysis in Lee et al. (2017)). Wild-type animals displayed frequent switching between low and high pumping rates (**Fig.** 3.8.H and J). In contrast, *unc-31* animals displayed infrequent switches, consistent with prior reports of constitutive pumping (Avery & Horvitz, 1990) and the role of neuropeptides such as PDF in regulating switches between foraging states (Flavell et al., 2013).

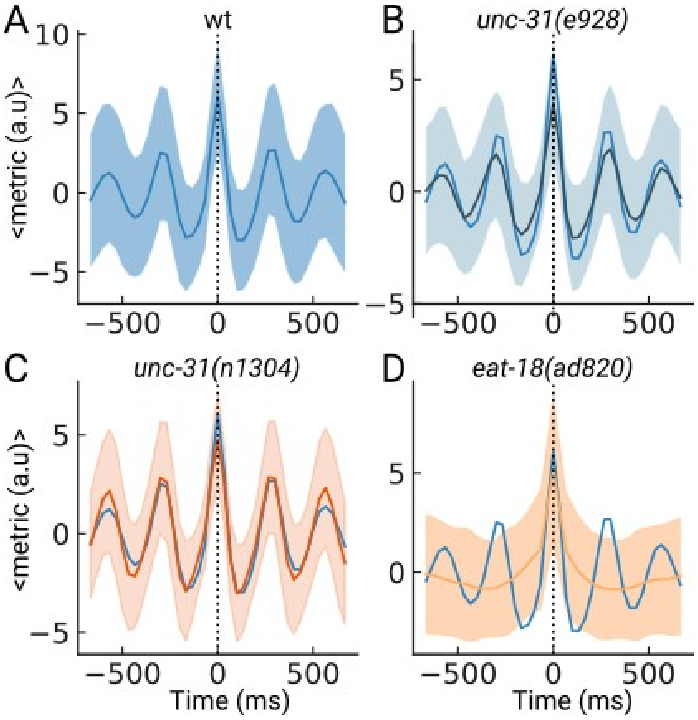

Figure 3.9: Impaired pharyngeal pumping dynamics in mutants as shown by the peak-triggered average of the pumping metric. (A) Average of the pumping metric around the detected peaks of N = 10 randomly selected sample animal tracks. The shaded area denotes the standard deviation. (B), (C), (D) same as (A) but the wild-type peak shape is underlaid in dark blue.

Taken together, these results show that studying the underlying behaviors and dynamics in a worm population requires large statistics and long recordings. Depending on the desired data, both long-term recordings and short-term high-throughput measurements are accessible with PharaGlow.

3.1.6 Limitations and requirements

3.1.6.1 Variations in the signal-to-noise ratio

Using a combination of low-magnification fluorescence imaging and dedicated analysis software, we show that it is possible to perform high-throughput, automated pumping detection of worms crawling on standard culture plates. There are some limitations to the method that are due to the reliance on a fluorescent indicator in the pharyngeal muscle and the handling of the large datasets that are generated. We find that uneven plates or improper focus leads to low signal-to-noise ratios. With careful focusing, imaging the center of evenly poured plates and using our custom peak detection method that is adaptive to the image quality, these pitfalls can be mitigated. Additionally, once at focus, small variations of the animal height do not affect the result, as low-magnification imaging results in a large depth of field.

To maximize the field of view, we have chosen the smallest spatial resolution at which we could reliably detect pumping in wild-type adults. To ensure detection in smaller animals, increasing the magnification in these cases is recommended, as we did to detect pumping in larvae.

3.1.6.2 Effects of light exposure on locomotion and feeding behaviors

C. elegans are known to sense and react to light by initiating reversals and suppressing pumping. These reactions occur more frequently at short wavelengths and high power densities (Bhatla & Horvitz, 2015; Bhatla et al., 2015; Ward et al., 2008). To determine if our imaging conditions affected behavior, we measured the light intensity and the leaving rates of animals during imaging. We used excitation light centered at 500 nm, and measured an effective intensity of only 0.24 mW/mm2 in the field-of-view, 54 times lower than the reported intensity that induces pumping inhibition or spitting. We observed 5–25 % of animals leaving the field-of-view during recordings, indicating a mild avoidance reaction which depends on the developmental stage (**Fig.** 3.10).).

To control for photo-toxic effects, we split our developmental cohort into two groups. One group of animals was imaged consecutively at each larval stage (multiple exposures), the other group was left to grow under the same conditions, but only ever imaged once (single

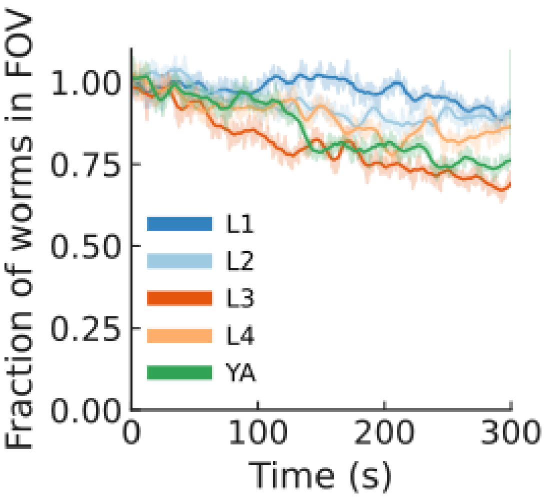

Figure 3.10: Only a mild leaving was induced by light .Mean number of animals in the field of view during the recording. Shaded: average across plates (N = 6 plates per condition), line: smoothed (averaging window = 10 s).

exposure). We find that during all larval stages, the behavioral results of the two groups are similar, but not in young adults (Figure3.11). For the young adult cohort, the animals that were repeatedly imaged show a higher velocity compared to the single-exposure group, as well as differences in all other behavioral metrics we report. We speculate that this could be due to differences in drying of the plates during repeated imaging, or a possible light-induced chronic effect.

Over longer time scales, exposure to light can reduce the worms' lifespan (De Magalhaes Filho et al., 2018). To test for chronic photo-toxic effects, we tested the viability of worms after long exposure to 500 nm light. We continuously illuminated 30 young adult GRU101 worms for five hours using the same illumination intensity as our PharaGlow assay (0.24 mW/mm2 at the focal plane). We employed a copper frame to prevent the animals from escaping the illuminated area. A plate not exposed to the 500 nm light was placed on the same bench close to the microscope as our negative control. After five hours, the copper frame was removed and animals were scored for viability both immediately and after overnight recovery in a 20 ℃ incubator. All animals were viable and able to move upon gentle tapping on the plates immediately after illumination. Further checking after overnight recovery confirmed their continued viability. This suggests that exposure to this light level does not cause observable photo-toxic effects.

To further assess the impact of the excitation light on behavior, we measured on-food pumping in adult animals expressing the red fluorophore mCherry compared to the strain expressing YFP, which is used throughout the paper. If the impact of the wavelength is non-negligible, the red fluorophore mCherry (excitation centered at 587 nm) should result

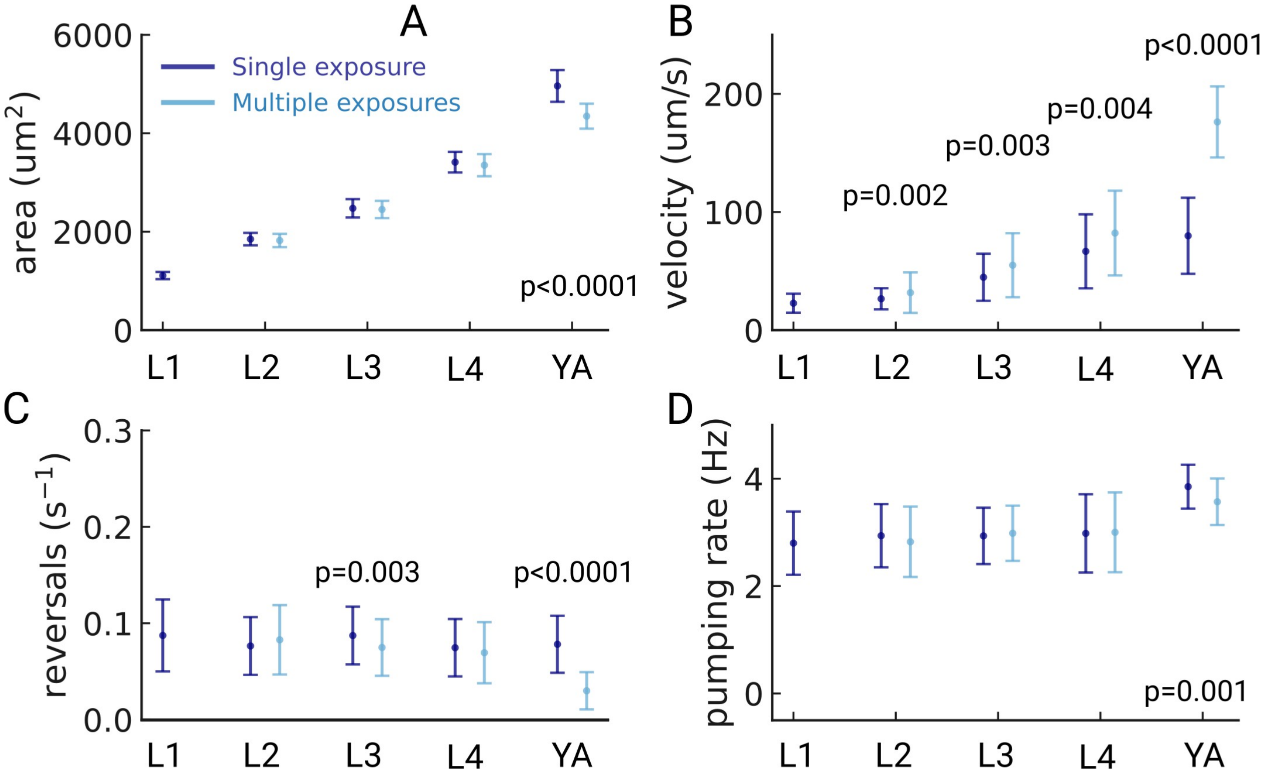

Figure 3.11: Possible light-induced behavioral changes. (A) Pharyngeal area of the detected animals for the group of animals that were imaged once (dark blue) or multiple times (light blue). (B) velocity, (C) reversal rate and (D) pumping rate for the same two cohorts. p-values are reported at the bottom for all p-values < 0.01. (Welch's unequal variance two-tailed t-test). The sample size of each group was L1 (191/144), L2 (132/153), L3 (87/114), L4 (112/59), and YA (38/142) for $N_{multiple}$ and N_{Single} respectively. Significant p-values are explicitly reported in the figure, all other pairwise comparisons were not significant (Welch's unequal variance two-tailed t-test).

in fewer reversals or accelerations compared to YFP, as these responses are wave-length dependent (Bhatla & Horvitz, 2015; Bhatla et al., 2015; Ward et al., 2008). As expected, we find an increase in the velocity for the green light exposed animals (**Fig.** 3.12.A). However, we find that pumping rates between the two populations are not significantly different ((**Fig.** 3.12).B), suggesting that these light intensities do not affect pumping behavior. The differential effects of excitation light on behavior should be taken into account when investigating the coupling between locomotor and feeding behaviors.

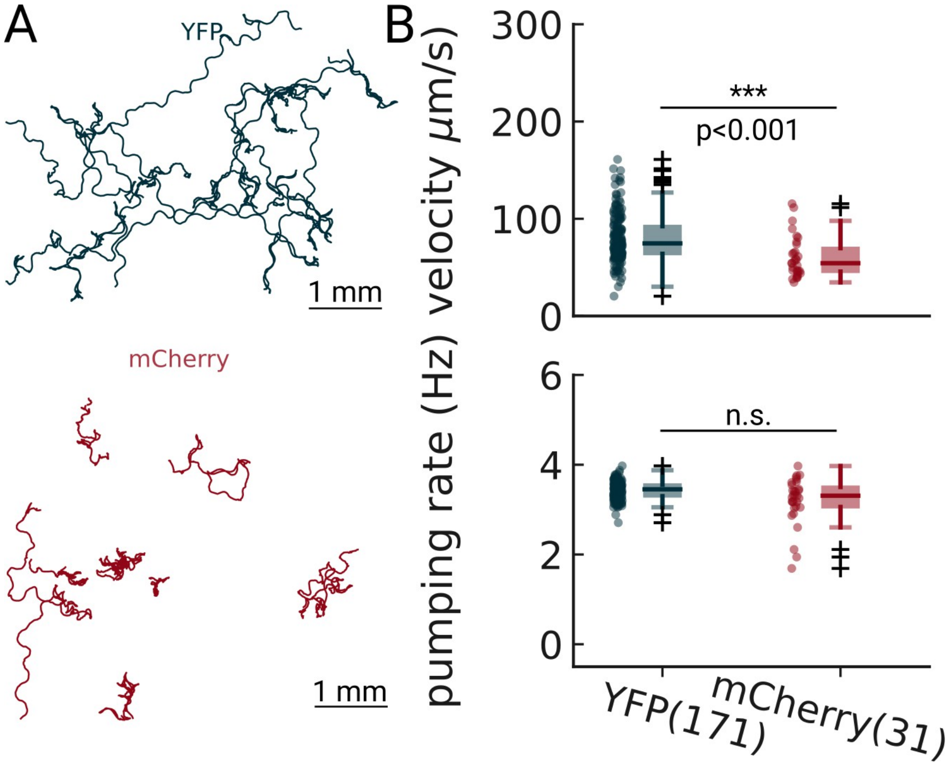

Figure 3.12: Pumping detection is robust at two different excitation wavelengths. Animals expressing either YFP (blue) or mCherry (red) were imaged on food and analyzed using PharaGlow. (A) Example trajectories. (B) The pumping rates are not significantly different but the velocity is slightly higher in animals exposed to blue (YFP) versus green (mCherry) excitation light (Welch's unequal variance two-tailed t-test).

3.1.6.3 Collision detection and effective number of independent animals in the field-of-view

PharaGlow detects all fluorescent objects in the field of view. The experimenter should choose a minimal and maximal size to allow only tracking objects that are single animals. If animals touch, an object that is larger than the maximally allowed size (maxSize) will be detected. In this case, the program automatically re-segments the region and attempts to separate the large object into multiple smaller objects using repeated filtering and thresholding. If this process is successful and two or more objects of the correct size can be separated, the program will continue tracking these animals. This approach is successful when animals touch, but do not overlap. We are unable to resolve crossings where animals are physically overlapping.

To determine the effect of collisions on tracking, we determine the number of detected objects in the field-of-view and compare it to the number of tracks obtained. Analysis of the track duration shows that average tracks are two min, and this duration depends on the velocity (Figure3.13.A). We find that these two measures correlate well, supporting the view that animal tracks are not frequently broken into small tracklets (**Fig.** 3.13.B).

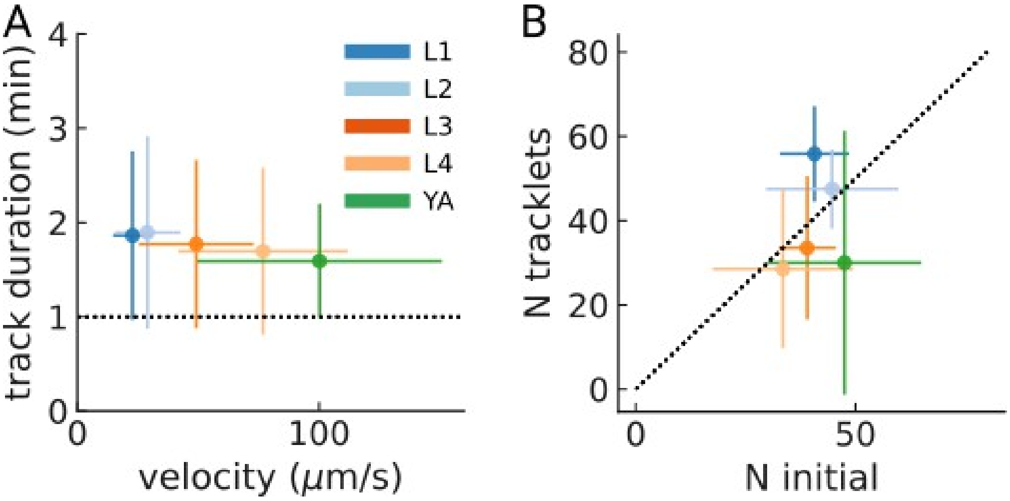

Figure 3.13: Stable tracking has shown by correlated track duration and number of tracked animals. (A) Mean track duration per experiment across larval stages (N = 6 plates per larval stage). Error bars denote STD between plates. (B) Correlation between the number of animals initially in the field of view, and the resulting number of tracks (N = 6 plates per larval stage). The dashed line denotes unity. Error bars denote STD between plates.

3.1.6.4 Transgenic lines

As it is necessary for our approach to label the pharynx, mutant characterization with our tool would require crossing all possible mutants with a fluorescent reporter strain, and albeit labor intensive this is nonetheless still a standard genetic practice when a reporter is used. While most experiments in this paper were performed with a homozygous, integrated reporter background (*gnaIs1*), we have also used extra-chromosomal arrays with success (**Fig.** 3.12), which allows the use of animals that have a *myo-2* reporter as a co-injection marker, for example. In addition, since our tool relies on the detection of fluorescent protein, siblings losing the transgene on the plate will not interfere with the analysis.

3.1.6.5 Computational cost and scaling

The final requirement is related to data management and handling. While the hardware requirements are restricted to equipment commonly available in many laboratories (a fluorescence dissecting microscope or a epifluorescence microscope and a Megapixel camera are needed), the data rate of the large area scan cameras is > 6 GB/min. On a 4-core laptop, the expected analysis time is approximately 8 hr for 150 worm-min of data. While the analysis can be run on a laptop or desktop computer, runtime is much improved when using a computing cluster.

We benchmarked the performance and scaling of the software using perfplot. Appendix 1—table 1 details the pure computation time as run on a 1000 frame demo recording (available for download at the data repository). We find that parallelization improves performance for the object detection for up to 8 workers, and continues improving for > 16 workers in the segmentation step. In our implementation, this option is already provided based on the python package multiprocessing. As the different steps depend on the details of the imaging, we have decided to report processing time per step.

1. Object detection The object detection step uses a full frame and does masking and object detection for each individual object. For this case, computational cost scales with the number of frames and can be easily parallelized to enable a faster speed. The average single-core computation time per frame is 300 ms, which includes I/O, as we employ lazy data loading, which allows analyses of data that are much larger than the RAM available. Of note, this step can be omitted if our acquisition software is used (see Methods) as single worms are segmented already during acquisition.

2. Tracking and trajectory interpolation The tracking step is based on trackpy and here the scaling depends on the search range (how far can an object move between frames) and the memory (how many subsequent frames can an object be unobserved). Typically, this step is much faster than the other two as it does not handle large I/O or image processing.

3. Segmentation, centerline detection, straightening, and pump detection In this step, the previously detected images of detected pharynx are further processed. The total compute time here depends on the product between the number of objects and the number of recording frames. We therefore provide a per-object assessment of the processing time.

In summary. We have developed a non-invasive optical method to automatically measure feeding and locomotion in freely moving *C. elegans*. We have shown its applicability in a range of standard assays from short recording in populations that can capture modulation by internal states (starved vs well-fed) or development stages (larvae vs adults) to more than one hour long recording in partially-restrained animals (mating).

3.2 Touch induces an intensity-dependent escape and feeding responses

To determine how touch modulates locomotion and feeding, we combined our new method for measuring pumping with a customized mechanical stimulation device. For providing touch stimuli, we exposed animals with YFP-labeled pharynx (Strain GRU101 strain in List of Transgenic Lines) to a 630 Hz buzz for 1 s at different intensities using a customized buzzing device. In short, a piezo buzzer was clamped to the animals housing plate, generating a nanoscale agar displacement resulting in a non-localized substrate vibrations, faithfully replicating both the temporal waveform and amplitude of the applied electrical signal (Sugi et al., 2016). 630 Hz buzz is an optimal frequency for triggering both an escape response (Sugi et al., 2016) and a rise of calcium in the escape circuit neuron AVA (Sugi et al., 2018).

3.2.1 Variable basal pumping rates reveal feeding states

Animals had free access to bacterial food during the measurement. In presence of food, *C. elegans* displays a dwelling behavior characterized by a high pumping rate between 4 Hz and a low speed between 50 µm/s (Gray et al., 2005; Wakabayashi et al., 2004). In accordance with our previous results (**Section** 3.1 ; (Bonnard et al., 2022)), we observed a multi-modal basal pumping rate distribution, (**Fig.** 3.14.A). This distribution was best fit by a 3-component Gaussian mixture model, which allowed us to identify three distinct basal pumping states: a non-pumping state (<= 1 Hz, 0.6 Hz ±0.4STD, 20 %) , a slow-pumping state (1-2.6 Hz, 1.9 ±0.4 Hz STD, 41 %), and a fast-pumping state (> = 2.6 Hz, 3.3 ±0.4 Hz STD, 39 %). In contrast, the basal speed was homogeneous across the population with an average of 70 ±54 um/s STD (**Fig.** 3.14.B).

Pumping pauses in presence of food has been reported (Scholz et al., 2016, 2017). However those pauses are short (600 ms) and we observed a pumping rate variation at larger timescale (10 s windows for baseline calculation) suggesting a state-dependency rather a local dynamic adaptation. We found that the non-pumping category included cases where the fluorescent signal was not stable enough for proper pump detection, which were consecutively excluded. For the low-pumping category, low pumping rate is more likely to result from satiety quiescence (Davis et al., 2018; Gallagher et al., 2013; You et al., 2008) or possibly from residual effect of mechanical stress from animal exposed multiple times to the stimulus, despite a 3 min long inter-stimulus interval for recovery. We therefore selected only animals engaged in high pumping mode before the stimulus onset to investigate how touch modulates feeding.

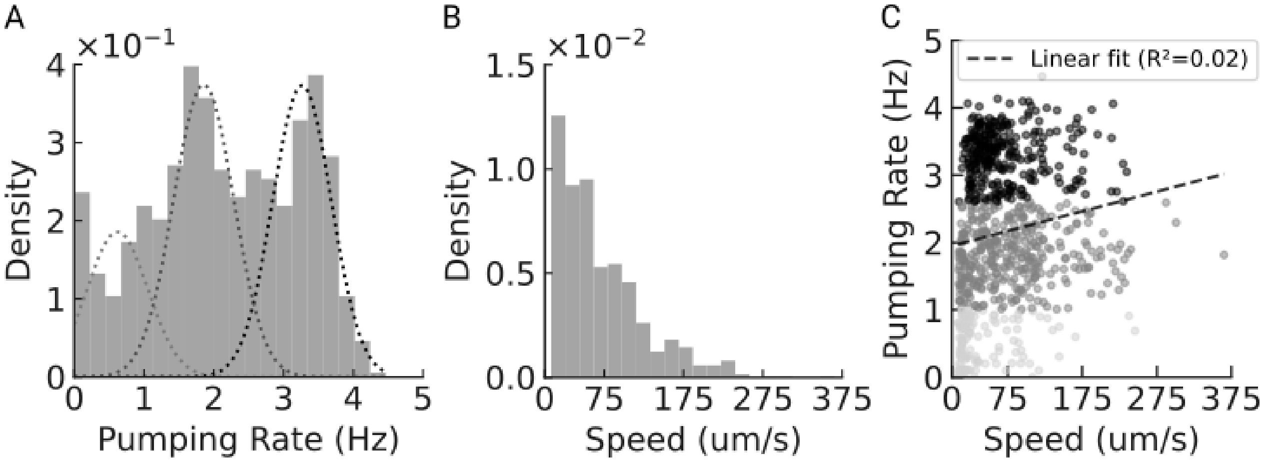

Figure 3.14: Animals exhibit different feeding states prior to stimulus exposure. (A) The distribution of basal pumping rates, calculated as the time-averaged rate over 10 s before stimulus across 777 tracks, fit by a three Gaussian mixture model. This model identifies three distinct modes: non-pumping (< 1 Hz), low pumping (1 to 2.6 Hz), and high pumping (> = 2.6 Hz). (B) The distribution of basal speeds for the same population is more homogeneous with an average of 70 ±54 um/s STD. (C) Correlation between basal speed and pumping rate ($R^2 =$ 0.02). Light gray for non-pumping, gray for low-pumping and dark gray for high-pumping modes

3.2.2 Touch induces a speed increase and a pumping inhibition

We found that substrate vibrations trigger both an escape response and a feeding inhibition (**Fig.** 3.15). The escape response is characterized by an immediate speed increase peaking within the first 5 s post-stimulus up to 200 um/s, followed by a sustained, albeit reduced, high speed lasting several tens of seconds. This pattern is consistent across individuals with 86 % of the animals responding, showing a significant increase from baseline 10 s after the stimulus onset (146.31 %, p-value < 0.001, Wilcoxon, **Fig.** 3.15.A-B). The feeding response is more heterogeneous as shown by the variable individual pumping rates in the heatmap in **Fig.** 3.15.C. Nevertheless the population average shows a significant reduction within 10 s post-stimulus onset compared to baseline (-17.75 %, p-value < 0.001, Wilcoxon test, **Fig.** 3.15.D) and 57 % responders. The dynamic and amplitude of the pumping inhibition aligned with previously reported pumping inhibition following 1 kHz-substrate vibrations (30 % in McClanahan et al., 2020).

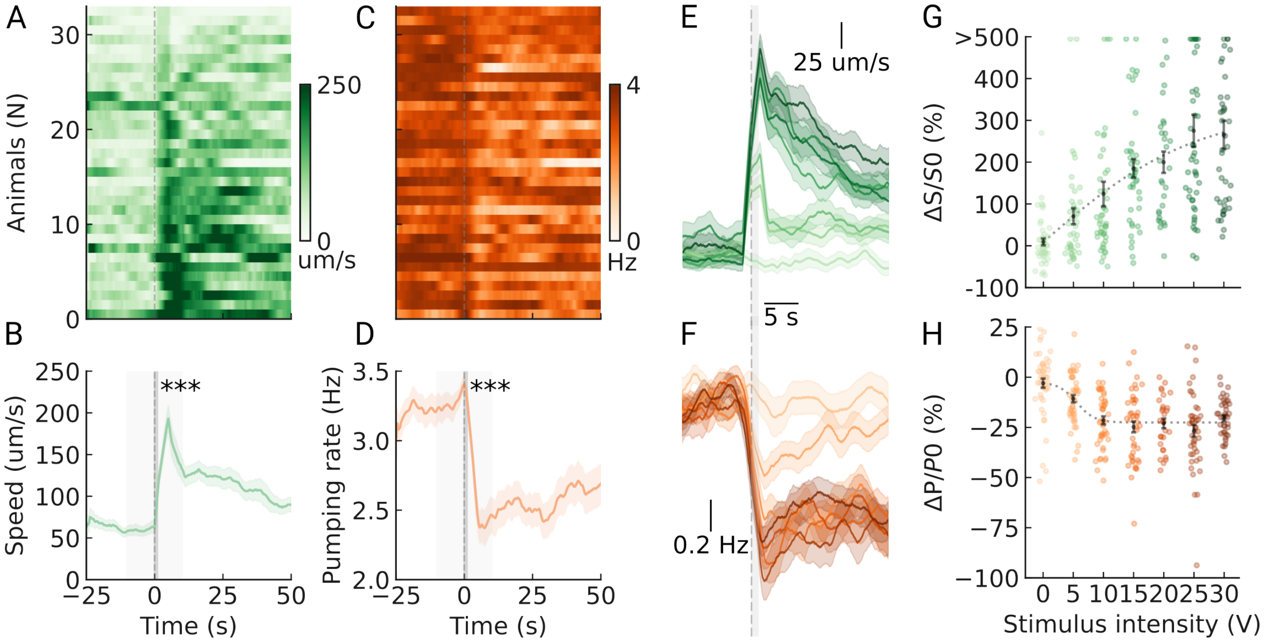

Figure 3.15: Escape speed increases with stimulus intensity while pumping inhibition saturates. (A-D) Speed and pumping rate simultaneously measured in wild-type animals populations are aligned to a 15 V buzz onset. Individual speed (A) and pumping rate (C) are ordered by ascending speed response. Below, the corresponding population averages ±SEM show a significant increase in speed (B) and decrease in pumping rate (D) 10 s after stimulus onset compared to 10 s before as indicated by gray zones (p-value < 0.001, Wilcoxon test). (E-F) Population averaged speed (E) and pumping rate (F) responses to different stimulus intensities, and (G-H) the corresponding response amplitude change compared to baseline, with error bars representing population averages ± SEM fitted by a logistic model ($R^2 = 0.98$ for speed (G) and 0.94 for pumping (H)). Note speed change is clipped to 500 % since due to a few values reaching up to 1000 %. Number of animals per stimulus intensity: 48 for 0 V: 48, 45 for 5 , 46 for 10 V, 42 for 15 V, 29 for 20 V, 43 for 25 V, 39 for 30 V. Stimulus onset is shown as a dark gray dashed line, and stimulus duration as a dark gray zone.

3.2.3 Escape speed increases while pumping inhibition saturates with stimulus intensity

To infer the transfer function of the bottleneck, we exposed the animals to various stimulus intensities, ranging from 0 to 30 V, and measured the psychometric curves for both speed and pumping responses. The amplitude of the speed response increases monotonically with stimulus intensity (**Fig.** 3.15.G), while the amplitude of the pumping response reaches a plateau around 20 % inhibition already at 10 V (**Fig.** 3.15.H). Similarly the number of responders stabilized between 56 and 72 % from 10 V for pumping but reach up to 90 % for speed (**Fig.** 3.16). However the speed response population average is not significantly different above 15 V (p-value > 0.05, Mann-Whitney test), which suggests a saturation in the speed response as well but occurring at higher intensity than for pumping.

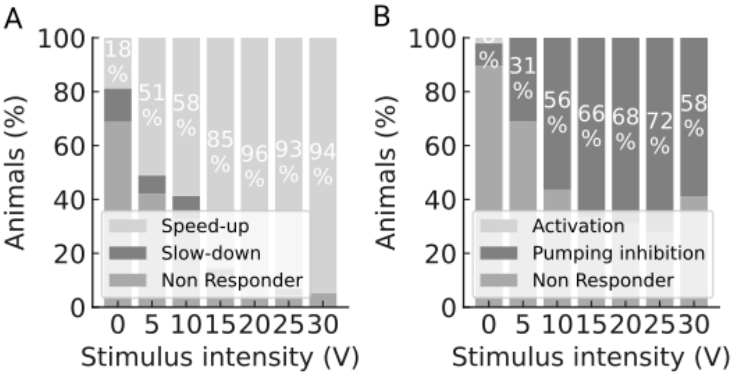

Figure 3.16: Animals are robustly engaged in escape speed-up, but only partially recruited for feeding inhibition. The percentage of animals showing escape responses increases with stimulus intensity, reaching a plateau near 90% at higher intensities. Colors indicate response types: light gray for speed increase, medium gray for no response, and dark gray for speed decrease. (B) The percentage of animals showing feeding responses stabilizes between 50-70% above 10 V. Colors indicate: light gray for pumping rate increase, medium gray for no response, and dark gray for pumping rate decrease.

3.2.4 No correlation between pumping and feeding responses

We wondered if the escape and feeding behaviors might be coupled. We found no correlation between the basal pumping and basal speed over the whole population ($R^2 = 0.02$) (**Fig.** 3.14.C) or in the high-pumping population ($R^2 = 2e^{-4}$). Those results suggest that the two behaviors are uncoupled in the ground state in animals engaged in sustained feeding. These two behaviors might be synchronized upon a salient stimulation. We therefore examined how the speed and pumping responses to touch in the high-pumping population vary together. We found no correlation between the speed response and the pumping inhibition ($R^2 = 0.07$; **Fig.** 3.17). Those results suggest that locomotion and feeding behaviors seem to act independently from each other, if the occurrence of a salient environmental event might coupled them remain unclear, at least for the acute responses—within the first 10 s post stimulation. Alternatively, non-linear relationships might play a role which has not been captured by our analysis.

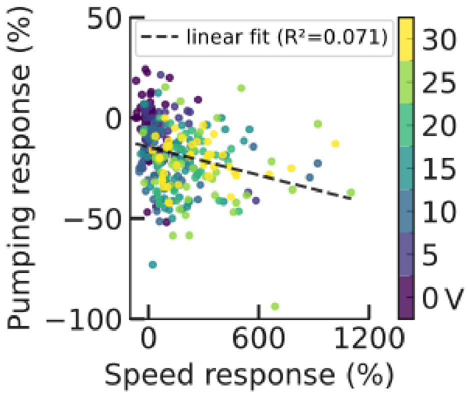

Figure 3.17: No correlation between speed and pumping responses. Data shown in 3.15 are combined across all stimulus intensities (V) and fitted with a regression model ($R^2 = 0.071$). Negative values in pumping responses correspond to a pumping rate decrease, and positive values in speed responses correspond to a speed-up.

In summary, we have shown that substrate vibrations induce both a pumping inhibition and an escape speed increases at the population level. Feeding trends to be binary tuned by the stimulus intensity (weak vs strong) whereas the escape is more graded. Locomotion and feeding circuits might process differently the incoming touch signal or touch signal might have been differently pre-processed. In the latest case, the bottleneck layer between the two circuits may filter touch signal based on intensity. A first step, to verify this hypothesis is to determine if the touch signal flows through the bottleneck to reach the pharynx.

3.3 The touch signal is detected by the touch receptor neurons and flows through the RIP-I1 neural bottleneck to inhibit feeding

In order to determine through which neuronal layers the touch signal flows in the touch-feeding system, we genetically ablated the candidates neurons for the input (TRNs) and bottleneck layers (RIP and I1).

3.3.1 Touch receptor neurons are required to mediate both feeding and escape responses to touch

We generated touch-insensitive mutants with a YFP-labeled pharynx by crossing GRU101 animals (List of Transgenic Lines) with available lines expressing mutations in the *mec-4* gene. This gene codes for the mechanotransducer subunit channel MEC-4 specific to TRNs. The first line labelled "TRN" (strain INF206 in List of Transgenic Lines) has a gain-of-function mutation (*mec-4(e1611)*) leading to the degeneration of TRNs (Brown et al., 2007; Hong et al., 2000). The second line termed "MEC4" (strain INF22 in List of Transgenic Lines) is a loss-of-function of the mechanoreceptor (*mec-4(u253*) but TRNs remain intact (Arnadottir et al., 2011; Hong et al., 2000; Huang & Chalfie, 1994). Single animals were exposed to repeated buzz at 15 V, an intensity which elicits both an escape and feeding suppression (**Fig.** 3.15). In mutants lacking TRNs ('TRN') or functional mechanotransducer channels ('MEC4'), the speed and pumping rate remain unchanged following the stimulus onset (3.19.A). Compared to animals with YFP pharynx ('YFP'), the speed responses are significantly lower ($p < 0.001$, Mann-Whitney U-test) varying around 0 (no response) and the pumping responses are significantly higher indicating a release of inhibition ($p < 0.001$ for 'TRN', $p < 0.01$ for 'MEC4', Mann-Whitney U-test) (**Fig.** 3.19.B). The completely abolished pumping and speed responses in the touch insensitive mutants suggest that TRNs are the input layer in the touch-feeding circuit.

3.3.2 Bottleneck neurons are required to mediate the feeding response but not the escape response to touch

Next we tested the requirement of the bottleneck neurons by genetically ablating the RIP and I1 neurons using a GAL/UAS strategy (Duffy, 2002; Wang et al., 2017). To achieve cell-specific ablation, we created cGAL lines specific to RIP and I1 that we crossed to available UAS effector lines, one expressing GFP and the other ICE (Cerretti et al., 1992; Thornberry et al., 1992). In *C. elegans*, neurons expressing ICE undergo cell death in early development (Zheng et al., 1999). We confirmed the loss of RIP or I1 neurons by the lack of GFP marker using confocal microscopy (**Fig.** 3.18). We estimated an ablation efficiency of approximately 90 % by investigating how many animals of the populations showed remaining GFP expression. These results validate our cGAL/UAS approach which enable precise genetic targeting of the RIP and I1 neurons.

In the hypothesis that the touch signal flows through the bottleneck to reach the pharynx, we expect no pumping response in animals where the bottleneck to the pharynx is disrupted, but an intact escape response-the escape circuit is upstream of the bottleneck like

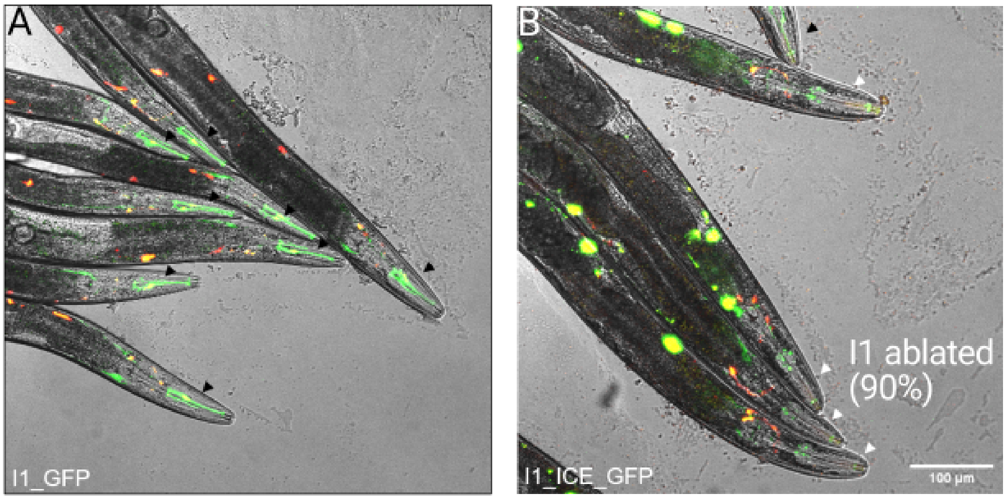

Figure 3.18: Confocal microscopy validation of genetic ablation of I1 neurons. Confocal images of immobilized animals expressing in the I1 neurons (A) GFP only (strain INF127) or (B) GFP and ICE (strain INF411) using the cGAL-UAS system. Color-code: GFP in green, co-injection markers in red (coleomocytes and AIY neurons). ICE leads to disappearance of GFP-labelled I1 neurons in 9 out of 10 animals. Scale bar: 100 µm.

the touch receptor neurons.

Consistent with this hypothesis, we observed no change in pumping rate following the stimulus onset in mutants lacking the RIP or I1 neurons. Expectedly, the speed increases upon stimulation (**Fig.** 3.19.A). The pumping responses over the population in RIP- and I1-ablated animals vary around 0 which means no response 3.19.B). The pumping response in I1-ablated animals are significantly lower than in the I1-driver animals ($p < 0.001$, Mann-Whitney U-test). However the pumping response in RIP-ablated animals is not significantly different than in RIP-driver animals ($p > 0.05$, Mann-Whitney U-test). This discrepancy is more likely to reflect a milder pumping inhibition in RIP-driver animals compared to the reference animals with YFP labeled-pharynx only.

In contrast, the population speed response in both RIP- and I1-ablated animals are positive which means an increase of speed following the stimulus onset. This increase is not different than in the driver animals ($p > 0.05$, Mann-Whitney U-test). However we observed a weaker speed responses in those animals than in the reference animals, confirming the impact of the driver transgene itself on the observed behaviors.

Taken together, these results suggest that the RIP and I1 bottleneck neurons are necessary to mediate the pumping inhibition by substrate vibrations. The complete abolition of the response in animals lacking these neurons indicates that the touch signal flows exclusively through this bottleneck to reach the pharynx, at least within the first 10 seconds following stimulus onset. To strengthen these findings, further backcrossing of the driver lines to the wild-type strain N2 could help to minimize background mutations and recover more robust behavioral responses, consequently providing a cleaner readout of the cell-specific manipulations. Alternatively, the use of different cell-specific promoters could be explored; however, no other promoters specific to the RIP or I1 neurons are currently available.

3.3.3 Attempt to determine the innexins forming the gap-junction coupling RIP and I1 neurons

An alternative approach for disrupting the bottleneck gateway to the pharynx is to genetically disrupt the gap-junctions coupling the RIP and I1 neurons. However the innexins forming those gap-junctions are unknown. Based on literature search and database screening (CenGen), we estimated that the three most likely partners would be *inx-4* / *unc-9*, *inx-4* / *unc-9* and *inx-4* / *unc-9*. We created mutants where the UNC-9 innexin in the I1 neurons is disrupted by expressing a dominant negative allele of *unc-1* gene under the I1 promoter *lgc8p*, *unc-1* encodes a stomatin-like integral membrane protein that co-localizes with UNC-9 proteins and modulates the gating of UNC-9 gap junctions in muscles and neurons which is disrupted in dominant negative form of UNC-1 (B. Chen et al., 2007; Jang et al., 2017). In gap-junction mutants, the pumping response seems to be less sustained than in YFP control (**Fig.** 3.19.A) with a significant reduction in amplitude as calculated within the 10 s post stimulus ($p < 0.01$, (**Fig.** 3.19.C). As expected, touch induces a speed increase similar than for YFP pharynx control and even a slightly higher than in I1-driver line ($p < 0 .05$, Mann-Whitney U-test). Those results suggest that the innexin UNC-9 in the I1 neurons may be part of the gap-junctions with the RIP neurons. Other innexin isoforms might be on the same side, forming heteromeric connections or the UNC-9 might not have been fully disrupted. Further experiments are required to identify the innexins such as co-expression of a fluorescent reporter of UNC-9 or other candidate innexins expression in the RIP and I1 neurons. Their requirement can be further tested using RNA interference. Identifying the gap-junctions between the RIP and I1 neurons will allow us to get insight about the mechanism underlying the touch signal transformation in the bottleneck.

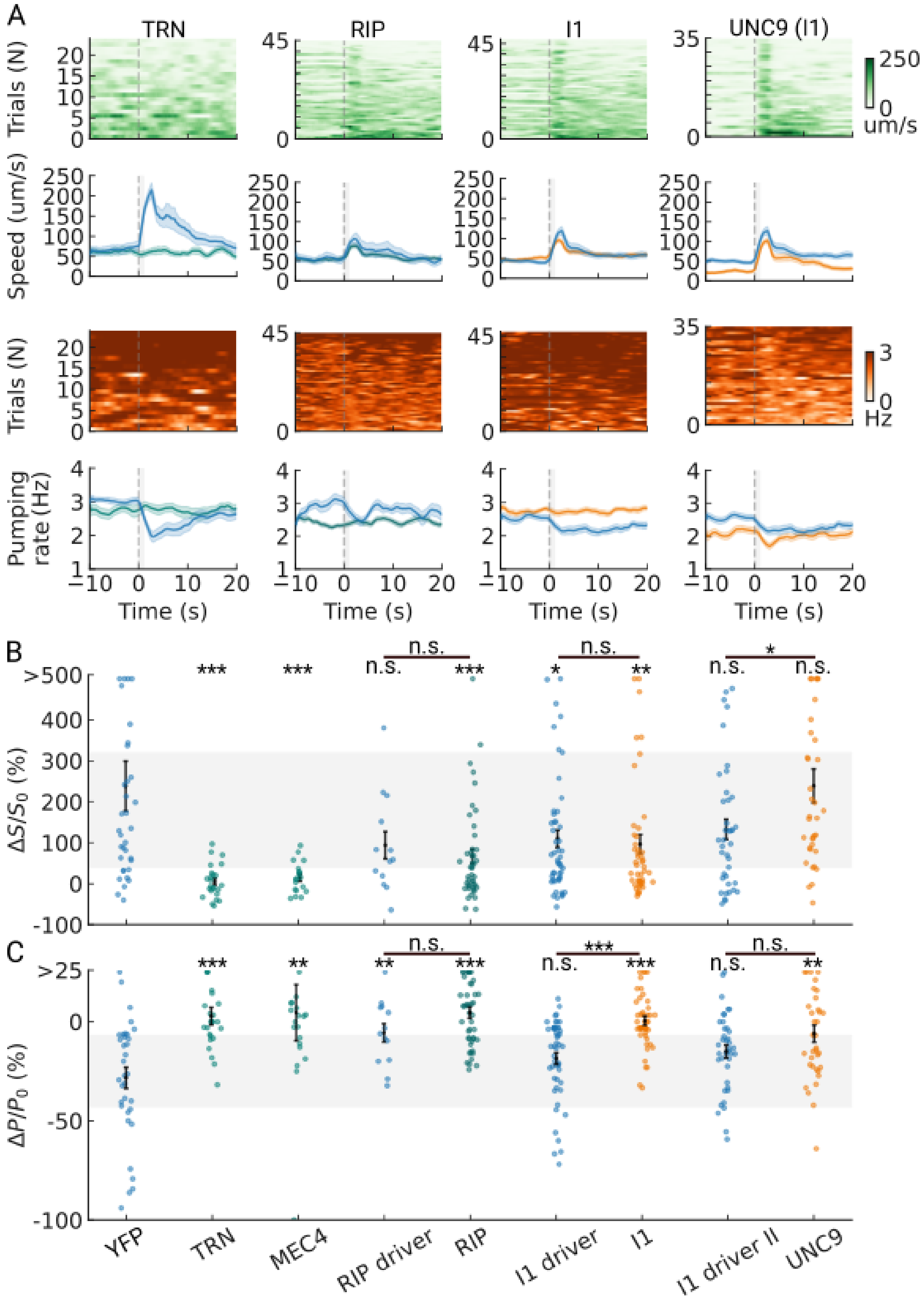

Figure 3.19: Touch-induced speed and pumping responses required TRNs whereas only pumping response required the RIP-I1 bottleneck. (Caption continued on the next page)

Figure 3.19 (continued). Touch-induced speed and pumping responses required TRNs whereas only pumping response required the RIP-I1 bottleneck. (A) Speed and pumping rate dynamics simultaneously measured and aligned to 15 V) buzz onset for individual trials over multiple animals. Below the population average ± SEM. From left to right: 'TRN' for touch-deficient mutants lacking TRNs (strain INF206) in green compared to YFP pharynx animals in blue ('YFP', strain GRU101). 'RIP': bottleneck mutants lacking RIP neurons (strain INF529) in green compared to RIP-driver animals in blue ('RIP driver', strain INF530) in blue. 'I1': bottleneck mutants lacking I1 neurons (strain INF417) in orange compared to I1-driver animals in blue ('I1 driver', strain INF407) in blue.'UNC9 (I1)': gap-junction mutants with impaired innexin UNC-9 in the I1 neurons (strain INF557) in orange compared to I1-driver animals in blue ('I1 driver II', strain INF556) in blue. Individuals (B) speed responses amplitude clipped to 500 % and (C) pumping responses amplitude to 25 % with population averages ± SEM in error bar. Mann-Whitney U-test run against the YFP control per default, otherwise against the drivers as indicated by the bar."MEC4": touch-deficient mutants lacking the mechanotransducer channel MEC-4 in the TRNs (Strain INF22). For comparison, grey zone show the STD of the responses in YFP pharynx animals at 15 V shown in **Fig.** 3.15.G-H.

In summary, using cell-specific genetic ablations, we mapped the core pathway of the touch-feeding circuit: the touch signal are detected in the TRNs and flows through the RIP and I1 bottleneck neurons to inhibit feeding.

3.4 The touch receptor neurons encode linearly the stimulus intensity

Psychometric curves revealed that the touch circuit processes stimulus intensity differently for two behaviors: locomotion (graded escape speed increase) and feeding (ON/OFF-like pumping inhibition) (**Section** 3.2. We hypothesized the bottleneck layer acts as an intensity filter, converting a graded input into a step-like output to gate feeding. To test this hypothesis, we enabled single neuron calcium imaging in the input and bottleneck layers.

3.4.1 GCaMP7f doesn't report touch receptor neurons responses to low stimulus intensities

Ca^{2+} has been shown to amplify the Na^{+} dependent depolarization induced by mechanical stimulation in the TRNs and be a reliable indicator of their responses(Goodman 2019).

We designed a plasmid containing both GCaMP7f, as it was the most recent version available in *C. elegans*, and a red fluorescent protein mKate2 insensitive to calcium for ratiometric measurement using the *mec-17* promoter to target all six TRNs. We verified the expression using confocal microscopy (**Fig.** 3.20.A). While we could detect both mKate2 and GCaMP7f in all TRNs, the expression was strongest in the PLM neurons. We therefore measured PLM responses to touch in animals immobilized by levamisole, an agonist of acetylcholine receptor in body-wall muscles resulting in sustained contraction and consecutively paralyzing (Holden-Dye et al., 2013). Multiple animals could be imaged simultaneously while a piezo buzzer supplied substrate vibrations with varying amplitudes in similar condition than used for the behavioral assay in 3.2. However there is neither locomotion nor feeding in this preparation.

We observed that the activity in PLM scales linearly with stimulus amplitude (**Fig.** 3.20.B and C, see also **Fig.** 3.24 for individuals traces), consistent with electro-physiological studies (Eastwood et al., 2015; Katta et al., 2019; O'Hagan et al., 2005) and calcium imaging data obtained with GCaMP6m (Cho et al., 2017). However the calcium response was detectable from 10 V intensity whereas our behavioral data showed feeding and escape responses already from 5 V (3.15), the lowest intensity that we tested. This discrepancy between behavioral and neuronal data indicated that GCaMP7f indicator does not allow proper detection of PLM responses to the lowest stimulus intensities.

Other GECIs could allow a finer detection. jGCaMP8, derived from a prior generation (GCaMP6) through structure-guided mutagenesis, show faster kinetics, to be brighter upon binding to Ca^{2+} and more sensitive to smaller amounts of intracellular calcium (Zhang et al., 2023). While these properties have been demonstrated using recordings in the fruit fly, mouse, and neuronal cell culture, its use in *C. elegans* has not been validated yet.

3.4.2 Successful adaptation of GCaMP8f in *C. elegans*

To determine whether GCaMP8f also shows the reported improved properties as a fluorophore in *C. elegans*, we wanted to compare it with the prior generation of fluorophores in a standardized setting. GECIss are frequently compared in spiking neurons with stereotyped action potentials, which simplifies the analysis: as the underlying shape is expected to remain the same, any change in the signals read-out by imaging can be attributed to changes in the indicator properties. However, as *C. elegans* neuronal activity is characterized predominantly by graded potentials (Goodman et al., 1998), we decided to instead use the stereotypical contractions of the pharynx to test first the properties of this GECIs.

C. elegans uses its pharynx to ingest bacteria, and this muscle shows action potentials shaped by voltage-gated Ca^{2+} and K^{+} channels (Shtonda & Avery, 2005). The quasi-rhythmic action of the pharyngeal muscle was also the first behavior whose activity was visualized with a GECI in *C. elegans*, i.e., Cameleon (Kerr et al., 2000). To test the *C.*

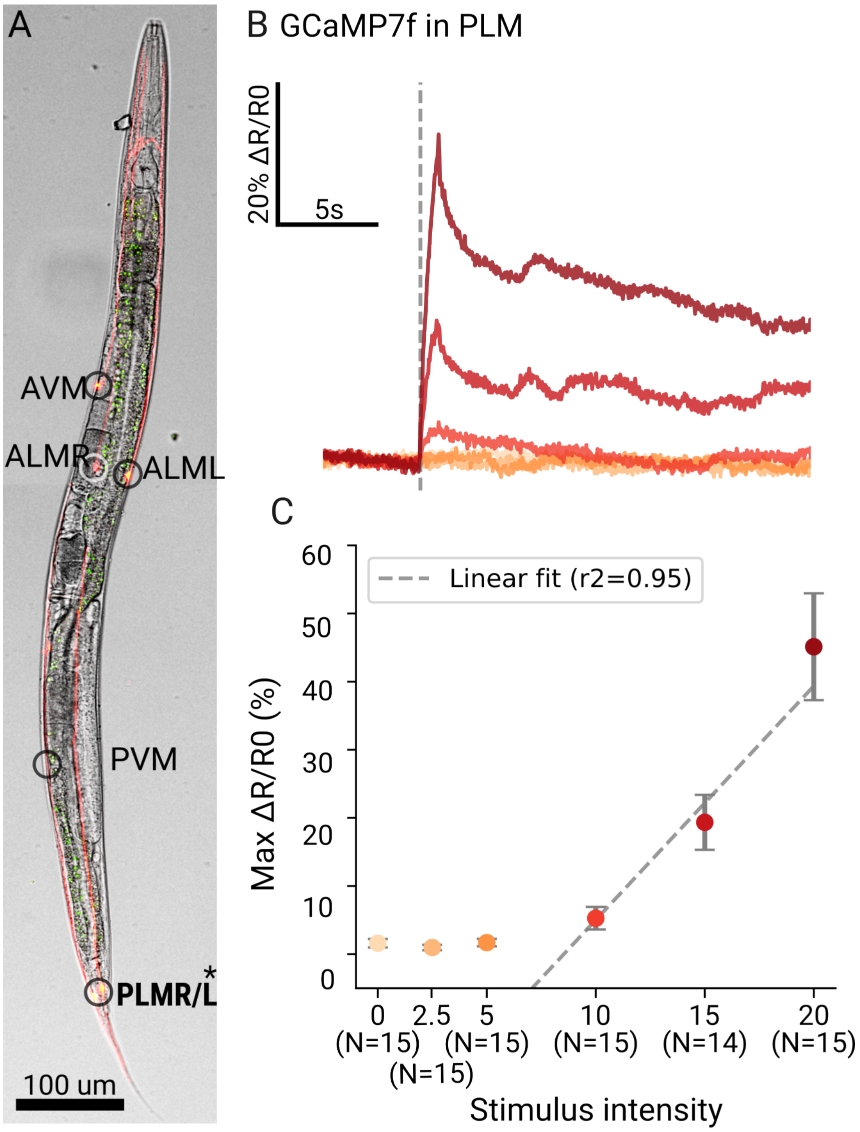

Figure 3.20: GCaMP7f fails to report low stimulus intensity responses in TRNs. (A) Confocal microscopy image showing an animal expressing GCaMP7f (green) and mKate2 (red) in TRNs. Asterisks indicate PLM neuron pair among TRNs used to extract activity. (B) Population averaged responses of PLM neurons to graded stimulus intensities using ratiometric correction. (C) Stimulus intensity–response curve. The response was fitted with a linear model based on prior observation of TRNs linearity. Bars indicate the standard error of the mean at the maximal ratio change. The stimulus intensities are color coded in oranges.

elegans optimized GCaMP8f, we used a similar approach and expressed the fluorophore in the pharyngeal muscle using the *myo-2* promoter. Based on the published sequence in Zhang et al. (2023), we generated a codon-optimized version for *C. elegans*, with 3 introns added, that were suggested to improve expression (Okkema et al., 1993). The resulting sequence was cloned into a plasmid containing the *myo-2* promoter specific to pharyngeal muscle and an *unc-54 3' UTR* (**Tab.** 2.1). We then compared the activity of GCaMP8f with the previous generation of GECI, GCaMP7f (Dana et al., 2019) (**Fig.** 3.21.A and B). By applying 5-HT, action potentials in the pharynx can be stimulated and the activity of the GECI visualized using fluorescence microscopy with limited intrinsic behavioral variability (**Fig.** 3.21.C and D). We find that as described for *Drosophila melanogaster*, mouse and in neuronal cell cultures (Zhang et al., 2023), the indicator has a larger dynamic range (**Fig.** 3.21.E and F) and shows faster kinetics compared to GCaMP7f (**Fig.** 3.21.G and H). In particular, for rapid contractions (**Fig.** 3.21.D), the slower indicator GCaMP7f is unable to return to the baseline between contractions, thus reducing the peak amplitude and potentially hindering detection of calcium transients.

Given the increased dynamic range and kinetics, we wanted to test whether these properties enable new assays at lower resolution, allowing high-throughput data collection, for example by detecting the feeding contractions of the pharynx muscle. While pumping can be detected without fluorescent labels, this requires imaging at higher magnifications and often laborious postprocessing. We previously found that expressing a non-calcium-dependent fluorophore enables detecting pumping at lower magnification and in freely moving animals (See section 3.1 and (Bonnard et al., 2022)). Using animals expressing either GCaMP7f or GCaMP8f in the pharyngeal muscle, we imaged groups of worms on a plate seeded with food. Compared to our previous work (Bonnard et al., 2022), we could detect animals labeled with GCaMP8f and GCaMP7f at even lower magnifications (0.5× instead of 1×), enabling a field of view of 1.5 cm (**Fig.** 3.22.A and B). By tracking and segmenting the signals, we could find clear, stereotyped peaks in the fluorescence signals of animals expressing GCaMP8f, but not GCaMP7f (**Fig.** 3.22. C). While the brightness of GCaMP7f was sufficient to track the animals, the peaks in GCaMP7f signals were noisy, likely due to the slower indicator speeds as seen in **Fig.** 3.21.D and the smaller dynamic range (**Fig.** 3.22.C). We therefore concluded that the pumping rates extracted from peaks in GCaMP7f were not a reliable reflection of the true pumping rate (**Fig.** 3.22.E).

One disadvantage of these indicators is their required binding of intracellular calcium. This results in sequestering some of the free calcium ions, thereby lowering their overall concentration and potentially interfering with intracellular processes. The effects of this can be observed both for GECIs that express in muscle, as well as in neurons, as strains that ex-

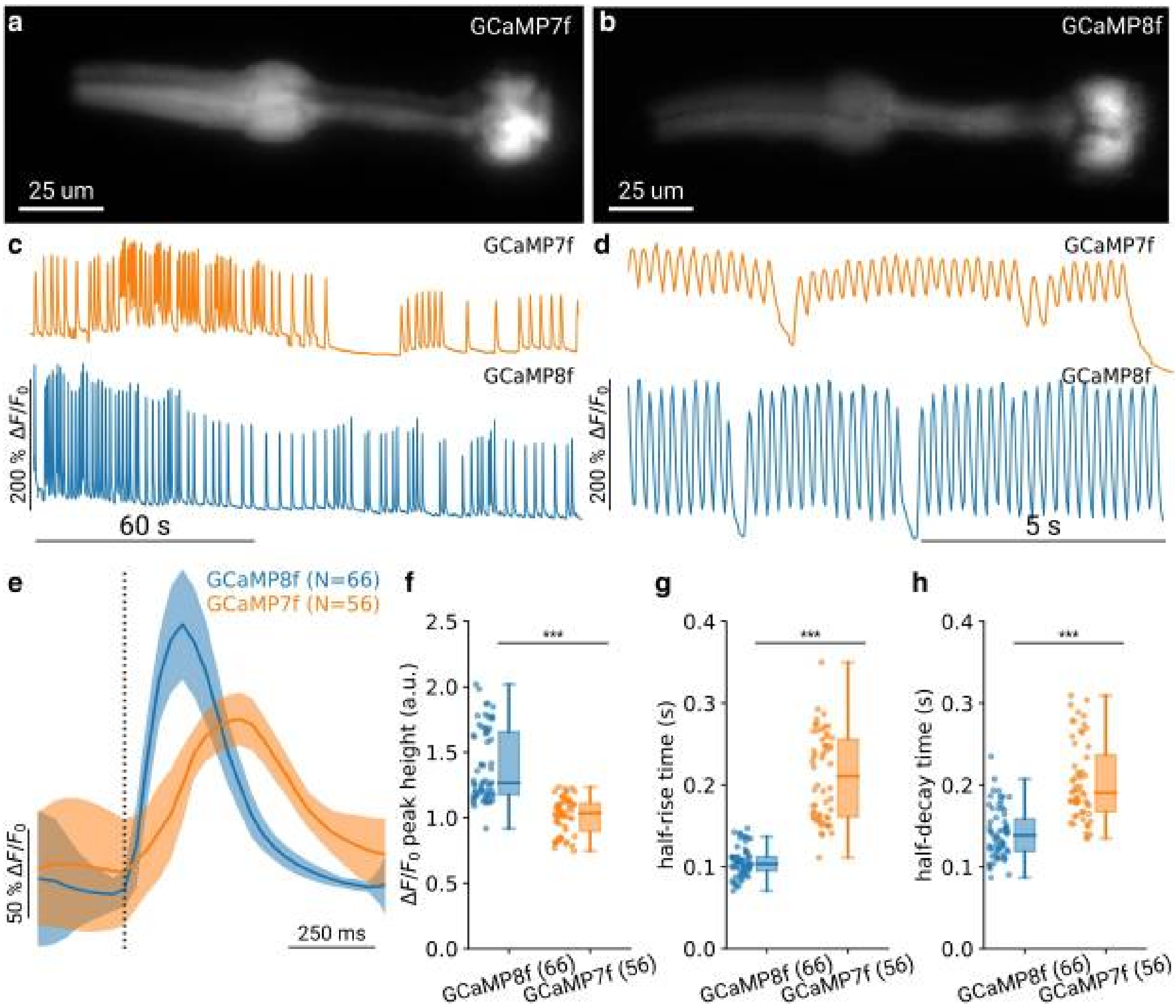

Figure 3.21: Improved detection of calcium dynamics with GCaMP8f. Images showing (A) GCaMP7f and (B) GCaMP8f expressed under the *myo-2* promoter in adult *C elegans* during pharyngeal pumping. (C) Example traces of pharyngeal muscle activity with GCaMP7f (top) and GCaMP8f (bottom) under stimulation with 10mM 5-HT for a representative animal during slower overall pumping and (D) for faster pumping animals. (E) Mean peak shape aligned to the onset for GCaMP7f and GCaMP8f. Shaded area indicates the standard deviation. Note that the increase in standard deviation before and after the peak is due to nearby peaks starting within the window of alignment and does not indicate an issue with detection. (F) Maximal peak height for GCaMP7f (N = 56) and GCaMP8f (N = 66), respectively. (G) Half-rise time for each peak, as estimated from the first moment the traces reached 0.5*maximal height. (H) Half-decay time for each peak, as estimated from the first moment the traces decayed to 0.5*maximal height. *** indicates P<0.001. Significance was assessed using Welch's unequal variance t test.

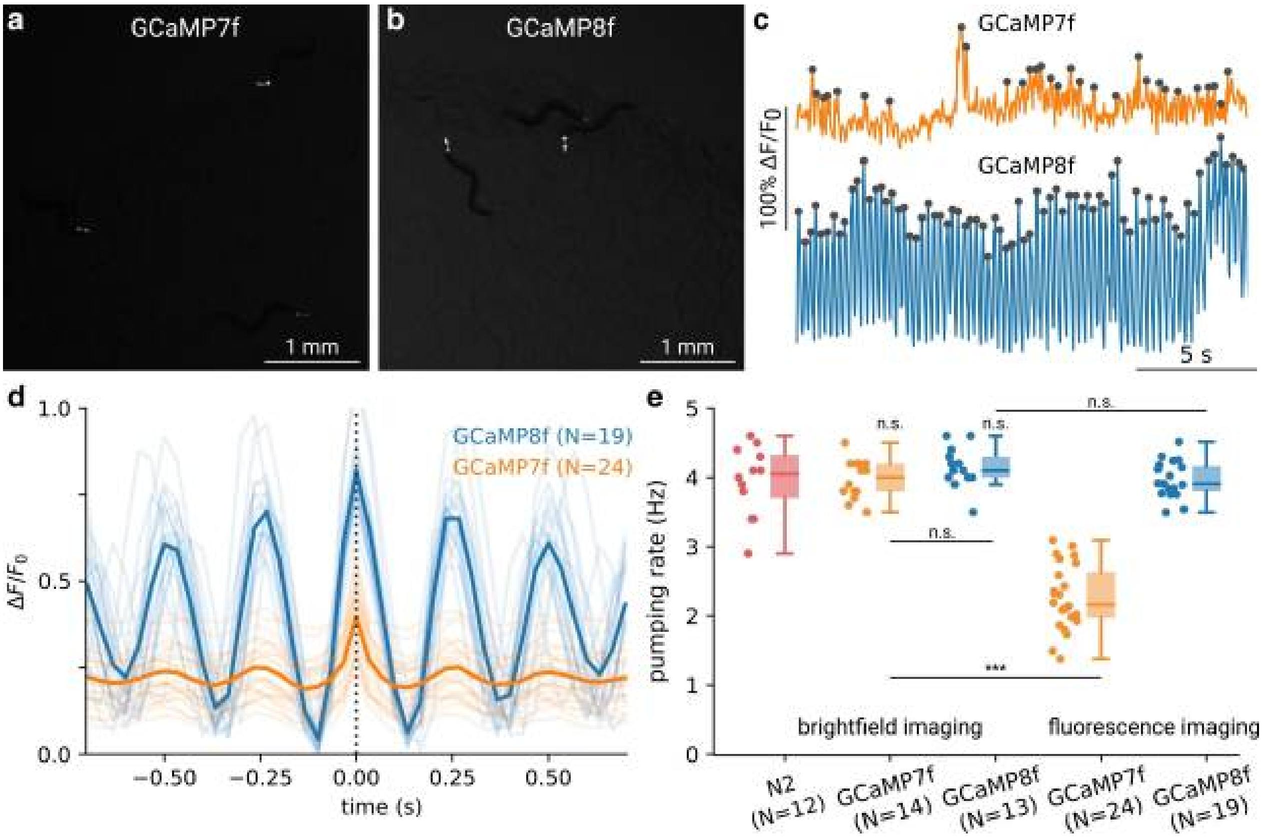

Figure 3.22: Large field-of-view measurements of pumping rates enabled by GCaMP8f expressed in pharyngeal muscles. Sample region showing animals expressing (A) GCaMP7f and (B) GCaMP8f in the pharynx at low magnification of 0.5×. The full field of view comprises 14mm × 10mm. (C) Examples of resulting fluorescence activity traces for GCaMP7f (top) and GCaMP8f (bottom) with peaks indicated in gray. (D) Average of the detected peaks corresponding to pumping events for GCaMP7f and GCaMP8f. (E) Pumping rate as measured from the peaks detected in c) and by manual counting of bright-field images at higher resolution. Note that the results for GCaMP7f are only displayed for comparison, as the lower quality of the trace yields many false detections and does not result in reliable measurements. *** indicates $P < 0.001$.Significance was assessed using a Kruskal–Wallis test followed by a post hoc Welch's unequal variance t-test. Multiple comparisons were corrected using the Bonferroni correction.

pressed GCaMP pan-neuronally frequently move slower than wild-type animals (Nguyen et al., 2017; Yemini et al., 2021). To estimate if calcium chelation is also detrimental to pharyngeal pumping and could impair the interpretation of such high-throughput measurements, we compared the pumping rate in bright-field images at high resolution for both strains with the wild-type strain N2. We found that animals expressing either GCaMP7f or GCaMP8f showed no significant difference in pumping rate from the wild type, suggesting that under these expression levels, muscle function is not impaired (3.21.E). In addition, we found that the pumping rate measured using GCaMP8f did not differ from the rate measured using high-resolution bright-field imaging (3.21.E).

We therefore conclude that this indicator enables robust, high-throughput analyses of feeding behavior which was not possible using GCaMP7f.

3.4.3 GCaMP8f unlocks sensitive measurement of activity in touch receptor neurons

Having successfully tested and validated GCaMP7f in *C. elegans* muscles, we wanted to confirm its application in neurons. This transition is crucial, as it allows us to explore whether the enhanced properties observed in muscles can be replicated in neurons. By using this GCaMP version to TRNs, we aimed to capture the full range of responses to our stimulus, including those at the lowest stimulus intensities, thus overcoming the limitations identified with the previous version.

As neurons are much smaller than the pharyngeal muscle, this typically requires higher magnifications and yields noisier, lower amplitude signals compared to the data shown in 3.21. We designed a plasmid containing both mKate2 and GCaMP8f with a similar construct than for GCaMP7f but replaced by GCaMP8f for direct comparison. Using confocal microscopy, we found similar expression of GCaMP8f and mKate2 in the six TRNs than for the previous construct (**Fig.** 3.23.A). We also observed that the activity in PLM scales linearly with stimulus amplitude. While we were unable to detect PLM activity with GCaMP7f at the lowest 2 stimulus levels, we were able to detect activity across all stimuli using GCaMP8f (**Fig. Fig.** 3.23.B and C; 3.24).

Although GCaMP7f has higher Ca^{2+} affinity (Kd = 150 nM) than GCaMP8f (Kd = 334 nM), it failed to detect PLM activity at low stimulus levels, while GCaMP8f succeeded. This is likely due to GCaMP8f's greater molecular brightness and faster kinetics, which improve signal amplitude and temporal resolution for brief Ca^{2+} transients (Zhang et al., 2023). While high-affinity sensors like GCaMP7f can bind Ca^{2+} at lower concentrations, their slower response and lower brightness may result in fluorescence changes that fall below the noise threshold. In contrast, GCaMP8f more effectively tracks rapid changes in intracellular Ca^{2+} concentration, generating stronger signals that rise above background noise. At higher stimulus intensities, where Ca^{2+} signals are sustained, slower high-affinity sensors like GCaMP7f can accumulate more bound complex and produce comparable fluorescence levels.

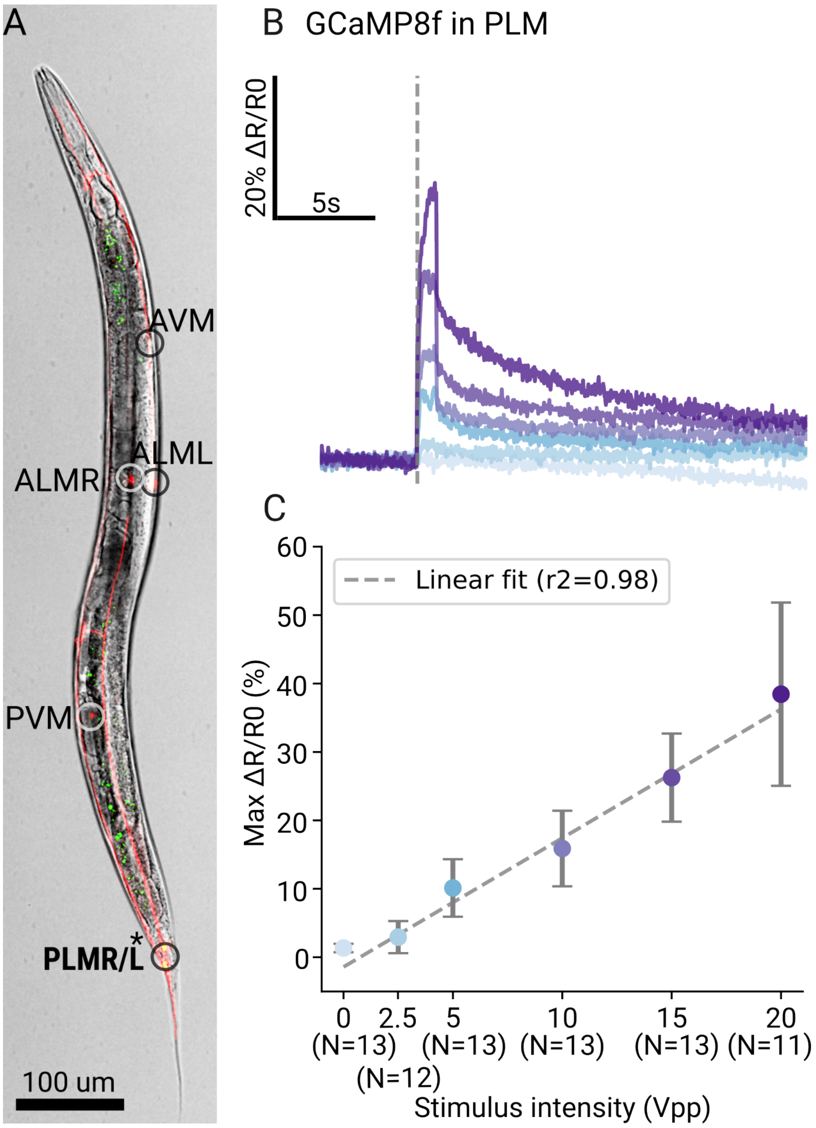

Figure 3.23: TRN encode linearly the task-relevant stimulus intensity. (A) Confocal microscopy image showing an animal expressing GCaMP8f (green) and mKate2 (red) in TRNs. Asterisks indicate the PLM neuron pair among the TRNs used to extract activity. (B) Population averaged responses of the PLM neurons to graded stimulus intensities using ratiometric correction. C. Stimulus intensity–response curve. The response was fitted with a linear model. Bars indicate the standard error of the mean at the maximal ratio change. The stimulus intensities are color coded in blues.

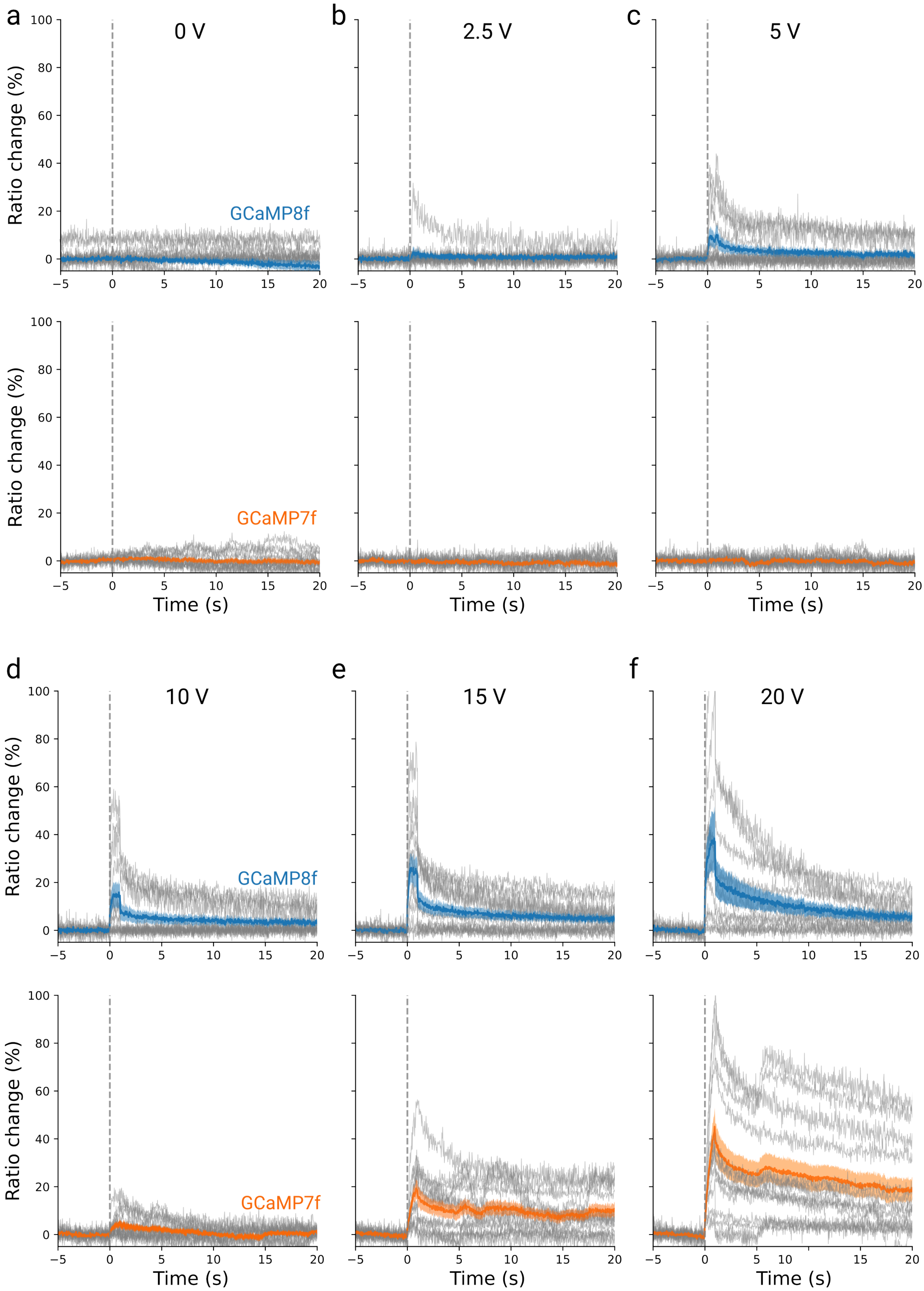

Figure 3.24: Individual PLM response dynamics over the full stimulus intensities range are differently captured by GCaMP8f and GCaMP7f indicators. (Caption continued on the next page)

Figure 3.24 (continued). Individual PLM response dynamics over the full stimulus intensities range are differently captured by GCaMP8f and GCaMP7f indicators. Individual traces of neuronal activity aligned to the stimulus onset (t = 0 s) and overlaid by their population average ± SEM for GCaMP7f (orange) and GCaMP8f (blue) respectively. Traces at stimulus intensity (A) 0 V (N = 13 for GCaMP8f, N = 15 for GCaMP7f) , (B) 2.5 V (N = 12 for GCaMP8f, N = 15 for GCaMP7f), (C) 5 V (N = 13 for GCaMP8f, N = 15 for GCaMP7f), (D) 10 V (N = 13 for GCaMP8f, N = 15 for GCaMP7f) (E) 15 V (N = 13 for GCaMP8f, N = 14 for GCaMP7f) and (F) 20 V (N = 11 for GCaMP8f, N = 15 for GCaMP7f).

In summary, we enabled sensitive calcium imaging in C. elegans muscles and neurons by adapting GCaMP8f. Our results in the PLM neurons demonstrate that the input layer of the touch-feeding circuit linearly encodes the stimulus intensities. The information about the full stimulus intensity range is therefore available for further processing in the circuit: upstream of the bottleneck, by the locomotion circuit where the speed response amplitude increases with the stimulus intensity range and downstream of the bottleneck, by the pharyngeal circuit, where the pumping response amplitude saturates. To determine if the bottleneck neurons filter the touch signal by intensity, we next aim to measure the neurometric curve in the RIP and I1 bottleneck neurons.

3.5 Evidence for both acute stimulus information and feeding state encoding in bottleneck neurons RIP

3.5.1 GCaMP8f signal in RIP or I1 neurons is not modulated by touch in immobilized animals

For reading out RIP and I1 activity, we used a similar approach than for the TRNs. We created transgenic lines expressing both GCaMP8f and mKate2 in the RIP and I1 neurons respectively. Blue light and shorter wavelengths have been shown to trigger an escape response and a pumping inhibition via extra and intra-pharyngeal pathways (Bhatla & Horvitz, 2015; Bhatla et al., 2015; Burr, 1985; S. L. Edwards et al., 2008; Gong et al., 2016; J. Liu et al., 2010; Ward et al., 2008). In order to exclude the possibility of any modulation of the bottleneck neurons by the light used to excite our calcium indicator (470 nm), we created new GCaMP8f lines for the TRNs, RIP and I1 neurons in the blue light insensitive background (*lite-1(ce314) gur-3(ok2245)* double mutants from Bhatla et al. (2015); strains INF204, INF559 and INF205 in List of Transgenic Lines).

We exposed immobilized animals to various buzz intensities. Contrary in the TRNs, GCaMP8f fails to report calcium change either as spontaneous activity or in response to touch in the RIP neurons (**Fig.** 3.25) and in the I1 neurons (data not shown). We also tested other GECIs (GCaMP6f, GCaMP7s and GCaMP7f) for reporting I1 activity either under a specific or pan-neuronal promoter and with different genetic background. However the basal GCaMP signal was barely or not visible except for GCaMP6f which might be a good alternative indicator (data not shown).

The animals were immobilized by levamisole. Although acetylcholine receptors sensitive to levamisole have only been identified in body wall muscles—outside of the pharynx—and in some extra-pharyngeal neurons (Holden-Dye et al., 2013; A. K. Jones & Sattelle, 2004), levamisole application results in pumping inhibition (Lockery et al., 2012). This effect has been suggested to result from body wall muscles signaling to the pharynx through two pathways: a fast neural signaling which would recruit the gap junctions to I1 neurons and a slow neuroendocrine signaling (Takahashi & Takagi, 2017). Furthermore, activity in RIP and/or I1 might be coupled to pharyngeal muscle activity. In order to exclude the possibility that an unbalanced motor feedback due to immobilization would prevent activity in the bottleneck neurons, we developed our calcium imaging setup further to enable simultaneous GCaMP8f/mKate2 ratiometric measurement in single neurons while monitoring pumping in freely moving animals.

3.5.2 Enabling of simultaneous measurement of feeding and neuronal calcium signal

A major challenge in monitoring neuronal calcium signals in freely moving *C. elegans* is maintaining signal stability. The small anatomical dimensions of its neurons — with somas typically between 2-5 µm in diameter and neurites smaller than 0.5 µm in width (White et al., 1986) necessitate using high-resolution optical systems. This requirement renders quantitative measurements highly sensitive to spatial displacement caused by animal movement. Closed-loop tracking systems with high spatial resolution detection, have been successfully employed for imaging single neurons and neuronal populations in freely moving *C. elegans* (Atanas et al., 2023; Nguyen et al., 2016; Venkatachalam et al., 2016). However, even within these sophisticated systems, animals are often artificially slowed and constrained in the z-axis to mitigate motion artifacts, typically by partial immobilization under a microscope slide on agarose pad (Atanas et al., 2023).Ratiometric measurements provide a complementary solution for correcting the residual artifacts. To circumvent the need for specialized hardware and software required by tracking systems, we developed an alternative approach using customized agarose micro-chambers spatially restraining the animal but allowing it to move within the chamber (**Fig.** 3.26.A). Leveraging our existing ratiometric calcium imaging setup described in **Section** 2.2, this chamber design

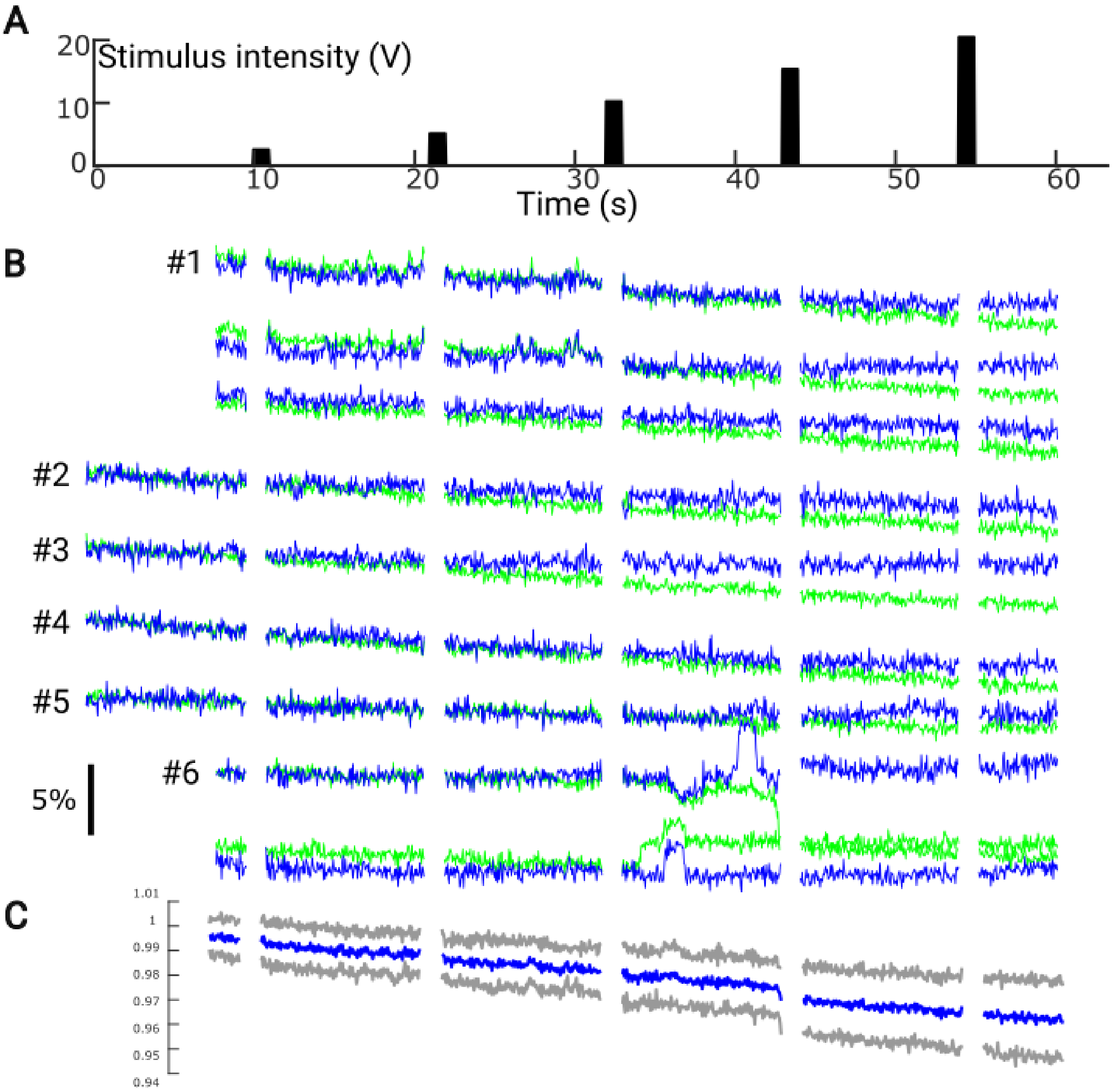

Figure 3.25: GCaMP8f does not report calcium changes in response to touch in the RIP neurons in immobilized animals. (A) Animals were exposed to graded stimulus intensities ranging from 2.5 to 20 V. (B) The normalized ratio between the GCaMP and red fluorophore signals (blue) and the GCaMP signal alone (green) in individual neurons (N =6) did not exhibit variations beyond noise levels (indicated by a scale bar showing changes below 5 %). (C) The population average of the normalized ratio ± STD, remains flat. Note: Signals during the 1-second stimulus period were excluded to reduce motion artifacts. The slight decay over time in the ratio, possibly due to bleaching, is less than 2 %

enabled the simultaneous capture of both GCaMP8f and mKate2 signals. (**Fig.** 3.26.D). Furthermore, by implementing a dedicated NIR imaging channel and a customized illumination system, we achieved simultaneous monitoring of pharyngeal pumping (**Fig.** 3.26.B and C).

We conducted a pilot experiment in which animals expressing GCaMP8f/mKate2 in theTRNs, RIP and I1 neurons respectively were exposed to touch stimuli at low (5 V) and high (20 V) intensity (strains INF204, INF559 and INF205 in List of Transgenic Lines). From this dataset, RIP neuron recordings were promising, reliably showing the neurons in focus over several tens of seconds. In contrast, I1 recordings were excluded from analysis due to a too low signal-to-noise ratio, and data from TRNs required further post-processing to account for focal plane shifts that disrupt neuron tracking and signal quality. As previously shown (**Fig.** 3.15), the low-intensity stimulus triggers no to mild pumping inhibition across the population, while the 20 V response is in the saturation range. Therefore, to investigate how RIP neurons may integrate stimulus signals, we focused our analysis on calcium signals in the RIP neuron and the pharyngeal pumping response to high-intensity stimulus.

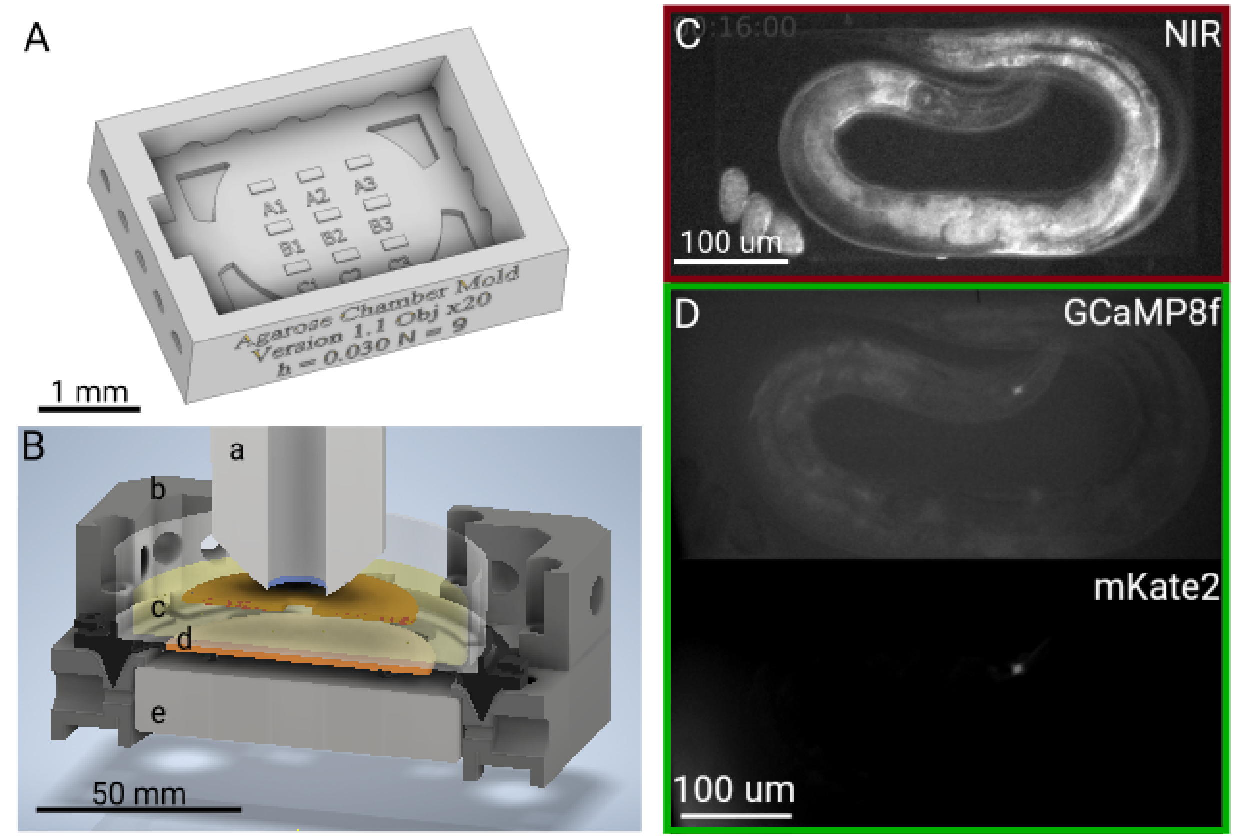

Figure 3.26: Simultaneous fluorescence and near-infrared imaging of neuronal activity and feeding in behaving *C. elegans* during substrate vibrations. (A) 3D-printed mold for preparing the agarose micro-chambers array. Individual chambers (250 × 500 × 30 μm) can host an adult worm providing sufficient space for lateral movement while restricting motion in the z. Scale bar: 1 mm. (B) Stimulus device positioned beneath the microscope objective (a). Key components include: the main housing with near-infrared (NIR) LEDs (b), a Petri dish (c) with a glued piezoelectric buzzer (d) for delivering vibrations, and a magnetic mount (e) for stable positioning. The dish contains an NGM agar block (yellow) supporting a copper ring (dark orange) that holds the micro-chamber array. Scale bar: 50 mm. (C) Field of view of the NIR camera, providing clear visualization of internal anatomy like the pharyngeal grinder. Scale bar: 100 μm. (D) Field of view from the dual-view fluorescence camera, showing simultaneous GCaMP8f (calcium indicator) and mKate2 (structural marker) in the I1 neurons in a representative animal (strain INF205 in List of Transgenic Lines).

3.5.3 RIP activity is driven by stimulus and feeding in behaving animals

We found that upon stimulation, the fluorescent signal ratio was reduced and coincided with a pumping inhibition (**Fig.** 3.27.C-D). This decrease suggest an inhibition of RIP activity upon touch stimulation. Both feeding suppression and RIP inhibition showed inter-animal variability, but we could reliably detect a significant reduction of both in the population averages of pumping and RIP responses (**Fig.** 3.27.E, F). Interestingly, the level of RIP inhibition and feeding suppression were correlated, indicating that the behavioral response can be decoded from RIP (**Fig.** 3.27.G). We also found that overall RIP activity reflects the pharyngeal activity on long timescales, with RIP activity and pumping rates showing a cross-correlation with the maximum at a lag time of 0.5 s (**Fig.** 3.27.I). Previous work using whole-brain imaging had also found this correlation, albeit with low sample number, as RIP does not reliably appear in some whole-brain experiments (Atanas et al., 2023). Beyond the gross baseline changes following tonic pharyngeal activity, we also observed rapid transients in the RIP signals that correlated with individual pharyngeal pumping contractions (**Fig.** 3.27.J). By aligning all detected pumping contractions, we could observe RIP activity preceding each pumping contraction (**Fig.** 3.27.K). Here, pumping was counted when the pharynx was maximally contracted, and RIP signals were extracted from the soma, which leaves the question open if these are efferent or afferent signals.

With our method, we could record simultaneously feeding and calcium signal in the RIP neurons as variation in the GCaMP to red fluorophore signal ratio. We found that calcium activity in RIP reflect both acute stimulus information, long-timescale pharyngeal activity and single-contraction level dynamics.

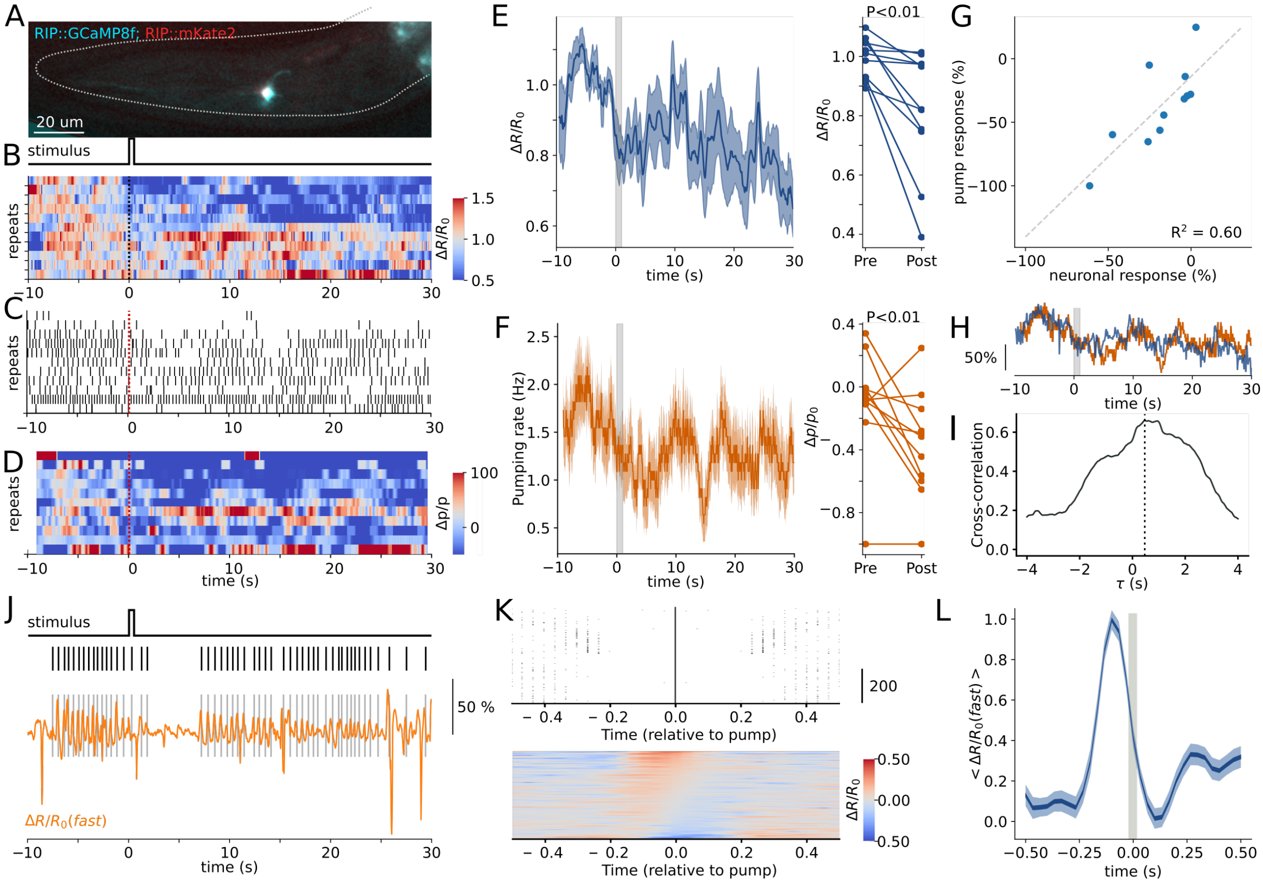

Figure 3.27: RIP neurons encode tonic feeding behavior and acute stimulus information as well as fast feeding motor signals. (A) RIP neurons labeled with two colors for ratiometric imaging. Activity around the soma was extracted. (B) Heatmap displaying single trial neuronal responses to a touch stimulus at t = 0 for 11 animal/repeats. (C) Pumping events before and after stimulation for the same trials as in B. (D) Pumping response score. E. Population average ± SEM of the neuronal activity in B. (F). Population average ± SEM of the pumping rate corresponding to the events in C. (G) Correlation of the pumping response and the neuronal response in a window 5 s after stimulation. (H) Overlay of the normalized pumping response and neuronal responses. Colors as in E and F. (I) Lagged cross-correlation of the traces in H. The dashed line indicates the maximum, which is at tau=0 s. Significance was assessed using a Mann-Whitney U-test. (J) baseline-subtracted fluorescence signal for a single animal trial. (K) behavior-triggered average showing all aligned pump events across all animals and trials and the corresponding calcium activity (heatmap). (L) Mean calcium activity for all pump events. The shaded area denotes the SEM.

4. Discussion

Neural bottlenecks, networks where inputs converge onto a limited number of neurons, represent a fundamental anatomical substrate for information compression. A key challenge is to measure the behaviorally-relevant information encoded in such a circuit. We designed a paradigm to study the function of the RIP-I1 neural bottleneck in *C. elegans* to experimentally measure how the behaviorally-relevant sensory information is represented in the input versus bottleneck layers.

4.1 Technical development

Several technical developments were required to achieve such measurements. First, we established a non-invasive optical method to automatically quantify feeding—the behavioral output of the RIP-I1 bottleneck— in freely moving animals (**Sections** 2.1 and 3.1; also published in Bonnard et al. (2022)). Second, we developed a system to deliver controlled substrate vibrations as mechanical stimuli (**Sections** 2.1, 3.2 and 3.3; partially published in J. Liu et al. (2024)). To achieve manipulation and activity measurement in the key neurons, we created new transgenic lines using cell-specific promoters for TRNs, RIP and I1 neurons, enabling genetic ablations (**Sections** 3.3, 3.4 and 3.5). Furthermore, we adapted the latest genetically encoded calcium indicator, GCaMP8f, for use in *C. elegans*, to reach the sensitivity required to measure calcium responses across the full behaviorally-relevant intensity range of substrate vibrations (**Section** 3.4, published in J. Liu et al. (2024)). Finally, we imaged the neuronal activity of the RIP neurons at behaviorally-relevant timescales and under stimulation by extending single-neuron calcium imaging from immobilized to freely behaving animals while simultaneously monitoring feeding behavior (Sections 3.5; manuscript in preparation).

4.2 Biological findings

These technical developments enable us to characterize the behavioral and neural representations of mechanosensory information through the RIP-I1 bottleneck. We found two distinct neuronal pathways driven touch-evoked behaviors: a robust, stereotyped escape response upstream of the bottleneck and a thresholded feeding inhibition via the RIP-I1 bottleneck. Furthermore, we provided functional evidence that the RIP-I1 circuit is a critical gateway for touch-induced modulation of feeding.

Based on these experiments, we identified distinct and independent pathways for escape and feeding. While almost all animals showed escape to substrate vibrations, only a subset showed feeding inhibition, and the temporal patterns of inhibition varied across individuals. Previous studies had looked at escape responses (X. Chen & Chalfie, 2014; Chiba & Rankin, 1990; Swierczek et al., 2011; Wicks & Rankin, 1995), however, no investigation simultaneously observed the effects of touch on escape and feeding circuits. Surprisingly, we found that those distinct behaviors are correlated neither in the basal state nor in responses to touch (**Fig.** 3.14 and 3.17). This dissociation in behaviors is supported by two distinct anatomical pathways: a fast, dedicated circuit for touch-escape (Goodman, 2006; Pirri & Alkema, 2012) and a touch-feeding circuit gated by the bottleneck. This architecture finds analogy in the startle response circuits, where a rapid, hardwired pathway ensures survival (D. H. Edwards et al., 1999; Katz, 1998; Korn & Faber, 2005)) distinct from more complex circuit mediating variable, state-dependent escape behaviors like found in zebrafish (Marquart et al., 2019). We speculate that the pumping response variability may arise from various arousal state (Horstick et al., 2016).

A fundamental difference emerged in how these pathways encode stimulus intensity. Escape speed increases with substrate vibrations amplitude (**Fig.** 3.15. In contrast, pharyngeal pumping inhibition saturated quickly at relatively low stimulus intensities, suggesting an ON-OFF response type compared to the graded escape output. This finding supports the hypothesis that the RIP-I1 bottleneck may act as a filter, preventing weak, potentially task-irrelevant mechanosensory signals from influencing pharyngeal activity. This is reminiscent of intensity-based filtering in decision-making circuits, such as those underlying go/no-go tasks (Sridhar et al., 2021). While our data point to the bottleneck as a likely site for this filtering, we cannot yet rule out that such gating could also be implemented at the level of the neuronal junctions onto the pharyngeal muscles or other intermediate layers. To distinguish these possibilities, further work should map the entire neurometric curve at the bottleneck layer, and investigate the role of the RIP-I1 gap junctions as possible rectifying elements (Starich et al., 2009).

Using cell-specific genetic ablations, we confirmed that substrate vibrations are detected in the six touch receptor neurons (TRNs), consistent with previous investigations (Chiba & Rankin, 1990; Wicks & Rankin, 1995). Crucially, we demonstrated for the first time that the RIP-I1 bottleneck is required for touch-evoked pumping inhibition (**Fig.** 3.19. Ablation of RIP or I1 neurons completely abolished the feeding response to mechanical stimuli without eliminating the escape response, providing direct functional evidence that the touch signal flow through this specific bottleneck to access the pharyngeal circuit. We therefore conclude that the bottleneck is required for transmitting touch signal to the pharynx.

Through single-neuron calcium imaging in immobilized animals, we confirmed that substrate vibrations evokes a rise in calcium in TRNs. The response amplitude increases linearly with vibrations amplitude, consistent with electrophysiological studies (Eastwood et al., 2015; Katta et al., 2019; O'Hagan et al., 2005) and calcium imaging data obtained with GCaMP6m (Cho et al., 2017). This linear representation of the stimulus intensity at the input layer is likely mirrored in the downstream escape circuit, providing a plausible neural basis for the graded locomotion speed we observed behaviorally.

A key unanswered question is whether the bottleneck neurons themselves implement the intensity threshold suggested by the behavioral saturation of feeding responses. Currently, we lack complete calcium imaging data mapping stimulus intensity to activity in the RIP and I1 neurons. However, our preliminary calcium imaging data in the RIP neurons — in both immobilized and behaving animals— indicate that their activity integrates multiple information streams, including the mechanosensory stimulus (Figures 3.25 and 3.27). This suggests thatRIP bottleneck neurons role may be more complex than a simple relay, potentially involving integration of sensory stimuli with the internal state to gate the flow of sensory information into the pharynx.

4.3 Limitations and further work

Several avenues for future research emerge from our findings and the technical challenges we encountered. Given the inter-animal variability in behavioral and neuronal responses, as well as the complex integration of multiple streams of information, a full understanding of this circuit would require observing all circuit elements at once. A promising solution are high-speed volumetric imaging techniques, such as light-sheet microscopy (Bouchard et al., 2015; Voleti et al., 2019) and similar whole-brain or multi-neuron imaging techniques (Atanas et al., 2023; Hallinen et al., 2021; Kato et al., 2015; Nguyen et al., 2016; Venkatachalam et al., 2016). Integrating volumetric imaging would significantly increase throughput by allowing visualization of the input, intermediate and bottleneck neurons, enabling the efficient collection of the large datasets required to fully map the neural dynamics during behavior.

A second technical challenge arose from the nature of the signals we aim to measure. We observed inhibitory responses in behavior (feeding suppression), and bottleneck neurons may themselves be inhibited (calcium decrease in RIP). Genetically encoded calcium indicators (GECIs), like GCaMP, are inherently better at reporting excitatory activity (calcium influx) than inhibitory activity (calcium removal). Therefore, genetically encoded voltage indicator (GEVI)s (Lin & Schnitzer, 2016) may provide a more direct and comprehensive measure of neuronal activity in this context, offering a clearer window into inhibitory signaling within the RIP-I1 circuit.

Finally, while our ablation studies established the requirement of the RIP-I1 bottleneck, they do not reveal the dynamic of their function. Our current system is ideally suited for optogenetic investigation. Precisely manipulating the activity of the bottleneck RIP and I1 neurons while monitoring pharyngeal pumping and neuronal calcium signals would establish a direct causal link with insight of the temporal regulations. This approach is critical for moving beyond correlation to a precise mechanistic understanding of how information flow through the bottleneck gates behavior.

4.4 Future research directions

Our data reveal a compelling paradox: sensory neurons (TRNs) display a graded, analog representation of stimulus intensity, yet the resulting feeding behavior is binary — either pausing or continuing pumping. This discrepancy suggests a fundamental transformation within the circuit, where a high-fidelity sensory signal is converted into a (near) discrete behavioral command.

A straightforward hypothesis is that an intermediate bottleneck-like layer represent a minimal energy expenditure to achieve dimensionality reduction (Muscinelli et al., 2023). The critical decision may be not be to modulate the pumping rate, but when to pause. This implies a shift from a rate-based code in the sensory layer to a temporal code governing motor output. The RIP-I1 bottleneck is in a key position to implement this computation. Future research should determine its specific algorithmic role: does it function as a coincidence detector, triggering a feeding pause only upon receiving a threshold-level input, or as a temporal integrator, averaging signals over time to make context-dependent decisions? Distinguishing between these models will require manipulating the temporal structure of stimuli while recording from bottleneck neurons and monitoring behavior. For instance, an integrator model would predict that a series of sub-threshold stimuli could sum to elicit a pause, whereas a coincidence detector would not (Diesmann et al., 1999; Jeanne & Wilson, 2015).

In both views, the circuit need not maintain high-information-content sensory signals representation all the way to the motor output to achieve goal-adapted behaviors. We speculate that analog encoding in the bottleneck layer is crucial for multifunctionality. A graded activity scale provides a richer substrate for integration than a binary state. The same RIP neurons likely integrate mechanosensory information with other internal states such as hunger or arousal, and external cues like olfactory signals—to produce context-appropriate behavioral outputs. Other studies have discussed that motor programs appear low-dimensional (Gallego et al., 2017; Saberski et al., 2021; Stephens et al., 2008) suggesting that once the complex multimodal integration is complete, a simplified decision signal is sufficient to adapt the motor pattern. Therefore, a central future direction is to move beyond single-modality stimulation. Experiments combining mechanical stimuli with perturbations of other sensory modalities or internal states will be essential to understand how the bottleneck circuit weights competing inputs to generate flexible, adaptive decisions.

In summary, this thesis provides an empirical examination of how neural bottlenecks compress behaviorally relevant information. Using touch-feeding system to study the function of RIP-I1 neural bottleneck in *C. elegans*, we established a framework to directly compare sensory representation between the input and bottleneck layers. We provided a first set of evidence for a lossy compression strategy, where sensory signals are filtered by intensity. Such compression is not merely a passive reduction but an active filtering process, gating information flow based on stimulus features and likely internal state.

Abstract

Neural bottlenecks are ubiquitous network motifs where multiple neurons project onto a smaller subset. This convergence suggests that the network compresses information encoded in incoming signals. However, measuring such compression remains challenging because it requires observing all the neurons involved, as well as the animal's behavior, to determine how much of the sensory information is used to guide behavior. RIP and I1 neurons in the nematode *C. elegans* are a compact implementation of a neural bottleneck where such measurements are possible. RIP receive massive converging sensory inputs and provide the only connections to the pharyngeal network controlling feeding via gap-junctions to the pharyngeal neurons I1. We developed a behavioral assay to deliver substrate vibrations as a controllable touch stimulus while automatically reading out the feeding behavior in freely moving *C. elegans*. We found that vibrations elicit both an escape response and a feeding inhibition. Both responses are abolished in mutants lacking the six touch receptor neurons (TRNs), whereas only the feeding response is abolished in animals where we genetically ablated RIP or I1 neurons, the escape circuit being upstream of the bottleneck. Furthermore, we showed that the escape response increases with the stimulus intensity, whereas the feeding response saturates at lower intensity, suggesting that the bottleneck may apply an intensity threshold to the touch signal. To determine how touch intensity information is encoded through the bottleneck, we adapted the calcium indicator GCaMP8f in *C. elegans* to enable sensitive measurements of neuronal activity in the input (TRNs) and bottleneck (RIP, I1) layers. Single neuron calcium imaging in immobilized animals showed that the input layer linearly encodes the behaviorally relevant stimulus intensity. However these experiments did not show activity in bottleneck neurons, indicating putative motor feedback. We therefore implemented simultaneous feeding and neuronal calcium imaging in behaving animals and showed that RIP activity is driven both by stimulus and feeding states. This provides a proof-of-concept for further measurements of intensity representation in the bottleneck layer. The touch-feeding system in *C. elegans* provides a neuroethological window to explore the role of neural bottleneck networks, potentially shedding light on generalizable principles of information compression.

List of Transgenic Lines

Aim 1, 2, 3

- **GRU101** (*gnaIs1*) — YFP in pharyngeal muscles (YFP pharynx) — CGC

Aim 1 (Feeding Measurement)

- **INF5** (*unc-31(e928); gnaIs1*) — UNC-31 mutants — Bonnard et al. 2022
- **INF17** (*unc-31(n1304); gnaIs1*) — UNC-31 mutants — Bonnard et al. 2022
- **INF44** (*eat-18(ad820); gnaIs1*) — EAT-18 mutant — Bonnard et al. 2022

Aim 2 (Neural Circuit Manipulations)

- **INF22** (*gnaIs1; mec-4(u253)*) — Touch insensitive (no MEC-4) with YFP pharynx
- **INF127** (*nonIs4; syIs390*) — GFP in I1 neurons
- **INF206** (*gnaIs1; mec-4(e1611)*) — Touch insensitive (no TRNs) with YFP pharynx
- **INF407** (*nonIs4; nonIs8*) — I1 driver with mCherry pharynx
- **INF411** (*nonIs4; syIs413; syIs390*) — I1-ablated (GFP and ICE in I1)
- **INF417** (*syIs390; syIs413*) — I1-ablated with mCherry pharynx
- **INF529** (*syIs390; syIs413; nonIs11; nonEx64*) — RIP-ablated with mCherry pharynx
- **INF530** (*syIs390; nonIs11; nonEx64*) — RIP driver with mCherry pharynx
- **INF556** (*gnaIs1 nonIs4*) — I1 driver II with YFP pharynx
- **INF557** (*gnaIs1 nonIs4; nonEx166*) — Gap-junction mutant with YFP pharynx

Aim 3 (Calcium Imaging)

- **INF204** (*lite-1(ce314) gur-3(ok2245); nonEx133*) — GCaMP8f/mKate2 in TRNs (light-insensitive)

- **INF205** (*lite-1(ce314) gur-3(ok2245); nonEx138*) — GCaMP8f/mKate2 in I1 (light-insensitive)
- **INF418** (*nonEx106*) — GCaMP8f in pharyngeal muscles — Liu et al. 2024
- **INF447** (*nonEx133*) — GCaMP8f in TRNs — Liu et al. 2024
- **INF491** (*nonEx105*) — GCaMP7f in pharyngeal muscles — Liu et al. 2024
- **INF498** (*nonEx158*) — GCaMP7f in TRNs — Liu et al. 2024
- **INF559** (*lite-1(ce314) gur-3(ok2245); nonEx157*) — GCaMP8f/mKate2 in RIP (light-insensitive)

Detailed genotype

- *gnaIs1[myo-2p::yfp] IV*
- *syIs390[15xUAS::?pes-10::GFP::let-858 3'UTR + ttx-3p::RFP + 1kb DNA ladder(NEB)] IV*
- *syIs413[15xUAS::?pes-10::ICE::let-858 3'UTR + unc-122p::GFP + pBlueScript]*

- *nonIs4[Plgc-8::NLS::cGAL(DBD):: cGAL(AD)::let-858 3'UTR + coel::RFP] IV*
- *nonIs8[myo-2p::mCherry]*
- *nonIs11 [Pnlp-51::NLS::cGAL(DBD):: cGAL(AD)::let-858 3'UTR]*
- *nonEx166[15xUAS::pes-10::unc-1(n494)::let-858 3'UTR, rab-3p::BFP]*
- *nonEx105[myo-2p::GCaMP7f]*
- *nonEx106[myo-2p::GCaMP8f::unc-54 3'UTR]*
- *nonEx133[Pmec-17_GCaMP8f_SL2_mKate2_let-858_3'UTR + Punc-122::tagBFP]*
- *nonEx138[Plgc-8_GCaMP8f_SL2_mKate2_let-858_3'UTR]*
- *nonEx157[Pnlp-51_GCaMP8f_SL2_mKate2_let-858_3'UTR + Prab-3::tagBFP]*
- *nonEx158[mec-17p_GCaMP7f_SL2_mKate2_let-858_3'UTR + unc-122p::tagBFP]*

List of Figures

List of Tables

Bibliography

Albertson, D. G., & Thomson, J. N. (1976). The pharynx of *Caenorhabditis elegans*. *Philos. Trans. R. Soc. Lond., B, Biol. Sci.*, *275*(938), 299–325. https://doi.org/10.1098/rstb.1976.0085

Allan, D. B., Caswell, T., Keim, N. C., van der Wel, C. M., & Verweij, R. W. (2021). *Soft-matter/trackpy: Trackpy v0.5.0*. Zenodo. https://doi.org/10.5281/zenodo.4682814

Andersen, E. C., Bloom, J. S., Gerke, J. P., & Kruglyak, L. (2014). A variant in the neuropeptide receptor npr-1 is a major determinant of *Caenorhabditis elegans* growth and physiology. *PLoS Genet*, *10*(2), e1004156. https://doi.org/10.1371/journal.pgen.1004156

Arnadottir, J., O'Hagan, R., Chen, Y., Goodman, M. B., & Chalfie, M. (2011). The DEG/ENaC protein MEC-10 regulates the transduction channel complex in *Caenorhabditis elegans* touch receptor neurons. *J. Neurosci.*, *31*(35), 12695–12704. https://doi.org/10.1523/jneurosci.4580-10.2011

Atanas, A. A., Kim, J., Wang, Z., Bueno, E., Becker, M., Kang, D., Park, J., Kramer, T. S., Wan, F. K., Baskoylu, S., Dag, U., Kalogeropoulou, E., Gomes, M. A., Estrem, C., Cohen, N., Mansinghka, V. K., & Flavell, S. W. (2023). Brain-wide representations of behavior spanning multiple timescales and states in *C. elegans*. *Cell*, *186*(19), 4134–4151.e31. https://doi.org/10.1016/j.cell.2023.07.035

Avery, L. (1993). Motor neuron m3 controls pharyngeal muscle relaxation timing in *Caenorhabditis elegans*. *J Exp Biol*, *175*, 283–297.

Avery, L., & Horvitz, H. R. (1990). Effects of starvation and neuroactive drugs on feeding in *Caenorhabditis elegans*. *J Exp Zool*, *253*(3), 263–270. https://doi.org/10.1002/jez.1402530305

Avery, L., & Shtonda, B. B. (2003). Food transport in the *C. elegans* pharynx. *J Exp Biol*, *206*(0), 2441–2457. Retrieved November 28, 2021, from https://www.ncbi.nlm.nih.gov/pmc/articles/PMC3951750/

Barlow, H. (1961). Possible principles underlying the transformations of sensory messages. *Sensory Communication*, *1*. https://doi.org/10.7551/mitpress/9780262518420.003.0013

Bhandawat, V., Olsen, S. R., Gouwens, N. W., Schlief, M. L., & Wilson, R. I. (2007). Sensory processing in the *Drosophila* antennal lobe increases reliability and separability of ensemble odor representations. *Nat Neurosci*, *10*(11), 1474–1482. https://doi.org/10.1038/nn1976

Bhatla, N., Droste, R., Sando, S. R., Huang, A., & Horvitz, H. R. (2015). Distinct neural circuits control rhythm inhibition and spitting by the myogenic pharynx of *C. elegans*. *Current Biology*, *25*(16), 2075–2089. https://doi.org/10.1016/j.cub.2015.06.052

Bhatla, N., & Horvitz, H. R. (2015). Light and hydrogen peroxide inhibit *C. elegans* feeding through gustatory receptor orthologs and pharyngeal neurons. *Neuron*, *85*(4), 804–818. https://doi.org/10.1016/j.neuron.2014.12.061

Bonnard, E., Liu, J., Zjacic, N., Alvarez, L., & Scholz, M. (2022). Automatically tracking feeding behavior in populations of foraging *C. elegans*. *eLife*, *11*, e77252. https://doi.org/10.7554/eLife.77252

Bouchard, M. B., Voleti, V., Mendes, C. S., Lacefield, C., Grueber, W. B., Mann, R. S., Bruno, R. M., & Hillman, E. M. C. (2015). Swept confocally-aligned planar excitation (SCAPE) microscopy for high-speed volumetric imaging of behaving organisms. *Nature Photon*, *9*(2), 113–119. https://doi.org/10.1038/nphoton.2014.323

Brodal, P., & Bjaalie, J. G. (1992). Organization of the pontine nuclei. *Neuroscience Research*, *13*(2), 83–118. https://doi.org/10.1016/0168-0102(92)90092-Q

Brown, A. L., Fernandez-Illescas, S. M., Liao, Z., & Goodman, M. B. (2007). Gain-of-function mutations in the MEC-4 DEG/ENaC sensory mechanotransduction channel alter gating and drug blockade. *J Gen Physiol*, *129*(2), 161–173. https://doi.org/10.1085/jgp.200609672

Bueschges, A., & Ache, J. M. (2025). Motor control on the move: From insights in insects to general mechanisms. *Physiological Reviews*, *105*(3), 975–1031. https://doi.org/10.1152/physrev.00009.2024

Burr, A. H. (1985). The photomovement of *Caenorhabditis elegans*, a nematode which lacks ocelli. proof that the response is to light not radiant heating. *Photochemistry and Photobiology*, *41*(5), 577–582. https://doi.org/10.1111/j.1751-1097.1985.tb03529.x

Calhoun, A. J., Chalasani, S. H., & Sharpee, T. O. (2014). Maximally informative foraging by *Caenorhabditis elegans*. *eLife*, *3*, e04220. https://doi.org/10.7554/eLife.04220

Cermak, N., Yu, S. K., Clark, R., Huang, Y.-C., Baskoylu, S. N., & Steven W Flavell. (2020). Whole-organism behavioral profiling reveals a role for dopamine in state-dependent motor program coupling in *C. elegans*. *eLife*, *9*, e57093. https://doi.org/10.7554/eLife.57093

Cerretti, D. P., Kozlosky, C. J., Mosley, B., Nelson, N., Van Ness, K., Greenstreet, T. A., March, C. J., Kronheim, S. R., Druck, T., & Cannizzaro, L. A. (1992). Molecular cloning of the interleukin-1 beta converting enzyme. *Science*, *256*(5053), 97–100. https://doi.org/10.1126/science.1373520

Chalfie, M., Sulston, J. E., White, J. G., Southgate, E., Thomson, J. N., & Brenner, S. (1985). The neural circuit for touch sensitivity in *Caenorhabditis elegans*. *J. Neurosci.*, *5*(4), 956–964. https://doi.org/10.1523/jneurosci.05-04-00956.1985

Chen, B., Liu, Q., Ge, Q., Xie, J., & Wang, Z.-W. (2007). UNC-1 regulates gap junctions important to locomotion in *C. elegans*. *Curr Biol*, *17*(15), 1334–1339. https://doi.org/10.1016/j.cub.2007.06.060

Chen, X., & Chalfie, M. (2014). Modulation of *C. elegans* touch sensitivity is integrated at multiple levels. *J. Neurosci.*, *34*(19), 6522–6536. https://doi.org/10.1523/jneurosci.0022-14.2014

Chiba, C. M., & Rankin, C. H. (1990). A developmental analysis of spontaneous and reflexive reversals in the nematode *Caenorhabditis elegans*. *Journal of Neurobiology*, *21*(4), 543–554. https://doi.org/10.1002/neu.480210403

Cho, Y., Porto, D. A., Hwang, H., Grundy, L. J., Schafer, W. R., & Lu, H. (2017). Automated and controlled mechanical stimulation and functional imaging *in vivo* in *C. elegans*. *Lab Chip*, *17*(22), 3935. https://doi.org/10.1039/c7lc90104f

Choudhary, S., Buxton, S. K., Puttachary, S., Verma, S., Mair, G. R., McCoy, C. J., Reaves, B. J., Wolstenholme, A. J., Martin, R. J., & Robertson, A. P. (2020). EAT-18 is an essential auxiliary protein interacting with the non-alpha nAChR subunit EAT-2 to form a functional receptor. *PLoS Pathogens*, *16*(4), e1008396. https://doi.org/10.1371/journal.ppat.1008396

Clark, D. A., Biron, D., Sengupta, P., & Samuel, A. D. T. (2006). The AFD sensory neurons encode multiple functions underlying thermotactic behavior in *Caenorhabditis elegans*. *J Neurosci*, *26*(28), 7444–7451. https://doi.org/10.1523/jneurosci.1137-06.2006

Cook, S. J., Crouse, C. M., Yemini, E., Hall, D. H., Emmons, S. W., & Hobert, O. (2020). The connectome of the *Caenorhabditis elegans* pharynx. *Journal of Comparative Neurology*, *528*(16), 2767–2784. https://doi.org/10.1002/cne.24932

Cook, S. J., Jarrell, T. A., Brittin, C. A., Wang, Y., Bloniarz, A. E., Yakovlev, M. A., Nguyen, K. C. Q., Tang, L. T.-H., Bayer, E. A., Duerr, J. S., Bülow, H. E., Hobert, O., Hall, D. H., & Emmons, S. W. (2019). Whole-animal connectomes of both *Caenorhabditis elegans* sexes. *Nature*, *571*(7763), 63–71. https://doi.org/10.1038/s41586-019-1352-7

Dallière, N., Bhatla, N., Luedtke, Z., Ma, D. K., Woolman, J., Walker, R. J., Holden-Dye, L., & O'Connor, V. (2016). Multiple excitatory and inhibitory neural signals converge to fine-tune *Caenorhabditis elegans* feeding to food availability. *FASEB J*, *30*(2), 836–848. https://doi.org/10.1096/fj.15-279257

Dana, H., Sun, Y., Mohar, B., Hulse, B. K., Kerlin, A. M., Hasseman, J. P., Tsegaye, G., Tsang, A., Wong, A., Patel, R., Macklin, J. J., Chen, Y., Konnerth, A., Jayaraman, V., Looger, L. L., Schreiter, E. R., Svoboda, K., & Kim, D. S. (2019). High-performance calcium sensors for imaging activity in neuronal populations and microcompartments. *Nat Methods*, *16*(7), 649–657. https://doi.org/10.1038/s41592-019-0435-6

Davis, K. C., Choi, Y.-I., Kim, J., & You, Y.-J. (2018). Satiety behavior is regulated by ASI/ASH reciprocal antagonism. *Sci Rep*, *8*(1), 6918. https://doi.org/10.1038/s41598-018-24943-6

De Magalhaes Filho, C. D., Henriquez, B., Nicole E. Seah, Evans, R. M., Lapierre, L. R., & Dillin, A. (2018). Visible light reduces *C. elegans* longevity. *Nat Commun*, *9*(1), 927. https://doi.org/10.1038/s41467-018-02934-5

Diesmann, M., Gewaltig, M.-O., & Aertsen, A. (1999). Stable propagation of synchronous spiking in cortical neural networks. *Nature*, *402*(6761), 529–533. https://doi.org/10.1038/990101

Dillon, J., Holden-Dye, L., O'Connor, V., & Hopper, N. A. (2016). Context-dependent regulation of feeding behaviour by the insulin receptor, DAF-2, in *Caenorhabditis elegans*. *Invert Neurosci*, *16*(2), 4. https://doi.org/10.1007/s10158-016-0187-2

Ding, S. S., Romenskyy, M., Sarkisyan, K. S., & Brown, A. E. X. (2020). Measuring *Caenorhabditis elegans* spatial foraging and food intake using bioluminescent bacteria. *Genetics*, *214*(3), 577–587. https://doi.org/10.1534/genetics.119.302804

Duffy, J. B. (2002). GAL4 system in *Drosophila* : A fly geneticist's swiss army knife. *34*(1), 1–15. https://doi.org/10.1002/gene.10150

Eastwood, A. L., Sanzeni, A., Petzold, B. C., Park, S.-J., Vergassola, M., Pruitt, B. L., & Goodman, M. B. (2015). Tissue mechanics govern the rapidly adapting and symmetrical response to touch. *PNAS*, *112*(50), E6955–E6963. https://doi.org/10.1073/pnas.1514138112

Edwards, D. H., Heitler, W. J., & Krasne, F. B. (1999). Fifty years of a command neuron: The neurobiology of escape behavior in the crayfish. *Trends Neurosci.*, *22*(4), 153–161. https://doi.org/10.1016/S0166-2236(98)01340-X

Edwards, S. L., Charlie, N. K., Milfort, M. C., Brown, B. S., Gravlin, C. N., Knecht, J. E., & Miller, K. G. (2008). A novel molecular solution for ultraviolet light detection in *Caenorhabditis elegans*. *PLoS Biol*, *6*(8), e198. https://doi.org/10.1371/journal.pbio.0060198

Fang-Yen, C., Avery, L., & Samuel, A. D. T. (2009). Two size-selective mechanisms specifically trap bacteria-sized food particles in *Caenorhabditis elegans*. *Proc Natl Acad Sci U S A*, *106*(47), 20093–20096. https://doi.org/10.1073/pnas.0904036106

Flavell, S. W., Pokala, N., Macosko, E. Z., Albrecht, D. R., Larsch, J., & Bargmann, C. I. (2013). Serotonin and the neuropeptide PDF initiate and extend opposing behavioral states in *C. elegans*. *Cell*, *154*(5), 1023–1035. https://doi.org/10.1016/j.cell.2013.08.001

Gallagher, T., Kim, J., Oldenbroek, M., Kerr, R., & You, Y.-J. (2013). ASI regulates satiety quiescence in *C. elegans*. *J. Neurosci.*, *33*(23), 9716–9724. https://doi.org/10.1523/jneurosci.4493-12.2013

Gallego, J. A., Perich, M. G., Miller, L. E., & Solla, S. A. (2017). Neural manifolds for the control of movement. *Neuron*, *94*(5), 978–984. https://doi.org/10.1016/j.neuron.2017.05.025

Girard, L. R., Fiedler, T. J., Harris, T. W., Carvalho, F., Antoshechkin, I., Han, M., Sternberg, P. W., Stein, L. D., & Chalfie, M. (2007). WormBook: The online review of caenorhabditis elegans biology. *Nucleic Acids Res*, *35*, D472–475. https://doi.org/10.1093/nar/gkl894

Gomez-Amaro, R. L., Valentine, E. R., Carretero, M., LeBoeuf, S. E., Rangaraju, S., Broaddus, C. D., Solis, G. M., Williamson, J. R., & Petrascheck, M. (2015). Measuring food intake and nutrient absorption in *Caenorhabditis elegans*. *Genetics*, *200*(2), 443–454. https://doi.org/10.1534/genetics.115.175851

Gong, J., Yuan, Y., Ward, A., Kang, L., Zhang, B., Wu, Z., Peng, J., Feng, Z., Liu, J., & Xu, X. Z. S. (2016). The *C. elegans* taste receptor homolog LITE-1 is a photoreceptor. *Cell*, *167*(5), 1252–1263.e10. https://doi.org/10.1016/j.cell.2016.10.053

Goodman, M. B. (2006). Mechanosensation. *WormBook*. https://doi.org/doi/10.1895/wormbook.1.62.1

Goodman, M. B., Hall, D. H., Avery, L., & Lockery, S. R. (1998). Active currents regulate sensitivity and dynamic range in *C. elegans neurons*. *Neuron*, *20*(4), 763–772. https://doi.org/10.1016/s0896-6273(00)81014-4

Goodman, M. B., & Sengupta, P. (2019). How *Caenorhabditis elegans* senses mechanical stress, temperature, and other physical stimuli. *Genetics*, *212*(1), 25–51. https://doi.org/10.1534/genetics.118.300241

Gray, J. M., Hill, J. J., & Bargmann, C. I. (2005). A circuit for navigation in *Caenorhabditis elegans*. *Proceedings of the National Academy of Sciences*, *102*(9), 3184–3191. https://doi.org/10.1073/pnas.0409009101

Gruninger, T. R., Gualberto, D. G., LeBoeuf, B., & Garcia, L. R. (2006). Integration of male mating and feeding behaviors in *Caenorhabditis elegans*. *J Neurosci*, *26*(1), 169–179. https://doi.org/10.1523/jneurosci.3364-05.2006

Hallinen, K. M., Dempsey, R., Scholz, M., Yu, X., Linder, A., Randi, F., Sharma, A. K., Shaevitz, J. W., & Leifer, A. M. (2021). Decoding locomotion from population neural activity in moving *C. elegans*. *eLife*, *10*, e66135. https://doi.org/10.7554/eLife.66135

Hendricks, M., Ha, H., Maffey, N., & Zhang, Y. (2012). Compartmentalized calcium dynamics in a *C. elegans* interneuron encode head movement. *Nature*, *487*(7405), 99–103. https://doi.org/10.1038/nature11081

Hills, T., Brockie, P. J., & Maricq, A. V. (2004). Dopamine and glutamate control area-restricted search behavior in *Caenorhabditis elegans*. *J Neurosci*, *24*(5), 1217–1225. https://doi.org/10.1523/jneurosci.1569-03.2004

Holden-Dye, L., Joyner, M., O'Connor, V., & Walker, R. J. (2013). Nicotinic acetylcholine receptors: A comparison of the nAChRs of *Caenorhabditis elegans* and parasitic nematodes. *Parasitology International*, *62*(6), 606–615. https://doi.org/10.1016/j.parint.2013.03.004

Hong, K., Mano, I., & Driscoll, M. (2000). *In vivo* structure–function analyses of *Caenorhabditis elegans* MEC-4, a candidate mechanosensory ion channel subunit. *J. Neurosci.*, *20*(7), 2575–2588. https://doi.org/10.1523/jneurosci.20-07-02575.2000

Horstick, E. J., Mueller, T., & Burgess, H. A. (2016). Motivated state control in larval zebrafish: Behavioral paradigms and anatomical substrates. *Journal of Neurogenetics*, *30*(2), 122–132. https://doi.org/10.1080/01677063.2016.1177048

Huang, M., & Chalfie, M. (1994). Gene interactions affecting mechanosensory transduction in *Caenorhabditis elegans*. *Nature*, *367*(6462), 467–470. https://doi.org/10.1038/367467a0

Humphries, M. D. (2025). The computational bottleneck of basal ganglia output (and what to do about it). *eNeuro*, *12*(4). https://doi.org/10.1523/eneuro.0431-23.2024

Inoue, M. (2021). Genetically encoded calcium indicators to probe complex brain circuit dynamics *in vivo*. *Neuroscience Research*, *169*, 2–8. https://doi.org/10.1016/j.neures.2020.05.013

Itskovits, E., Ruach, R., Kazakov, A., & Zaslaver, A. (2018). Concerted pulsatile and graded neural dynamics enables efficient chemotaxis in *C. elegans*. *Nat Commun*, *9*, 2866. https://doi.org/10.1038/s41467-018-05151-2

Iwanir, S., Brown, A. S., Nagy, S., Najjar, D., Kazakov, A., Lee, K. S., Zaslaver, A., Levine, E., & Biron, D. (2016). Serotonin promotes exploitation in complex environments by accelerating decision-making. *BMC Biology*, *14*(1), 9. https://doi.org/10.1186/s12915-016-0232-y

Jang, H., Levy, S., Flavell, S. W., Mende, F., Latham, R., Zimmer, M., & Bargmann, C. I. (2017). Dissection of neuronal gap junction circuits that regulate social behavior in *Caenorhabditis elegans*. *Proc Natl Acad Sci U S A*, *114*(7), E1263–E1272. https://doi.org/10.1073/pnas.1621274114

Jeanne, J. M., & Wilson, R. I. (2015). Convergence, divergence, and reconvergence in a feedforward network improves neural speed and accuracy. *Neuron*, *88*(5), 1014–1026. https://doi.org/10.1016/j.neuron.2015.10.018

Jiang, J., Su, Y., Zhang, R., Li, H., Tao, L., & Liu, Q. (2022). *C. elegans* enteric motor neurons fire synchronized action potentials underlying the defecation motor program. *Nat Commun*, *13*(1), 2783. https://doi.org/10.1038/s41467-022-30452-y

Jones, A. K., & Sattelle, D. B. (2004). Functional genomics of the nicotinic acetylcholine receptor gene family of the nematode, *Caenorhabditis elegans*. *Bioessays*, *26*(1), 39–49. https://doi.org/10.1002/bies.10377

Jones, E. G. (2000). Cortical and subcortical contributions to activity-dependent plasticity in primate somatosensory cortex. *Annu Rev Neurosci*, *23*, 1–37. https://doi.org/10.1146/annurev.neuro.23.1.1

Kato, S., Kaplan, H. S., Schrödel, T., Skora, S., Lindsay, T. H., Yemini, E., Lockery, S., & Zimmer, M. (2015). Global brain dynamics embed the motor command sequence of *Caenorhabditis elegans*. *Cell*, *163*(3), 656–669. https://doi.org/10.1016/j.cell.2015.09.034

Katta, S., Sanzeni, A., Das, A., Vergassola, M., & Goodman, M. B. (2019). Progressive recruitment of distal MEC-4 channels determines touch response strength in *C. elegans*. *Journal of General Physiology*, *151*(10), 1213–1230. https://doi.org/10.1085/jgp.201912374

Katz, P. S. (1998). Neuromodulation intrinsic to the central pattern generator for escape swimming in tritonia. *Annals of the New York Academy of Sciences*, *860*(1), 181–188. https://doi.org/10.1111/j.1749-6632.1998.tb09048.x

Katzen, A., Chung, H.-K., Harbaugh, W. T., Della Iacono, C., Jackson, N., Glater, E. E., Taylor, C. J., Yu, S. K., Flavell, S. W., Glimcher, P. W., Andreoni, J., & Lockery, S. R. (2023). The nematode worm *C. elegans* chooses between bacterial foods as if maximizing economic utility. *eLife*, *12*, e69779. https://doi.org/10.7554/eLife.69779

Keane, J., & Avery, L. (2003). Mechanosensory inputs influence *Caenorhabditis elegans* pharyngeal activity via ivermectin sensitivity genes. *Genetics*, *164*(1), 153–162. Retrieved July 22, 2020, from https://www.genetics.org/content/164/1/153

Kerr, R., Lev-Ram, V., Baird, G., Vincent, P., Tsien, R. Y., & Schafer, W. R. (2000). Optical imaging of calcium transients in neurons and pharyngeal muscle of *C. elegans*. *Neuron*, *26*(3), 583–594. https://doi.org/10.1016/S0896-6273(00)81196-4

Kiyama, Y., Miyahara, K., & Ohshima, Y. (2012). Active uptake of artificial particles in the nematode *Caenorhabditis elegans*. *J Exp Biol*, *215*, 1178–1183. https://doi.org/10.1242/jeb.067199

Knight, C. G., Patel, M. N., Azevedo, R. B. R., & Leroi, A. M. (2002). A novel mode of ecdysozoan growth in *Caenorhabditis elegans*. *Evol Dev*, *4*(1), 16–27. https://doi.org/10.1046/j.1525-142x.2002.01058.x

Korn, H., & Faber, D. S. (2005). The mauthner cell half a century later: A neurobiological model for decision-making? *Neuron*, *47*(1), 13–28. https://doi.org/10.1016/j.neuron.2005.05.019

Krakauer, J. W., Ghazanfar, A. A., Gomez-Marin, A., MacIver, M. A., & Poeppel, D. (2017). Neuroscience needs behavior: Correcting a reductionist bias. *Neuron*, *93*(3), 480–490. https://doi.org/10.1016/j.neuron.2016.12.041

Larsch, J., Flavell, S. W., Liu, Q., Gordus, A., Albrecht, D. R., & Bargmann, C. I. (2015). A circuit for gradient climbing in *C. elegans* chemotaxis. *Cell Rep*, *12*(11), 1748–1760. https://doi.org/10.1016/j.celrep.2015.08.032

Lee, K. S., Iwanir, S., Kopito, R. B., Scholz, M., Calarco, J. A., Biron, D., & Levine, E. (2017). Serotonin-dependent kinetics of feeding bursts underlie a graded response to food availability in *C. elegans*. *Nature Communications*, *8*(1), 1–11. https://doi.org/10.1038/ncomms14221

Levi, A., Spivak, L., Sloin, H. E., Someck, S., & Stark, E. (2022). Error correction and improved precision of spike timing in converging cortical networks. *Cell Rep*, *40*(12), 111383. https://doi.org/10.1016/j.celrep.2022.111383

Li, Z., Li, Y., Yi, Y., Huang, W., Yang, S., Niu, W., Zhang, L., Xu, Z., Qu, A., Wu, Z., & Xu, T. (2012). Dissecting a central flip-flop circuit that integrates contradictory sensory cues in *C. elegans* feeding regulation. *Nature Communications*, *3*(1), 776. https://doi.org/10.1038/ncomms1780

Lin, M. Z., & Schnitzer, M. J. (2016). Genetically encoded indicators of neuronal activity. *Nat Neurosci*, *19*(9), 1142–1153. https://doi.org/10.1038/nn.4359

Liu, J., Ward, A., Gao, J., Dong, Y., Nishio, N., Inada, H., Kang, L., Yu, Y., Ma, D., Xu, T., Mori, I., Xie, Z., & Xu, X. Z. S. (2010). *C. elegans* phototransduction requires a g protein–dependent cGMP pathway and a taste receptor homolog. *Nat Neurosci*, *13*(6), 715–722. https://doi.org/10.1038/nn.2540

Liu, J., Bonnard, E., & Scholz, M. (2024). Adapting and optimizing GCaMP8f for use in *Caenorhabditis elegans*. *Genetics*, iyae125. https://doi.org/10.1093/genetics/iyae125

Liu, Q., Kidd, P. B., Dobosiewicz, M., & Bargmann, C. I. (2018). *C. elegans* AWA olfactory neurons fire calcium-mediated all-or-none action potentials. *Cell*, *175*(1), 57–70.e17. https://doi.org/10.1016/j.cell.2018.08.018

Lledo, P.-M., Gheusi, G., & Vincent, J.-D. (2005). Information processing in the mammalian olfactory system. *Physiological Reviews*, *85*(1), 281–317. https://doi.org/10.1152/physrev.00008.2004

Lockery, S. R., Hulme, S. E., Roberts, W. M., Robinson, K. J., Laromaine, A., Lindsay, T. H., Whitesides, G. M., & Weeks, J. C. (2012). A microfluidic device for whole-animal drug screening using electrophysiological measures in the nematode *C. elegans*. *Lab Chip*, *12*(12), 2211–2220. https://doi.org/10.1039/C2LC00001F

Marquart, G. D., Tabor, K. M., Bergeron, S. A., Briggman, K. L., & Burgess, H. A. (2019). Prepontine non-giant neurons drive flexible escape behavior in zebrafish. *PLoS Biol*, *17*(10), e3000480. https://doi.org/10.1371/journal.pbio.3000480

McClanahan, P. D., Dubuque, J. M., Kontogiorgos-Heintz, D., Habermeyer, B. F., Xu, J. H., Ma, A. M., Raizen, D. M., & Fang-Yen, C. (2020). A quiescent state following mild sensory arousal in *Caenorhabditis elegans* is potentiated by stress. *Sci Rep*, *10*(1), 4140. https://doi.org/10.1038/s41598-020-60994-4

McKay, J. P., Raizen, D. M., Gottschalk, A., Schafer, W. R., & Avery, L. (2004). *eat-2* and *eat-18* are required for nicotinic neurotransmission in the *Caenorhabditis elegans* pharynx. *Genetics*, *166*(1), 161–169. https://doi.org/10.1534/genetics.166.1.161

Mellem, J. E., Brockie, P. J., Madsen, D. M., & Maricq, A. V. (2008). Action potentials contribute to neuronal signaling in *C. elegans*. *Nature Neuroscience*, *11*(8), 865–867. https://doi.org/10.1038/nn.2131

Mobille, Z., Sikandar, U. B., Sponberg, S., & Choi, H. (2025). Temporal resolution of spike coding in feedforward networks with signal convergence and divergence. *PLoS Comput Biol*, *21*(4), e1012971. https://doi.org/10.1371/journal.pcbi.1012971

Mörck, C., & Pilon, M. (2006). *C. elegans* feeding defective mutants have shorter body lengths and increased autophagy. *BMC Dev Biol*, *6*, 39. https://doi.org/10.1186/1471-213X-6-39

Muscinelli, S. P., Wagner, M. J., & Litwin-Kumar, A. (2023). Optimal routing to cerebellum-like structures. *Nat Neurosci*, *26*(9), 1630–1641. https://doi.org/10.1038/s41593-023-01403-7

Nande, A., Dubinkina, V., Ravasio, R., Zhang, G. H., & Berman, G. J. (2022). Bottlenecks, modularity, and the neural control of behavior. *Front Behav Neurosci*, *16*, 835753. https://doi.org/10.3389/fnbeh.2022.835753

Naudin, L., Laredo, J. L. J., Liu, Q., & Corson, N. (2022). Systematic generation of biophysically detailed models with generalization capability for non-spiking neurons. *PLoS ONE*, *17*(5), e0268380. https://doi.org/10.1371/journal.pone.0268380

Nekimken, A. L., Fehlauer, H., Kim, A. A., Manosalvas-Kjono, S. N., Ladpli, P., Memon, F., Gopisetty, D., Sanchez, V., Goodman, M. B., Pruitt, B. L., & Krieg, M. (2017). Pneumatic stimulation of *C. elegans* mechanoreceptor neurons in a microfluidic trap. *Lab Chip*, *17*(6), 1116–1127. https://doi.org/10.1039/C6LC01165A

Nguyen, J. P., Linder, A. N., Plummer, G. S., Shaevitz, J. W., & Leifer, A. M. (2017). Automatically tracking neurons in a moving and deforming brain. *PLoS Comput Biol*, *13*(5), e1005517. https://doi.org/10.1371/journal.pcbi.1005517

Nguyen, J. P., Shipley, F. B., Linder, A. N., Plummer, G. S., Liu, M., Setru, S. U., Shaevitz, J. W., & Leifer, A. M. (2016). Whole-brain calcium imaging with cellular resolution in freely behaving *Caenorhabditis elegans*. *PNAS*, *113*(8), E1074–E1081.

O'Hagan, R., Chalfie, M., & Goodman, M. B. (2005). The MEC-4 DEG/ENaC channel of *Caenorhabditis elegans* touch receptor neurons transduces mechanical signals. *Nat. Neurosci.*, *8*(1), 43–50. https://doi.org/10.1038/nn1362

Okkema, P. G., Harrison, S. W., Plunger, V., Aryana, A., & Fire, A. (1993). Sequence requirements for *myosin* gene expression and regulation in *Caenorhabditis elegans*. *Genetics*, *135*(2), 385–404. https://doi.org/10.1093/genetics/135.2.385

Okkema, P., & Fire, A. (1994). The *Caenorhabditis elegans* NK-2 class homeoprotein CEH-22 is involved in combinatorial activation of gene expression in pharyngeal muscle. *Development*, *120*(8), 2175–2186. https://doi.org/10.1242/dev.120.8.2175

Pirri, J. K., & Alkema, M. J. (2012). The neuroethology of c. elegans escape. *Curr Opin Neurobiol*, *22*(2), 187–193. https://doi.org/10.1016/j.conb.2011.12.007

Pocock, R., & Hobert, O. (2010). Hypoxia activates a latent circuit for processing gustatory information in *C. elegans*. *Nat Neurosci*, *13*(5), 610–614. https://doi.org/10.1038/nn.2537

Pritz, C., Itskovits, E., Bokman, E., Ruach, R., Gritsenko, V., Nelken, T., Menasherof, M., Azulay, A., & Zaslaver, A. (2023). Principles for coding associative memories in a compact neural network. *eLife*, *12*, e74434. https://doi.org/10.7554/eLife.74434

Raizen, D. M., & Avery, L. (1994). Electrical activity and behavior in the pharynx of *Caenorhabditis elegans*. *Neuron*, *12*(3), 483–495. https://doi.org/10.1016/0896-6273(94)90207-0

Raizen, D. M., Lee, R. Y., & Avery, L. (1995). Interacting genes required for pharyngeal excitation by motor neuron MC in *Caenorhabditis elegans*. *Genetics*, *141*(4), 1365–1382. https://doi.org/10.1093/genetics/141.4.1365

Redemann, S., Schloissnig, S., Ernst, S., Pozniakowsky, A., Ayloo, S., Hyman, A. A., & Bringmann, H. (2011). Codon adaptation-based control of protein expression in c. elegans. *Nat Methods*, *8*(3), 250–252. https://doi.org/10.1038/nmeth.1565

Rodríguez-Palero, M. J., López-Díaz, A., Marsac, R., Gomes, J.-E., Olmedo, M., & Artal-Sanz, M. (2018). An automated method for the analysis of food intake behaviour in *Caenorhabditis elegans*. *Sci Rep*, *8*(1), 3633. https://doi.org/10.1038/s41598-018-21964-z

Saberski, E., Bock, A. K., Goodridge, R., Agarwal, V., Lorimer, T., Rifkin, S. A., & Sugihara, G. (2021). Networks of causal linkage between eigenmodes characterize behavioral dynamics of caenorhabditis elegans. *PLoS Comput Biol*, *17*(9), e1009329. https://doi.org/10.1371/journal.pcbi.1009329

Sawin, E. R., Ranganathan, R., & Horvitz, H. R. (2000). *C. elegans* locomotory rate is modulated by the environment through a dopaminergic pathway and by experience through a serotonergic pathway. *Neuron*, *26*(3), 619–631. https://doi.org/10.1016/s0896-6273(00)81199-x

Schindelin, J., Arganda-Carreras, I., Frise, E., Kaynig, V., Longair, M., Pietzsch, T., Preibisch, S., Rueden, C., Saalfeld, S., Schmid, B., Tinevez, J.-Y., White, D. J., Hartenstein, V., Eliceiri, K., Tomancak, P., & Cardona, A. (2012). Fiji: An open-source platform for biological-image analysis. *Nat Methods*, *9*(7), 676–682. https://doi.org/10.1038/nmeth.2019

Scholkmann, F., Boss, J., & Wolf, M. (2012). An efficient algorithm for automatic peak detection in noisy periodic and quasi-periodic signals. *Algorithms*, *5*(4), 588–603. https://doi.org/10.3390/a5040588

Scholz, M., Dinner, A. R., Levine, E., & Biron, D. (2017). Stochastic feeding dynamics arise from the need for information and energy. *PNAS*, *114*(35), 9261–9266. https://doi.org/10.1073/pnas.1703958114

Scholz, M., Lynch, D. J., Lee, K. S., Levine, E., & Biron, D. (2016). A scalable method for automatically measuring pharyngeal pumping in *C. elegans*. *Journal of Neuroscience Methods*, *274*, 172–178. https://doi.org/10.1016/j.jneumeth.2016.07.016

Seymour, M. K., Wright, K. A., & Doncaster, C. C. (1983). The action of the anterior feeding apparatus of *Caenorhabditis elegans* (<i>nematoda</i: <i>rhabditida</i). *Journal of Zoology*, *201*(4), 527–539. https://doi.org/10.1111/j.1469-7998.1983.tb05074.x

Shannon, P., Markiel, A., Ozier, O., Baliga, N. S., Wang, J. T., Ramage, D., Amin, N., Schwikowski, B., & Ideker, T. (2003). Cytoscape: A software environment for integrated models of biomolecular interaction networks. *Genome Res*, *13*(11), 2498–2504. https://doi.org/10.1101/gr.1239303

Shaw, M., Elmi, M., Pawar, V., & Srinivasan, M. A. (2016). Investigation of mechanosensation in *C. elegans* using light field calcium imaging. *Biomed. Opt. Express, BOE*, *7*(7), 2877–2887. https://doi.org/10.1364/BOE.7.002877

Shtonda, B., & Avery, L. (2005). CCA-1, EGL-19 and EXP-2 currents shape action potentials in the *Caenorhabditis elegans* pharynx. *J Exp Biol*, *208*(11), 2177–2190. https://doi.org/10.1242/jeb.01615

Song, B.-M., & Avery, L. (2012). Serotonin activates overall feeding by activating two separate neural pathways in *Caenorhabditis elegans*. *J Neurosci*, *32*(6), 1920–1931. https://doi.org/10.1523/jneurosci.2064-11.2012

Song, B.-M., Faumont, S., Lockery, S., & Avery, L. (2013). Recognition of familiar food activates feeding via an endocrine serotonin signal in *Caenorhabditis elegans* (P. Mason, Ed.). *eLife*, *2*, e00329. https://doi.org/10.7554/eLife.00329

Spirou, G. A., Rager, J., & Manis, P. B. (2005). Convergence of auditory-nerve fiber projections onto globular bushy cells. *Neuroscience*, *136*(3), 843–863. https://doi.org/10.1016/j.neuroscience.2005.08.068

Sridhar, V. H., Li, L., Gorbonos, D., Nagy, M., Schell, B. R., Sorochkin, T., Gov, N. S., & Couzin, I. D. (2021). The geometry of decision-making in individuals and collectives. *Proceedings of the National Academy of Sciences*, *118*(50), e2102157118. https://doi.org/10.1073/pnas.2102157118

Starich, T. A., Xu, J., Skerrett, I. M., Nicholson, B. J., & Shaw, J. E. (2009). Interactions between innexins UNC-7 and UNC-9 mediate electrical synapse specificity in the *Caenorhabditis elegans* locomotory nervous system. *Neural Development*, *4*(1), 16. https://doi.org/10.1186/1749-8104-4-16

Stephens, G. J., Johnson-Kerner, B., Bialek, W., & Ryu, W. S. (2008). Dimensionality and dynamics in the behavior of *C. elegans*. *PLoS Comput Biol*, *4*(4), e1000028. https://doi.org/10.1371/journal.pcbi.1000028

Sugi, T., Igarashi, R., & Nishimura, M. (2018). Noninvasive mechanochemical imaging in unconstrained <i>caenorhabditis elegans<\i>. *Materials (Basel)*, *11*(6). https://doi.org/10.3390/ma11061034

Sugi, T., Okumura, E., Kiso, K., & Igarashi, R. (2016). Nanoscale mechanical stimulation method for quantifying *C. elegans* mechanosensory behavior and memory. *Analytical Sciences*, *32*(11), 1159–1164. https://doi.org/10.2116/analsci.32.1159

Suzuki, H., Kerr, R., Bianchi, L., Frøkjær-Jensen, C., Slone, D., Xue, J., Gerstbrein, B., Driscoll, M., & Schafer, W. R. (2003). *In vivo* imaging of *C. elegans* mechanosensory neurons demonstrates a specific role for the MEC-4 channel in the process of gentle touch sensation. *Neuron*, *39*(6), 1005–1017. https://doi.org/10.1016/j.neuron.2003.08.015

Swierczek, N. A., Giles, A. C., Rankin, C. H., & Kerr, R. A. (2011). High-throughput behavioral analysis in *C. elegans*. *Nat. Methods*, *8*(7), 592–598. https://doi.org/10.1038/nmeth.1625

Takahashi, M., & Takagi, S. (2017). Optical silencing of body wall muscles induces pumping inhibition in *Caenorhabditis elegans*. *PLoS Genetics*, *13*(12), e1007134. https://doi.org/10.1371/journal.pgen.1007134

Thornberry, N. A., Bull, H. G., Calaycay, J. R., Chapman, K. T., Howard, A. D., Kostura, M. J., Miller, D. K., Molineaux, S. M., Weidner, J. R., & Aunins, J. (1992). A novel heterodimeric cysteine protease is required for interleukin-1 beta processing in monocytes. *Nature*, *356*(6372), 768–774. https://doi.org/10.1038/356768a0

Tinevez, J.-Y., Perry, N., Schindelin, J., Hoopes, G. M., Reynolds, G. D., Laplantine, E., Bednarek, S. Y., Shorte, S. L., & Eliceiri, K. W. (2017). TrackMate: An open and extensible platform for single-particle tracking. *Methods*, *115*, 80–90. https://doi.org/10.1016/j.ymeth.2016.09.016

Trojanowski, N. F., Raizen, D. M., & Fang-Yen, C. (2016). Pharyngeal pumping in *Caenorhabditis elegans* depends on tonic and phasic signaling from the nervous system. *Sci Rep*, *6*(1), 1–10. https://doi.org/10.1038/srep22940

Turek, M., Lewandrowski, I., & Bringmann, H. (2013). An AP2 transcription factor is required for a sleep-active neuron to induce sleep-like quiescence in *C. elegans*. *Curr Biol*, *23*(22), 2215–2223. https://doi.org/10.1016/j.cub.2013.09.028

Venkatachalam, V., Ji, N., Wang, X., Clark, C., Mitchell, J. K., Klein, M., Tabone, C. J., Florman, J., Ji, H., Greenwood, J., Chisholm, A. D., Srinivasan, J., Alkema, M., Zhen, M., & Samuel, A. D. T. (2016). Pan-neuronal imaging in roaming *Caenorhabditis elegans*. *Proceedings of the National Academy of Sciences*, *113*(8), E1082–E1088. https://doi.org/10.1073/pnas.1507109113

Voleti, V., Patel, K. B., Li, W., Campos, C. P., Bharadwaj, S., Yu, H., Ford, C., Casper, M. J., Yan, R. W., Liang, W., Wen, C., Kimura, K. D., Targoff, K. L., & Hillman, E. M. C. (2019). Real-time volumetric microscopy of *in vivo* dynamics and large-scale samples with SCAPE 2.0. *Nat Methods*, *16*(10), 1054–1062. https://doi.org/10.1038/s41592-019-0579-4

Wakabayashi, T., Kitagawa, I., & Shingai, R. (2004). Neurons regulating the duration of forward locomotion in *Caenorhabditis elegans*. *Neuroscience Research*, *50*(1), 103–111. https://doi.org/10.1016/j.neures.2004.06.005

Wang, H., Liu, J., Gharib, S., Chai, C. M., Schwarz, E. M., Pokala, N., & Sternberg, P. W. (2017). cGAL, a temperature-robust GAL4–UAS system for *Caenorhabditis elegans*. *Nat Methods*, *14*(2), 145–148. https://doi.org/10.1038/nmeth.4109

Ward, A., Liu, J., Feng, Z., & Xu, X. Z. S. (2008). Light-sensitive neurons and channels mediate phototaxis in *C. elegans*. *Nat Neurosci*, *11*(8), 916–922. https://doi.org/10.1038/nn.2155

White, J. G., Southgate, E., Thomson, J. N., & Brenner, S. (1976). The structure of the ventral nerve cord of *Caenorhabditis elegans*. *Philos Trans R Soc Lond B Biol Sci*, *275*(938), 327–348. https://doi.org/10.1098/rstb.1976.0086

White, J. G., Southgate, E., Thomson, J. N., & Brenner, S. (1986). The structure of the nervous system of the nematode *Caenorhabditis elegans*. *Philosophical Transactions of the Royal Society of London. B, Biological Sciences*, *314*(1165), 1–340. https://doi.org/10.1098/rstb.1986.0056

Wicks, S. R., & Rankin, C. H. (1995). Integration of mechanosensory stimuli in *Caenorhabditis elegans*. *J. Neurosci.*, *15*(3), 2434–2444. https://doi.org/10.1523/jneurosci.15-03-02434.1995

Wicks, S. R., Roehrig, C. J., & Rankin, C. H. (1996). A dynamic network simulation of the nematode tap withdrawal circuit: Predictions concerning synaptic function using behavioral criteria. *J. Neurosci.*, *16*(12), 4017–4031. https://doi.org/10.1523/jneurosci.16-12-04017.1996

Yemini, E., Lin, A., Nejatbakhsh, A., Varol, E., Sun, R., Mena, G. E., Samuel, A. D. T., Paninski, L., Venkatachalam, V., & Hobert, O. (2021). NeuroPAL: A multicolor atlas for whole-brain neuronal identification in *C. elegans*. *Cell*, *184*(1), 272–288.e11. https://doi.org/10.1016/j.cell.2020.12.012

You, Y.-j., Kim, J., Cobb, M., & Avery, L. (2006). Starvation activates MAP kinase through the muscarinic acetylcholine pathway in *Caenorhabditis elegans* pharynx. *Cell Metabolism*, *3*(4), 237–245. https://doi.org/10.1016/j.cmet.2006.02.012

You, Y.-j., Kim, J., Raizen, D. M., & Avery, L. (2008). Insulin, cGMP, and TGF-β signals regulate food intake and quiescence in *C. elegans*: A model for satiety. *Cell Metabolism*, *7*(3), 249–257. https://doi.org/10.1016/j.cmet.2008.01.005

Yu, F. H., Yarov-Yarovoy, V., Gutman, G. A., & Catterall, W. A. (2005). Overview of molecular relationships in the voltage-gated ion channel superfamily. *Pharmacol Rev*, *57*(4), 387–395. https://doi.org/10.1124/pr.57.4.13

Zhang, Y., Rózsa, M., Liang, Y., Bushey, D., Wei, Z., Zheng, J., Reep, D., Broussard, G. J., Tsang, A., Tsegaye, G., Narayan, S., Obara, C. J., Lim, J.-X., Patel, R., Zhang, R., Ahrens, M. B., Turner, G. C., Wang, S. S.-H., Korff, W. L., ... Looger, L. L. (2023). Fast and sensitive GCaMP calcium indicators for imaging neural populations. *Nature*, *615*(7954), 884–891. https://doi.org/10.1038/s41586-023-05828-9

Zhao, B., Khare, P., Feldman, L., & Dent, J. A. (2003). Reversal frequency in *Caenorhabditis elegans* represents an integrated response to the state of the animal and its environment. *J. Neurosci.*, *23*(12), 5319–5328. https://doi.org/10.1523/jneurosci.23-12-05319.2003

Zhaoping, L. (2006). Theoretical understanding of the early visual processes by data compression and data selection. *Network*, *17*(4), 301–334. https://doi.org/10.1080/09548980600931995

Zheng, Y., Brockie, P. J., Mellem, J. E., Madsen, D. M., & Maricq, A. V. (1999). Neuronal control of locomotion in *C. elegans* is modified by a dominant mutation in the GLR-1 ionotropic glutamate receptor. *Neuron*, *24*(2), 347–361. https://doi.org/10.1016/S0896-6273(00)80849-1

Zou, W., Fu, J., Zhang, H., Du, K., Huang, W., Yu, J., Li, S., Fan, Y., Baylis, H. A., Gao, S., Xiao, R., Ji, W., Kang, L., & Xu, T. (2018). Decoding the intensity of sensory input by two glutamate receptors in one *C. elegans* interneuron. *Nature Communications*, *9*(1), 4311. https://doi.org/10.1038/s41467-018-06819-5

Statement on own contribution

This thesis was carried out at the Max Planck Institute for Neurobiology of Behavior - caesar (MPINB) in the Neuronal Information Flow group under the supervision of Dr. Monika Scholz.

The work related to the first aim (**Section** 1.4 "Measuring feeding in freely moving animals") has been published in a peer-reviewed journal: Bonnard, E., Liu, J., Zjacic, N., Alvarez, L., & Scholz, M. (2022). Automatically tracking feeding behavior in populations of foraging *C. elegans*. *eLife*, *11*, e77252. https://doi.org/10.7554/eLife.77252 I am the co-first author of this publication, with equal contribution shared with Dr. Jun Liu. My personal contributions included: experimental design, setup, and protocol development. Data acquisition. Code development in a user-tester capacity (error identification and debugging). Manuscript writing (contributing to sections, review, and editing).

The work related to the second aim (**Section** 1.4 "Establishing the touch-feeding paradigm and quantifying the psychometric curves") and to the third aim (**Section** 1.4 "Measuring information flow through the bottleneck") for neuronal calcium imaging in behaving animal is included in a manuscript in preparation: Bonnard, E., Liu, J., Alvarez, L., Iyer, A., & Scholz, A. (manuscript in prep.). A vagus-like bottleneck neuron between enteric and somatic nervous systems integrates aversive stimuli, feeding behavior and motor signals. My personal contributions for the behavioral assays included: Experimental design, setup, and protocol development. Data acquisition. Code development and analysis. Manuscript writing (sections). My personal contributions for neuronal calcium imaging part included: Experimental design, setup, and protocol development. Data acquisition. Behavioral data analysis. Manuscript writing.

Part of the work related to the third aim (**Section** 1.4 "Measuring information flow through the bottleneck") for neuronal calcium imaging in immobilized animal has been published in a peer-reviewed journal: Liu, J., Bonnard, E., & Scholz, M. (2024). Adapting and optimizing GCaMP8f for use in *Caenorhabditis elegans*. *Genetics*, iyae125. https://doi.org/10.1093/genetics/iyae125 I am the co-first author of this publication, with equal contribution shared with Dr. Jun Liu. My personal contributions focused on neuronal calcium imaging: experimental design, setup, and protocol development. Data acquisition. Code development and Analysis. Manuscript writing.

Transgenic lines were either provided by *Caenorhabditis* Genetics Center, kindly shared by other laboratories (Drs. Miriam Goodman and Paul Sternberg) or created in our laboratory by Dr. Jun Liu. I contributed to strain crossing and verification by confocal microscopy. Some plasmids were kindly shared by other laboratories (Drs. Marc Pilon and Manuel Zimmer), or generated in our laboratory by Dr. Jun Liu, or by Dr. Wolfgang Bönigk from the genetic facility at MPINB. Microscopes for calcium imaging were build and/or maintained by Dr. Luis Alvarez (Scholz Lab). I took over some maintenance and improvement of the setups after training.

I used ChatGPT to improve the readability and language of the manuscript. After using this tool, I reviewed and edited the relevant passages and take full responsibility for the content of the published dissertation. I hereby confirm that my thesis complies with the Statement by the Executive Committee of the Deutsche Forschungsgemeinschaft (DFG, German Research Foundation) on the Influence of Generative Models of Text and Image Creation on Science and the Humanities and on the DFG's Funding Activities.

Acknowledgments

I am deeply grateful to everyone who has supported me throughout this journey. Each of you has contributed to this work in your own way.

First, I would like to thank Prof. Dr. Ilona Grunwald Kadow, Dr. Aneta Koseska, Prof. Dr. Tobias Rose, and Dr. Monika Scholz for agreeing to be on my thesis examination committee. To them, and to Prof. Dr. Miriam Goodman, I am thankful for their valuable guidance, advice, and feedback over the years as members of my Thesis Advisory Committee.

I am grateful to my supervisor Dr. Monika Scholz for entrusting me with this project and for her dedicated supervision. I thank her as well for her direct contributions to this thesis, by sharing her expertise, providing insightful ideas, building optical setups and analysis pipelines and by performing experiments.

I thank my teammates, Dr. Jun Liu and Dr. Luis Alvarez, who worked closely with me, taught me and played a crucial role in all steps of the project. I am grateful to Euphrasie Ramahefarivo for being a boundless source of energy, refreshing questions and ideas. I also thank Serdi, Takka, Miry, all former team members, and Dr. James Lightfoot's lab for stimulating discussions, feedback on manuscripts and presentations, and for all the good times shared. Special thanks to Fumie Hiramatsu for her diligent care and friendship.

I am grateful to the Max Planck Institute for Neurobiology of Behavior and the International Max Planck Research School (IMPRS) for Brain and Behavior for providing an excellent scientific environment and the resources essential for this work. I want to thank particularly Dr. Wolfgang Bönigk from the Genetic Facility for essential plasmids and advice; Dr. René Pascal from the Microscopy Facility for guidance with confocal imaging; Michael Straußfeld and Rolf Honnef from the Mechanical Workshop for helping me building and repairing experimental devices, often on-the-fly; Omar Valerio Minero and the Scientific Computing team for their support in exploring new analysis avenues and for cluster management; Corinna Bernsdorff from IT for her ever-ready assistance; and Ruth Scherger, for whom there were no inaccessible papers!; and the IMPRS coordinators, Ezgi Bulca and Eva Gentes, for their dedication to the students. I would like to extend my gratitude to the PhD and postdoc community, and to all those who organized retreats, seminars, and social events, who created a collaborative and supportive atmosphere.

Finally, I thank my family for being my anchor. Through all challenges, their unwavering support and love have been my constant guide and inspiration. Here we are.

Thank you all !